POLITECNICO DI TORINO

Master's Degree in Aerospace engineering

Master's Degree Thesis

Quantifying paravalvular leakage after transcatheter aortic valve replacement using particle image velocimetry

Supervisors

Prof. Stefania SCARSOGLIO

Prof. Vrishank RAGHAV

Candidate

Michele MASTROGIACOMO

JULY 2024

Summary

Cardiovascular diseases (CVD) are the leading cause of death in the United States, claiming a life every 33 seconds. In 2021, CVD accounted for approximately 695,000 deaths, underscoring the urgent need for enhanced preventive and therapeutic strategies. Globally, the challenge of CVD continues to grow, with 19.05 million deaths in 2020, highlighting the escalating burden of cardiovascular diseases. Heart diseases, particularly valvular diseases, play a significant role in global health issues, especially among the elderly population. Valvular conditions, such as aortic stenosis, are prevalent and complex, disrupting critical cardiovascular functions. Aortic stenosis, primarily caused by age-related calcification of the aortic valve, restricts blood flow from the left ventricle to the aorta. This condition affects 0.4% of the general population and 1.7% of those over 65. The primary treatment strategies for aortic stenosis include Surgical Aortic Valve Replacement (SAVR) and Transcatheter Aortic Valve Replacement (TAVR). TAVR, a less invasive procedure developed as an alternative to open-heart surgery, involves inserting a new valve into the heart through a small cut, typically in the leg or chest. Despite advancements in TAVR technology, mild to moderate Paravalvular Leak (PVL) still occurs in up to 19.7% of procedures. PVL is a complication where blood leaks around the edges of the implanted valve due to imperfect sealing, leading to inefficient blood flow and increased cardiac workload. Given the prevalence and impact of PVL, there is a critical need to study and mitigate this issue to improve patient outcomes. This thesis investigates PVL in an experimental way using a custom-built left heart simulator and Particle Image Velocimetry (PIV). The experimental setup replicates the human left heart, featuring a Pulsatile Pump ViVitro, an em-tec flow meter, pressure taps, and a transparent acrylic test chamber housing a heart valve. The working fluid, a water-glycerin mix, mimics the viscosity and density of blood and is maintained at a constant temperature of 37°C to replicate human physiological conditions. The structure of this thesis is organized to provide a comprehensive exploration of Paravalvular Leak (PVL) and its implications in cardiovascular treatments. The initial chapter lays the groundwork with an introduction to the cardiovascular system, detailing heart diseases, particularly valvular diseases such as aortic stenosis. This chapter also discusses the significance of Transcatheter Aortic

Valve Replacement (TAVR) as a less invasive alternative to traditional surgery and provides an explanation of PVL, including its causes, prevalence, and impact on patient outcomes. Following this, the thesis delves into the experimental setup, describing the design and components of the custom-built left heart simulator used for this study. The methodology employed in the experiments is outlined next. This section covers the procedures for data acquisition, detailing the setup of the PIV system, alignment of the laser and camera, and techniques used to ensure accurate measurements. It also explains the analysis methods for processing collected data. The chapter emphasizes the calibration process for the Particle Image Velocimetry (PIV) system, with the use of a plenoptic camera. The experimental results will be presented through 2D and 3D visualizations. The 2D results, derived from planar PIV, and the 3D results, obtained from plenoptic PIV, will illustrate the velocity field. Additionally, results on turbulent kinetic energy (TKE), viscous shear stress (VSS), and Reynolds shear stress(RSS) will be included. In the final chapter, these results will be thoroughly discussed, interpreting their implications for current knowledge about PVL and cardiovascular dynamics.

Acknowledgements

Questo lavoro segna la fine di un percorso di fondamentale importanza nella mia vita, durante il quale ho avuto modo di imparare e crescere sia come studente sia come individuo. In primis, vorrei ringraziare i miei genitori, Giusy e Giovanni, e mia sorella Martina, che mi hanno sempre supportato in questa avventura. Senza di loro, questo traguardo non sarebbe stato possibile.

Un sincero ringraziamento va anche ai miei amici, la cui presenza costante e il supporto continuo hanno reso questo viaggio più sereno e piacevole. Grazie per avermi alleviato le giornate e per i tanti momenti di condivisione che hanno arricchito questa esperienza.

Infine, desidero ringraziare il Dr.Raghav e tutti i membri dell'Applied Fluids Research Group per avermi dato l'opportunità di svolgere il mio lavoro di tesi presso l'Auburn University e per essersi dimostrati sempre disponibili durante il mio lavoro. Un ringraziamento speciale va anche alla professoressa Scarsoglio, relatrice del mio lavoro, per avermi seguito e guidato con dedizione durante la stesura della mia tesi.

A tutti voi, la mia più profonda gratitudine.

Table of Contents

List of Tables

List of Figures

Chapter 1

Introduction

1.1 Summary on cardiovascular system

The primary function of the cardiovascular system is to supply oxygen and nutrients to the tissues and cells while removing metabolic wastes like CO2. This system comprises the heart, which acts as a pumping mechanism, a distribution network consisting of veins and arteries, and a transport fluid, namely blood. The heart consists of two atria and two ventricles, along with four cardiac valves.

The cardiovascular system is composed of:

- **Systemic circulation**

  The systemic circulation is the largest circulation system in the body, aimed at transporting oxygenated blood to all major muscles and organs. Approximately 86% of the blood volume in the cardiovascular system is contained within this circulation. To illustrate its significance, the aortic system pressure typically ranges between 80-120 mmHg.

- **Pulmonary circulation**

  The purpose of the pulmonary circuit is to transport blood containing waste products to the lungs, where toxic substances like CO2 can be expelled, and oxygen can be added to the blood through the respiratory system. This circuit constitutes approximately 9% of the total blood volume in the cardiovascular system. Typically, the pulmonary pressure ranges between 10-30 mmHg.

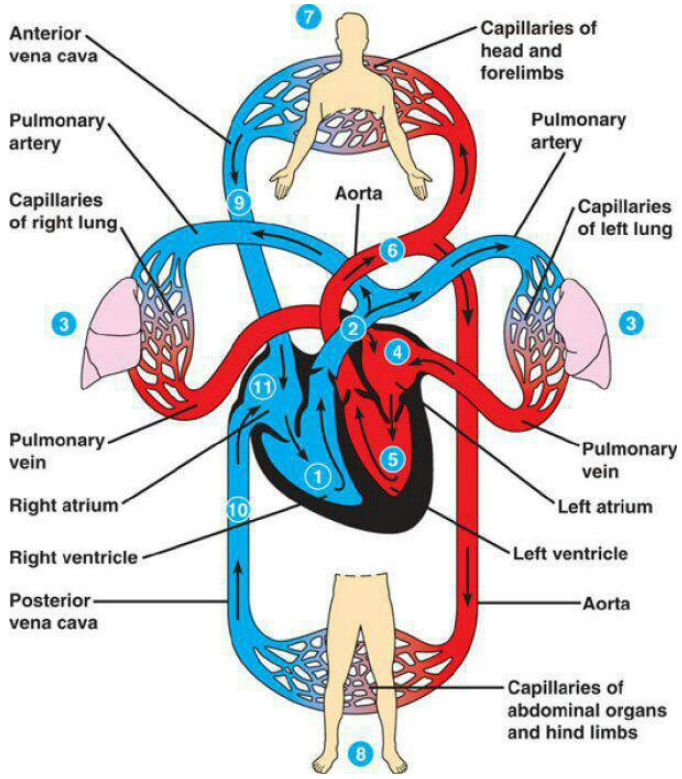

Figure 1.1: Aortic and pulmonary systems [1]

1.1.1 Arterial and venous system

Blood vessels, including arteries and veins, serve as muscular tubes through which blood circulates. Arteries carry blood away from the heart to various tissues and organs throughout the body, while veins return blood back to the heart. Due to their distinct functions, arteries and veins possess different characteristics, including variations in pressure, pulsatility, and resistance.

- **Arterial system**

  The arterial system functions by transporting oxygenated blood from the heart to various tissues and organs throughout the body. This process initiates in the left ventricle of the heart, where oxygenated blood is ejected into the aorta, the body's largest artery. From the aorta, oxygen-rich blood is conveyed into smaller arteries, which branch out and distribute blood to specific regions of the body.

As blood travels through the arteries, it goes through even smaller vessels known as arterioles. Arterioles regulate blood flow to specific tissues and organs by modulating their diameter through vasoconstriction (narrowing) or vasodilation (widening). This mechanism aids in controlling blood pressure and allocating blood flow as per the body's requirements.

Arterioles further connect to networks of microscopic blood vessels called capillaries. In capillaries, exchange of oxygen, nutrients, and metabolic waste products occurs between the blood and surrounding tissues. Oxygen and nutrients diffuse out of the capillaries into the tissues, while carbon dioxide and other waste products move from the tissues into the bloodstream. At this stage, pressure is reduced to facilitate the exchange of nutrients, decreasing from approximately 80-120 mmHg to 20-25 mmHg for the systemic circulation. This decrease in pressure allows for efficient nutrient exchange within the capillaries, ensuring that tissues receive the necessary oxygen and nutrients while waste products are removed.

Throughout this process, pressure, pulsatility, and resistance undergo changes. Pressure gradually decreases as blood progresses from the heart through arteries, arterioles, and capillaries. Pulsatility diminishes in capillaries due to their high compliance, enabling continuous blood flow and exchange. Arterioles play a critical role in the regulation of blood flow and systemic vascular resistance, influencing the general distribution of blood pressure. In addition, the dimensions of these blood vessels decrease from the aorta to the capillaries, while the number of vessels increases. This structural adaptation enables the efficient distribution of blood throughout the body, ensuring that each tissue and organ receives an adequate blood supply for its metabolic needs.

- **Venous system**

After delivering oxygen and nutrients to the tissues, blood undergoes a transformation, becoming deoxygenated and laden with metabolic waste products. This altered composition prompts its collection by venules, which are small veins converging to form larger veins. Throughout this phase, the venous system adapts dynamically, exhibiting characteristics such as compliance and resistance. Unlike the arterial system, the venous system is not pulsatile and operates at a very low pressure.

Veins play a fundamental role in this process, transporting deoxygenated blood back to the heart, specifically to the right atrium. From there, the blood proceeds to enter the pulmonary circulation, where it undergoes oxygenation once again, completing the circulatory cycle.

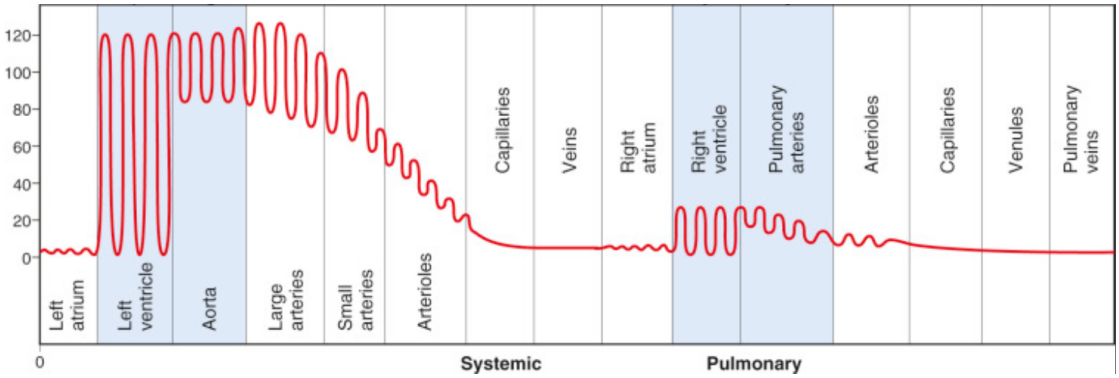

Figure 1.2: Pressure and pulsatility in blood vessels [1]

1.1.2 Blood

Blood, a complex and essential fluid, is primarily composed of plasma, red and white blood cells, and platelets. Plasma, which constitutes about 55% of its volume, is the medium for carrying cells that perform crucial functions. Red blood cells are vital for oxygen transport and greatly influence the viscosity of the blood. Typically, blood contains 4.5 to 5.5 million red blood cells per microliter, 4,000 to 11,000 white blood cells per microliter, and 150,000 to 400,000 platelets per microliter. The viscosity of blood at 37 ° C generally ranges from 3 to 4 centipoise [2], shaped by hematocrit and shear rate. The average density of blood is about 1060 kg/m^3, and adults typically have around 5 liters of blood.

1.2 Heart

The human heart, central to the circulatory system, is composed of four main chambers: the upper atria and the lower ventricles. The atria collect blood from various parts of the body and lungs, then transfer it to the ventricles. The ventricles are responsible for pumping the blood to the lungs and the rest of the body. The right ventricle sends deoxygenated blood to the lungs, while the left ventricle pumps oxygenated blood throughout the body. The heart contains about 8% of the total blood volume in the human body. The heart beats in a rhythmic pattern, generally ranging from 60 to 100 beats per minute in adults, with variations dependent on individual health, activity, and age levels. This rhythmic activity is vital for effective blood circulation and optimal health maintenance.

1.2.1 Heart valves

The heart includes four valves that regulate blood flow, ensuring efficient circulation through its chambers:

1. **Tricuspid Valve:** Situated between the right atrium and right ventricle, this valve has three leaflets and opens when the pressure in the atrium is greater than in the ventricle.

2. **Pulmonary Valve:** Located between the right ventricle and the pulmonary artery, it consists of three cusps and opens when the pressure in the ventricle exceeds that in the artery.

3. **Mitral Valve (Bicuspid Valve):** Positioned between the left atrium and left ventricle, it includes two leaflets and opens when the atrial pressure surpasses the ventricular pressure.

4. **Aortic Valve:** Found at the exit of the left ventricle leading to the aorta, this valve typically has three cusps and opens when ventricular pressure is higher than aortic pressure.

These valves are essential for maintaining the unidirectional flow of blood and preventing backflow, critical for the heart's optimal function.

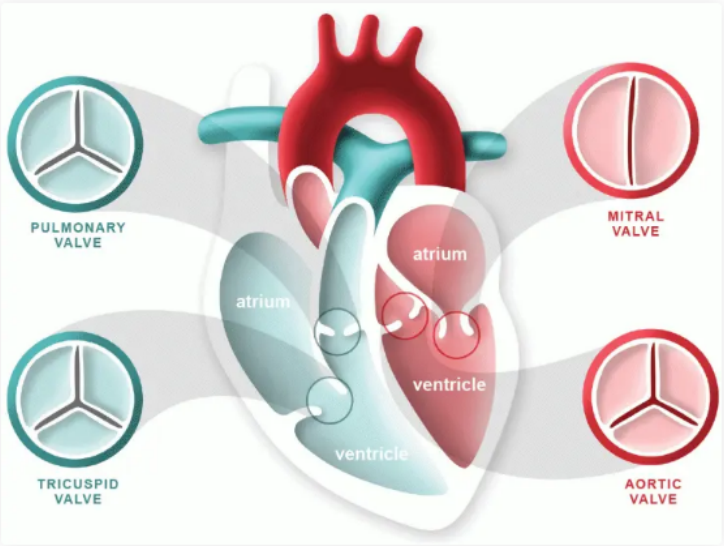

Figure 1.3: Heart valves scheme [3]

1.2.2 Cardiac cycle

The cardiac cycle consists of two main phases: systole and diastole. Systole involves contraction of the heart muscles and ejection of blood, beginning with the closure of the mitral valve and ending when the aortic valve closes. Diastole, on the other hand, starts with the closing of the aortic valve and is characterized by isovolumetric relaxation followed by the heart filling with blood, concluding with the mitral valve closing. To visualize these dynamics, a pressure-volume (PV) loop diagram can be particularly useful, as it graphically represents the changes in volume and pressure within the heart during these phases.

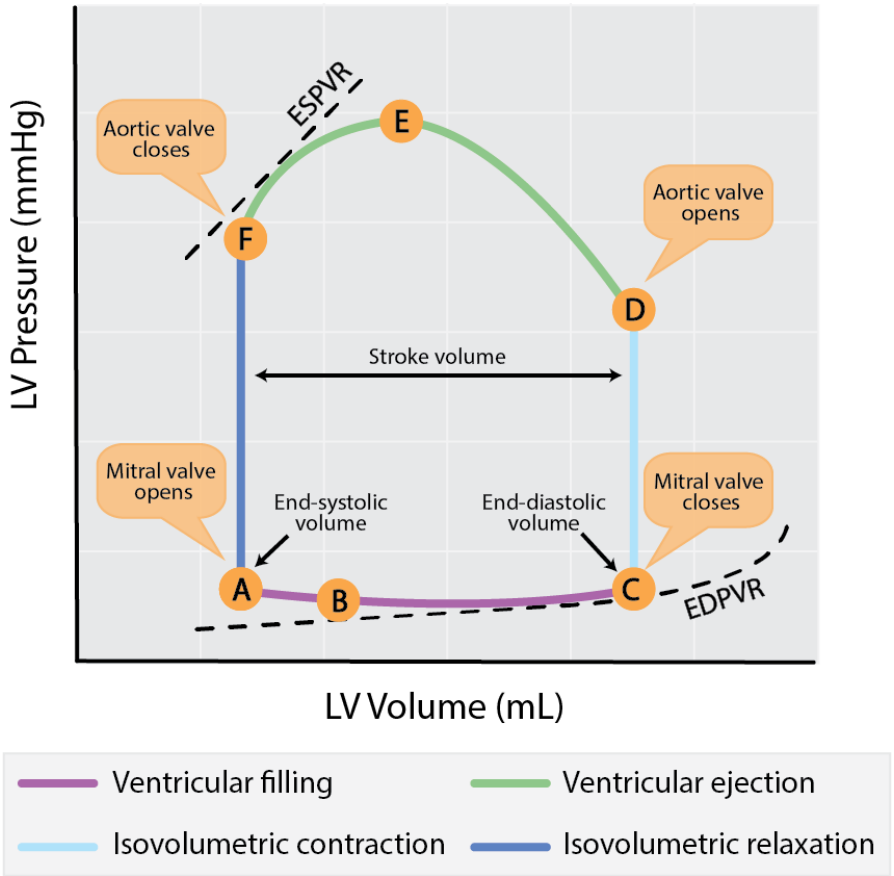

Figure 1.4: PV loop heart [4]

The analysis in this thesis relies heavily on understanding several key cardiovascular parameters defined in agrremen with [5]:

- **Stroke Volume (SV)**: This is the volume of blood pumped from the left ventricle of the heart with each beat, typically measured in milliliters (mL). It is calculated using the formula:

  $$SV = EDV - ESV$$

  where EDV is end-diastolic volume and ESV is end-systolic volume.

- **Cardiac Output (CO)**: The total volume of blood pumped by the ventricle per minute, measured in liters per minute (L/min). The formula for cardiac output is:

  $$CO = HR \times SV$$

- **Closing Volume**: The volume of fluid that passes through a valve from fully open to fully closed, typically measured in milliliters (mL).

- **Regurgitant Volume** Volume of fluid that flows through a heart valve substitute in the reverse direction during one cycle and is the sum of the closing volume and the leakage volume.

- **Regurgitant Fraction** Regurgitant volume expressed as a percentage of the forward flow volume.

- **Leakage Volume** Portion of the regurgitant volume which is associated with leakage during the closed phase of a valve in a single cycle and is the sum of the transvalvular leakage volume and paravalvular leakage volume.

- **Paravalvular Leakage Volume** Portion of the leakage volume that is associated with leakage around the closed heart valve substitute during a single cycle.

- **Transvalvular Leakage Volume** Component of the leakage volume that is associated with leakage through the closed valve during a single cycle.

- **Effective Regurgitant Orifice Area (EROA)** Effective Regurgitant Orifice Area (EROA) is a measurement used to assess the severity of aortic regurgitation by quantifying the size of the circular-shaped opening through which blood flows back into the ventricular side.

Defining these quantities is fundamental for working technically on biofluidynamics. Many of these quantities can be referred to using the Wigger's diagram:

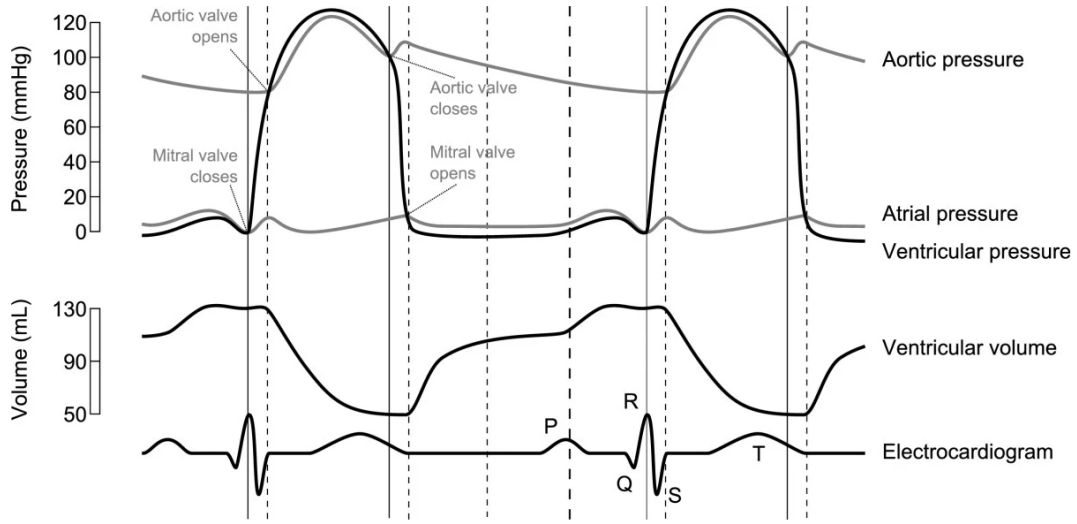

Figure 1.5: Wigger's Diagram [6]

1.3 Cardiovascular diseases (CVD)

Cardiovascular diseases (CVD) claim a life every 33 seconds in the United States, making them the leading cause of death across most demographic groups. In 2021, CVD accounted for approximately 695,000 deaths, representing one in every five deaths nationally [7]. The financial impact is significant, with annual costs associated with heart disease estimated at $239.9 billion between 2018 and 2019, covering healthcare services, medications, and lost productivity due to death. diseases Cardiovascular diseases (CVD) claim a life every 33 seconds in the United States, making them the leading cause of death across most demographic groups. In 2021, CVD accounted for approximately 695,000 deaths, representing one in every five deaths nationally [7]. The financial impact is significant, with annual costs associated with heart disease estimated at $239.9 billion between 2018 and 2019, covering healthcare services, medications, and lost productivity due to death. Globally, the challenge of CVD continues to grow. In 2020, CVD led to 19.05 million deaths, an 18.71% increase from 2010. Despite a 12.19% decrease in the age-standardized death rate during the same period, the crude prevalence of CVD increased by 29.01%, reaching 607.64 million cases worldwide. This data underscores the urgent need for enhanced preventive and therapeutic strategies to address the escalating burden of cardiovascular diseases. [8] Heart diseases remain a leading cause of health issues globally, with valvular diseases playing a significant role, particularly among the elderly population. Among various heart conditions, valvular diseases stand out due to their complexity and the critical function they disrupt in the cardiovascular system. Valvular conditions, such as

aortic stenosis, are prevalent in the aging population and represent a substantial portion of cardiovascular morbidity.

1.3.1 Aortic Stenosis

Aortic stenosis is a progressive disease that is most commonly caused by age-related calcification of the aortic valve in the elderly, though it can also arise from congenital conditions such as a bicuspid aortic valve. The disease is characterized by the narrowing of the aortic valve opening, which restricts blood flow from the left ventricle to the aorta, the main artery supplying blood to the rest of the body. The pathobiology of calcific aortic stenosis (AS) is complex, involving genetic factors, lipoprotein deposition and oxidation, chronic inflammation, osteoblastic transition of cardiac valve interstitial cells, and active leaflet calcification [9]. Aortic stenosis has a prevalence of 0.4% in the general population, increasing to 1.7% among those older than 65 years. As the population ages, the incidence of this condition is expected to rise, reflecting the increasing prevalence of calcific valve diseases in older adults [9].

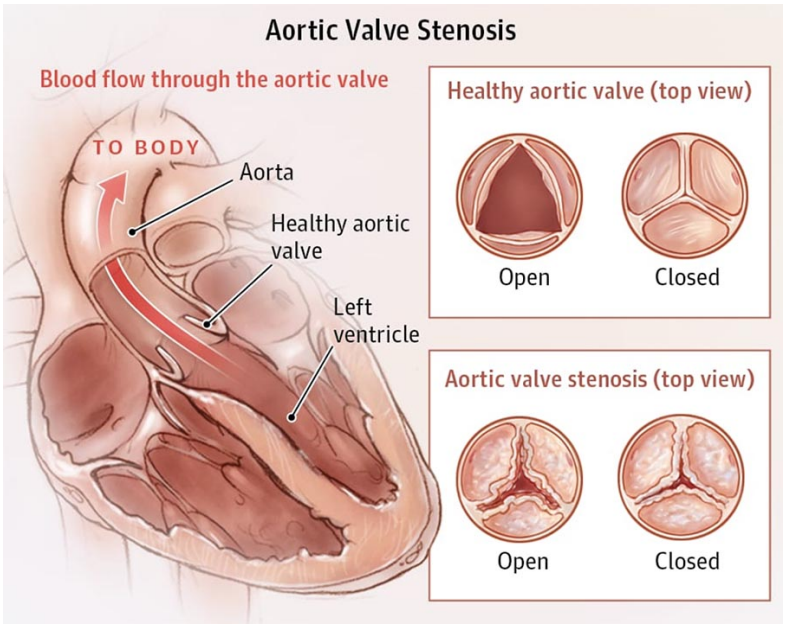

Figure 1.6: Aortic Stenosis [10]

The treatment of aortic stenosis has significantly evolved over the years, providing options that can be tailored to individual patient needs based on the severity of their condition, overall health, and specific medical requirements. The primary treatment strategies for aortic stenosis are Surgical Aortic Valve Replacement (SAVR) and Transcatheter Aortic Valve Replacement (TAVR).
Surgical Aortic Valve Replacement (SAVR): This traditional open-heart surgery involves removing the diseased aortic valve and replacing it with a mechanical or bioprosthetic valve. SAVR is generally recommended for younger patients or those with additional conditions that necessitate open-heart surgery. The choice between a mechanical or bioprosthetic valve is influenced by the patient's age, lifestyle, and willingness to adhere to long-term anticoagulation therapy, as mechanical valves require lifelong anticoagulation to prevent blood clots.

Transcatheter Aortic Valve Replacement (TAVR): A minimally invasive procedure that has revolutionized the treatment approach for elderly patients or those deemed at high or intermediate surgical risk. In TAVR, a bioprosthetic valve is delivered via a catheter through a small incision in the leg or chest and implanted within the existing aortic valve. TAVR is associated with quicker recovery times and less physical trauma compared to SAVR, making it an optimal choice for patients with multiple comorbidities or those of advanced age.

1.3.2 TAVR

Transcatheter Aortic Valve Replacement (TAVR) is a less invasive surgery developed in the early 2000s as an alternative to more traditional open-heart valve surgeries. It was first used for patients who couldn't undergo regular surgery. In this procedure, doctors insert a new valve into the heart through a small cut, usually in the leg or chest, without needing to open the chest or use a heart-lung machine. [11]

During TAVR, doctors use one of two main types of valves: balloon-expandable valves or self-expanding valves. Balloon-expandable valves are delivered to the heart via a catheter flexible tube threaded through the blood vessels. Once in place, a balloon at the end of the catheter inflates, expanding the new valve to fit securely within the old valve's space. This process effectively pushes the old valve's leaflets out of the way and secures the new valve in position. Self-expanding valves, on the other hand, are made from a material that expands on its own once the valve is deployed in the correct location. These valves are advantageous in that they can conform more closely to the patient's anatomy, providing a better fit and potentially reducing the risk of leakage around the valve edges. Both types of TAVR procedures are guided by advanced imaging techniques, allowing surgeons to visualize the valve's placement in real-time, ensuring optimal outcomes. The choice between a balloon-expandable valve and a self-expanding valve often depends on the specific anatomical and physiological needs of the patient, as well as the surgeon's preference.

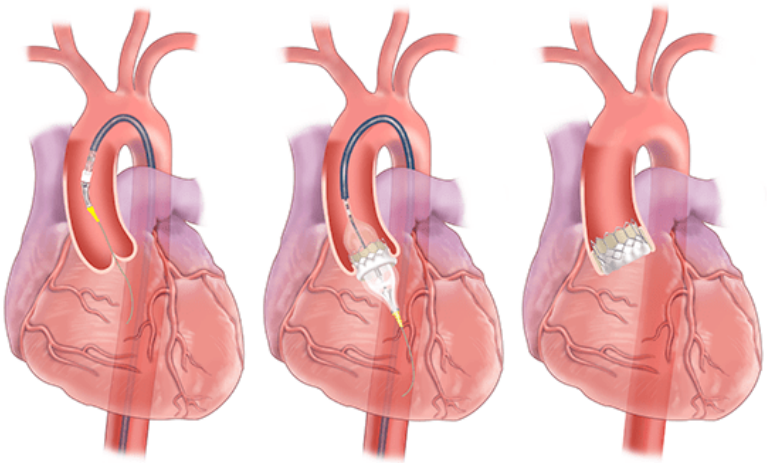

Figure 1.7: TAVR procedure [12]

This makes the recovery faster and easier, which is particularly helpful for older adults or those with other health issues. Over time, as more studies have shown how safe and effective TAVR is, it's become an option for more patients. As is possible to see in the figure below, TAVR drastically increased in number in the past years.[13]

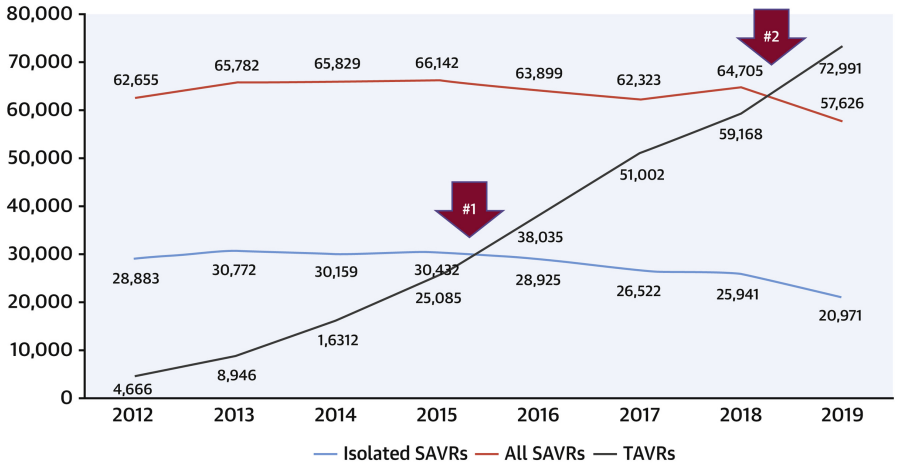

Figure 1.8: TAVR vs SAVR in recent years [14]

Research shows that TAVR can be as good as or better than traditional surgery in terms of survival, reducing stroke risk, and improving quality of life, especially for those who face higher risks with standard surgery. The simpler approach of TAVR reduces the stress of surgery and the risks of complications afterward.

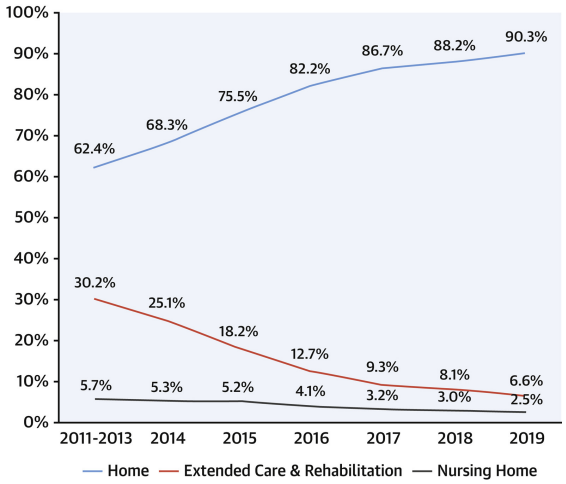

Figure 1.9: TAVR vs SAVR in previous years [14]

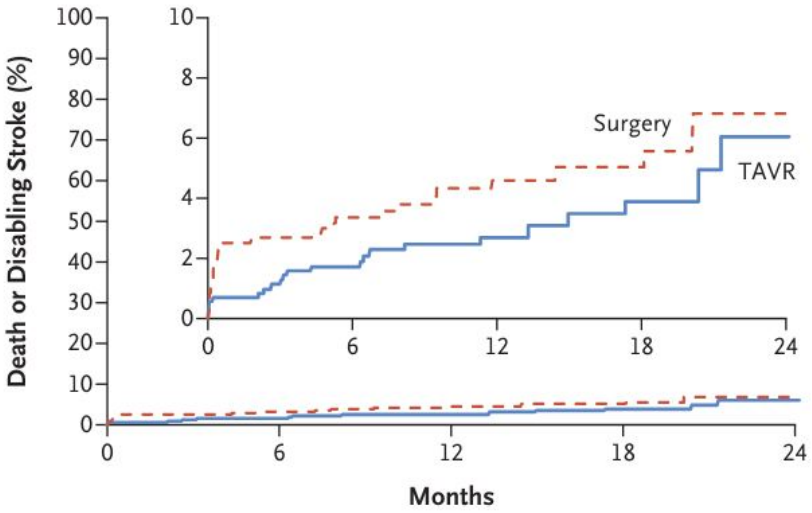

Figure 1.10: TAVR vs SAVR risks [15]

1.3.3 Paravalvular leakeage PVL

Paravalvular leakage (PVL) is one of the problem that can happen after valve replacement procedures like Transcatheter Aortic Valve Replacement (TAVR) or Surgical Aortic Valve Replacement (SAVR). PVL occurs when there is a leak around the valve prosthesis because it does not seal perfectly with the natural tissue of the heart. This issue allows blood to leak back into the chamber it came from, decreasing the heart's efficiency and potentially leading to serious health issues.
During the diastole phase of the heart cycle, the pressure difference across the closed valve can push blood through any small gaps between the valve frame and the surrounding tissue. If this happens with the aortic valve, blood flows back into the left ventricle, reducing how effectively the heart works and increasing its workload. If not addressed, this can result in heart failure and other serious heart problems.

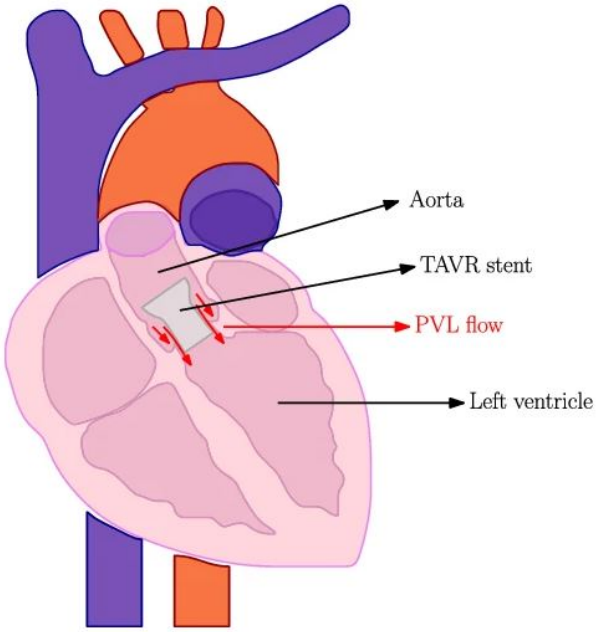

Figure 1.11: Schematic representation of the TAVR deployed in the aortic root geometry and the paravalvular leakage flow along the stent [16]

Paravalvular leakage (PVL) classification is crucial for assessing the severity of leaks that occur around prosthetic valves after heart valve replacement procedures such as Transcatheter Aortic Valve Replacement (TAVR). These classifications are instrumental in determining the potential impact on patient outcomes and guiding postoperative management.

Mild PVL: Represents the least severe form of leakage, involving minimal jet flows back into the heart. Although it may not present immediate threats, mild PVL can decrease long-term survival rates compared to patients without any leaks [17].

Moderate PVL: This level of severity leads to more noticeable cardiovascular symptoms and significantly affects the heart's efficiency.

Severe PVL: The most serious classification, where intense jet flows cause significant backflow into the heart. Severe PVL, although reduced by advances in valve placement techniques, poses substantial risks and necessitates immediate intervention [18].

Parameter	Category	Insignificant	Moderate	Severe
Prosthesis-Patient Mismatch (PPM)				
Indexed effective orifice area (cm^2/m^2)		>0.85	0.85–0.65	<0.65
Indexed effective orifice area* (cm^2/m^2)		>0.70	0.90–0.60	<0.60
Prosthetic Aortic Valve Regurgitation				
Diastolic flow reversal in the descending aorta – PW		Absent or brief early diastolic	Intermediate	Prominent, holodiastolic
Circumferential extent of prosthetic valve paravalvular regurgitation (%)**		<10%	10–29%	≥30%
Quantitative Parameters				
Regurgitant volume (mL/beat)		<30	30–59	≥60
Regurgitant fraction (%)		<30%	30–49%	≥50%
EROA (cm^2)		<0.10	0.10–0.29	≥0.30

Table 1.1: PVL evaluation criteria by The Valve Academic Research Consortium (VARC)

Despite advancements in technology, mild to moderate PVL still occurs in up to 19.7% of TAVR procedures due to issues such as imperfect valve sealing [18]. Properly categorizing the severity of PVL is vital for optimizing treatment and improving the outcomes for patients post-surgery. The application of advanced imaging techniques has allowed for more precise placement of the TAVR valve, ensuring a more accurate fit and reducing the potential for gaps between the valve frame and the native tissue where leaks could occur. Additionally, the evolution of valve designs to better match the anatomical complexities of the heart has played a critical role in minimizing the risk of PVL. These newer valves not only fit more securely but also integrate more effectively with the patient's cardiac tissue, providing a tighter seal.
Further contributing to the decrease in PVL rates is the improved screening process which ensures that the specific TAVR approach is optimally matched to each patient's unique cardiac structure. This tailoring of treatment reduces complications by addressing potential anatomical challenges before the procedure. The impact of these technological and procedural enhancements is evident in recent data, which shows a significant improvement in the survival rates of patients

with minimal to no PVL. While previous statistics highlighted that nearly one in five TAVR procedures could result in PVL, the refined approaches have led to a notable decrease in such outcomes. The survival data accompanying this discussion, which will be included in the thesis, underscores these advancements. Patients with trivial or no PVL demonstrate markedly better long-term survival and fewer complications compared to those with even mild PVL, emphasizing the importance of continuing to reduce PVL incidence through technological innovation and procedural refinement.

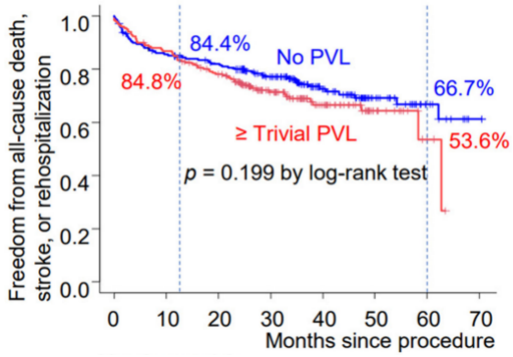

Figure 1.12: Free hospitalization about patitents affected by trivial PVL [19]

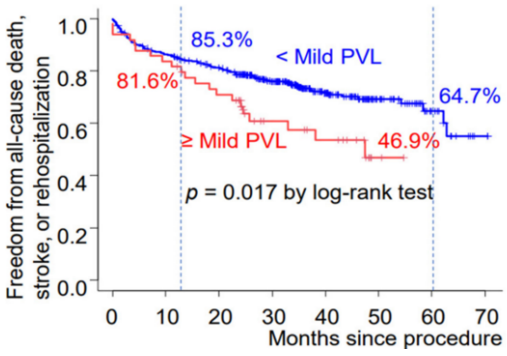

Figure 1.13: Free hospitalization about patitents affected by Mild PVL [19]

This progress highlights not only the advancements in medical technology but also underscores the necessity of ongoing research and development in the field of cardiology to further refine TAVR techniques, aiming to ensure even better outcomes for patients undergoing this life-saving procedure.

Chapter 2

Experimental setup

2.1 Left-Heart simulator

For the experiments, a custom-built left heart simulator assembled at Auburn University was used. This loop consisted of several key components: a Pulsatile Pump ViVitro, a mechanical valve in the mitral position, an em-tec flow meter that operates with ultrasounds, two pressure taps (one for the aortic side and one for the ventricular side), and a test chamber. The chamber is made of transparent acrylic, allowing for image recording with a camera and enabling the possibility of conducting PIV experiments. Additionally, the test chamber houses the heart valve. The loop included compliance chambers and resistance elements, which allowed for variation in the pressure on both sides of the test chamber, thereby controlling the flow rate. The loop was capable of maintaining different conditions by varying the aortic pressure from hypotension cases 60-100 mmHg to hypertension 120-160 mmHg and achieving flow rates with peaks up to 40 L/min. The Pulsatile Pump ViVitro was responsible for driving the fluid through the loop, pushing a defined quantity of fluid per cycle. The stroke volume (SV) could be adjusted by changing the pump's gain, while the heart period remained constant at 857 ms, corresponding to a heart rate of 70 beats per minute. A camera with an high frame-rate, the Phantom VEO 4K 990L, was used to facilitate the PIV measurements. This camera enabled the capture flow dynamics in the test chamber using the PIV method. The pressure taps were connected to two amplifiers, which were then linked to an analog deck connected to a dedicated LabVIEW code for data acquisition. Typically, data were acquired and then phase-averaged over 50 cycles to minimize noise and oscillations. The sample frequency was set at 2000 Hz.

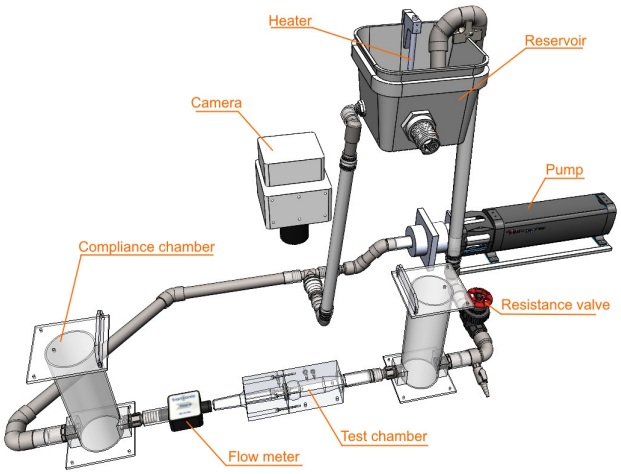

Figure 2.1: Left Heart simulator

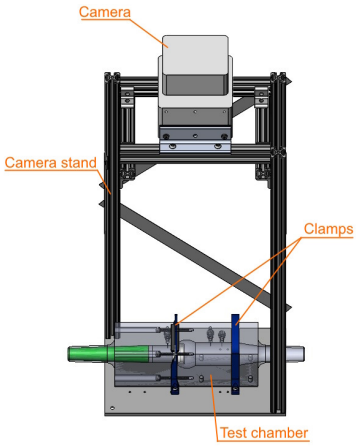

Figure 2.2: Camera and Test Chamber tower

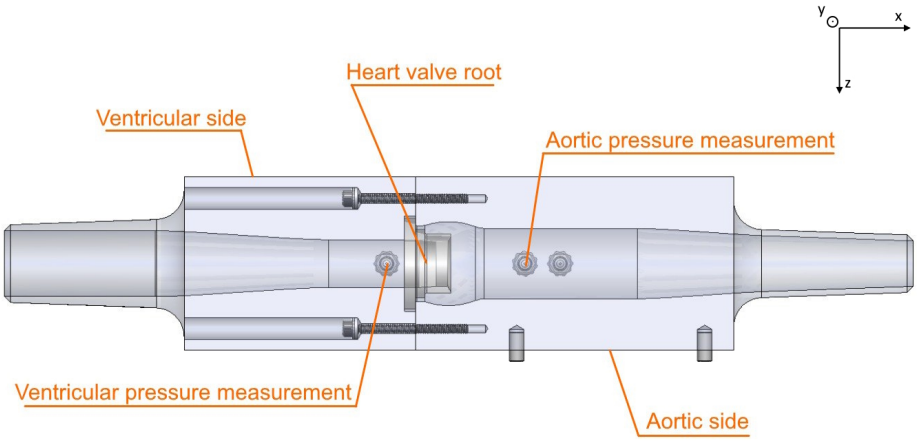

Figure 2.3: Test Chamber

2.2 Working Fluid

The working fluid in the heart loop is a water-glycerin mix, specifically selected to mimic the viscosity and density of blood. The mixture consisted of 36% glycerin and 64% water, with an addition of 9 grams of salt (NaCl) per liter of water to closely replicate the properties of human blood. The fluid's viscosity was measured at 3 cPa and its density at 1.1 kg/m^3, both evaluated experimentally using a viscometer for viscosity and appropriate methods for density measurement. Stored in a filling bucket, the fluid is consistently maintained between 96 and 100 degrees Fahrenheit (approximately 37 degrees Celsius) by a heater to ensure the fluid's properties remain consistent with those of human blood. The total quantity of fluid within the loop is approximately 10.5 liters, providing sufficient volume to simulate the circulatory system's dynamics effectively.

2.3 Heart Valve and nodules

2.3.1 Heart Valve

The heart valve for our experiments was sourced from an external company, which supplied a real valve used during TAVR with an external diameter of 29mm. Along with the valve, the company provided a silicone jacket designed to emulate the natural tissue surrounding a heart valve. This silicone jacket is essential as it houses the valve, and the combined valve-jacket assembly is then placed within the acrylic heart chamber. This setup provides a realistic environment for studying the valve's functionality.

2.3.2 Nodules

The nodules used in the described setup are placed between the valve and the silicone jacket. Made from rigid PLA and 3D printed, these nodules are designed to slightly deform the heart valve tissue, creating spaces where paravalvular leakage (PVL) can occur. Initially, nodules were designed as per ISO guidelines with a thickness of 1.5 mm.

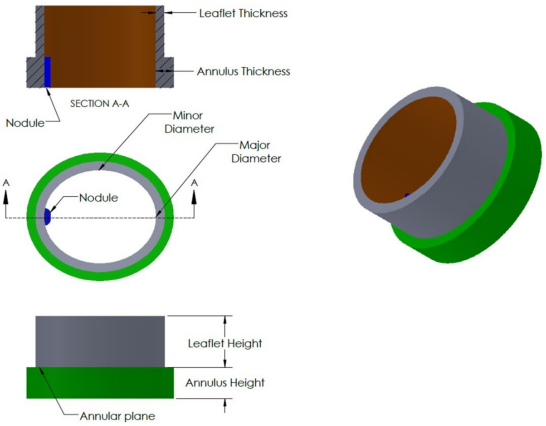

Figure C.1 – Representative schematic of TAVI hydrodynamic test fixture

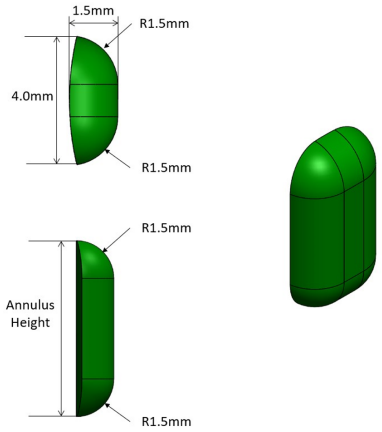

Figure C.2 – Schematic of simulated calcification nodule for TAVI hydrodynamic test fixture

Figure 2.4: ISO Nodule document

However, to achieve consistent PVL, the thickness of these nodules was increased to 3 mm, 4 mm, and 5 mm, while maintaining the original ISO shape. Adjusting the thickness was crucial for observing the effects of more pronounced calcific deposits on the functionality of heart valves and their potential to cause significant PVL. An increasing in RF and PVL was evident.

2.4 Particle Image Velocimetry (PIV)

Particle Image Velocimetry (PIV) is an optical method that measures fluid flow velocities by tracking the movement of seeded particles. The system provides high spatial and temporal resolution, making it ideal for analyzing flow patterns. The spatial resolution depends on the optical setup and the seeded particles size. It is determined by the size of interrogation windows used for analyzing particle displacement while the temporal resolution is influenced by the camera's frame rate and the pulse frequency of the light source. A high frame rate allows capturing

rapid changes, thus measuring transient and turbulent flows. A typical PIV system includes the following components:

- **Illumination Source:** Usually a laser that generates a thin light sheet to illuminate the flow particles, producing high-contrast images.
- **Seeding Particles:** Small particles introduced into the flow to act as markers. They should match the fluid density and optical properties for precise flow tracking.
- **Camera:** Captures high-speed images of the particles illuminated by the laser.
- **Synchronization and Processing System:** Aligns the laser pulses with the camera frames. Cross-correlation algorithms then analyze the displacement between frames to calculate flow velocities.

The basic equation for calculating the velocity field using PIV involves the displacement of particles over time:

$$\mathbf{u} = \frac{\Delta \mathbf{x}}{\Delta t}$$

where $\mathbf{u}$ is the velocity vector, $\Delta \mathbf{x}$ is the displacement vector of the particles in an interrogation window and Δt is the time interval between two successive images. The cross-correlation method used for PIV analysis is mathematically expressed as:

$$C(\Delta \mathbf{x}) = \int_W I_1(\mathbf{x}) I_2(\mathbf{x} - \Delta \mathbf{x}) d\mathbf{x}$$

Where $C(\Delta \mathbf{x})$ is the cross-correlation function, I_1 and I_2 represent image intensity functions for the two successive frames and W denotes the interrogation window. The equipment used for the PIV experiments included a Phantom VEO 4K 990L camera and a Photonics Industries DM30-507DH laser. Seeding particles with diameters between 30 and 50 micrometers were introduced into the flow, and the acquired data was processed using Davis software. The figure below shows a scheme of the PIV setup.

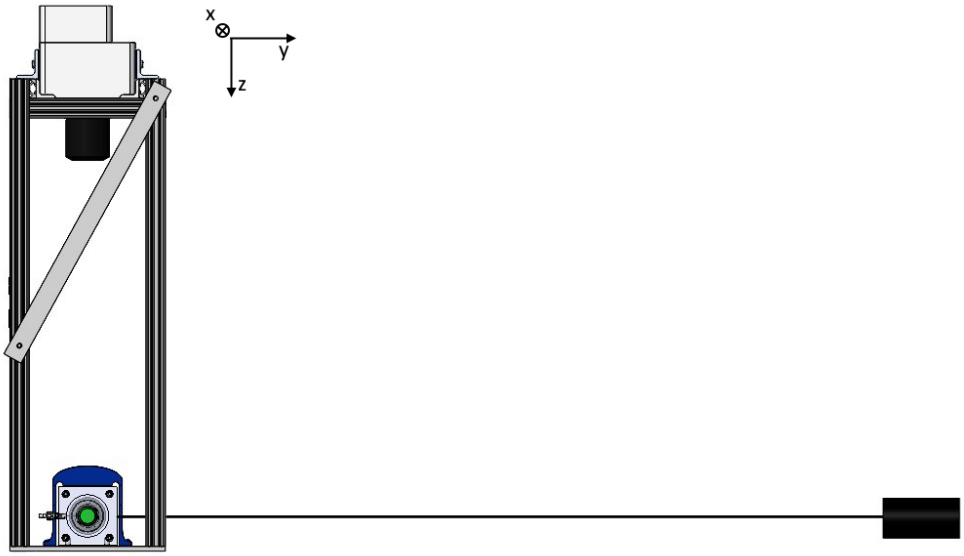

Figure 2.5: Planar PIV setup side view

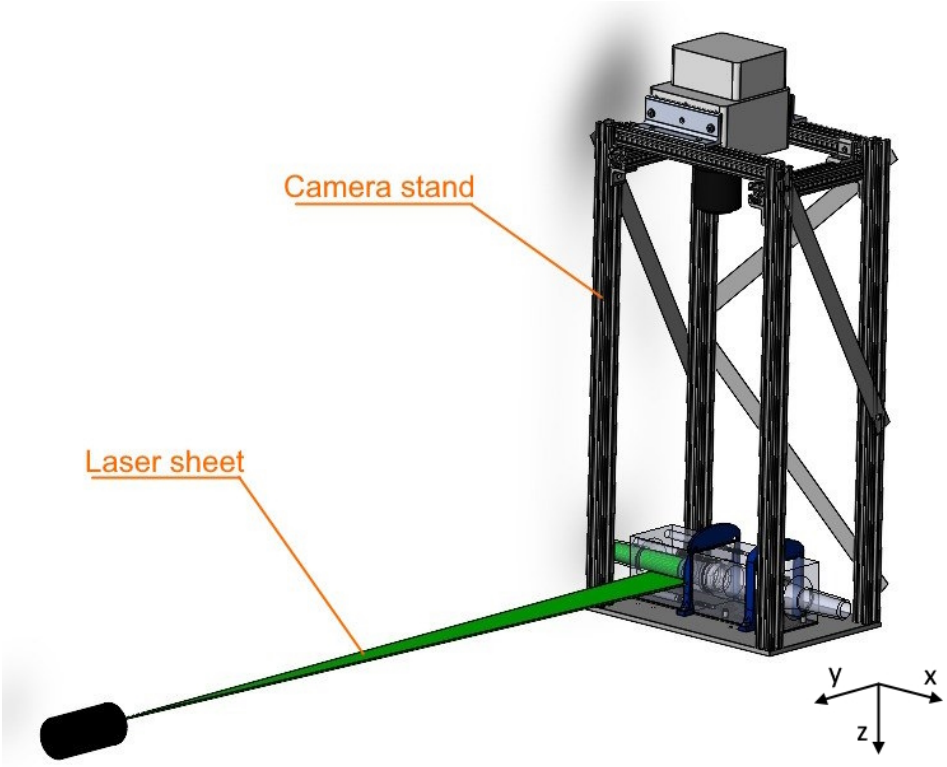

Figure 2.6: Planar PIV setup axonometry

It is possible to classify PIV among different methods:
Planar PIV Planar PIV is the most straightforward and widely used PIV technique. It illuminates a single plane within the flow using a laser light sheet, and a camera captures images of tracer particles suspended in that plane. Planar PIV provides high spatial resolution within the illuminated plane and is suitable for studying two-dimensional flow phenomena.
Stereo PIV Stereo PIV combines elements of planar and tomographic PIV techniques to capture three-dimensional velocity fields with higher spatial resolution. Two cameras with overlapping fields of view capture images of tracer particles from different perspectives. Stereo PIV offers higher spatial resolution compared to tomographic PIV within individual planes and is suitable for studying complex flow structures in confined spaces.
Tomographic PIV Tomographic PIV extends planar PIV to capture three-dimensional velocity fields within a volume of interest. Multiple cameras are arranged around the flow field to capture images from different viewing angles, which are then reconstructed into a three-dimensional volume. Tomographic PIV provides comprehensive analysis of complex flow structures.

2.4.1 Plenoptic PIV

The plenoptic camera, also known as the light field camera, captures not only the intensity of light rays but also their direction, enabling the capture of a light field. Several methods exist for capturing light fields, such as mounting a camera on a gantry to take multiple photos at different positions, using a large array of cameras (as in tomo-PIV or synthetic aperture PIV). In a conventional camera, the sensor plane integrates angular information, leading to the loss of this data, and records only the spatial information about incident light rays. This integration results in focused images when the sensor plane aligns with the image plane. In the conventional camera the directional information of light ray is lost because light from multiple angles are focused onto a point. In contrast, a plenoptic camera uses a microlens array positioned a focal lenght infront of sensors. This setup allows each microlens to direct light incident at a particular angle onto specific pixels behind it, capturing both the position and angle of the light rays [20]. To develop the plenoptic PIV technique, a prototype plenoptic camera was constructed using an Imperx Bobcat ICL-B4820 camera as the base, equipped with a Kodak KAI-16000 image sensor. This sensor was chosen for its high resolution and ability to perform double exposures, similar to traditional PIV cameras. The microlens array, fabricated by Adaptive Optics Associates, was precisely mounted above the sensor using a custom-designed mounting device to ensure accurate positioning. Each pixel in a plenoptic camera captures a part of the light field, represented as $L(x, y, \theta, \phi)$, where

(x, y) denotes the position of the light ray in the object space and (θ, ϕ) denotes the angle at which the ray enters the camera. Alternatively, pixels can be considered as sampling parts of the aperture, described by coordinates (u, v). In this two-plane parameterization, each pixel's information is represented as $L(u, v, s, t)$, with (s, t) corresponding to the microlens position. This approach is useful for interpolation since the bounds of each pixel are defined by the aperture, making the processing more straightforward. [21] Using this two-plane parameterization, we gain several benefits from the plenoptic camera. It allows us to generate different perspective views and refocus images after they are captured. Additionally, it is a less invasive method since only one camera is needed to achieve these effects.

Chapter 3

Methodology

3.1 Calibrations

To ensure accurate measurements in experimental setup, both the pressure taps and the flow meter have been calibrated. Let's describe the calibration methods used for these instruments.

3.1.1 Pressure taps calibration

The necessary equipment includes a Delta-Cal transducer, a pressure transducer with a strain gauge, an amplifier, an analog input module, and a laptop with LabVIEW software. The Delta-Cal Transducer generates and measures pressure by adjusting air within a connected pipe. The pressure transducer detects pressure changes and outputs varying voltages. An amplifier boosts these low voltage signals for readability, and the analog input module converts them into digital values for use in programs. LabVIEW software records voltage values corresponding to pressure, builds a linear regression, and evaluates the slope, which is saved as the calibration constant. 5 points are taken and then is possible to build the linear regression and evaluate the calibration constant. Calibration Data are here reported.

Ventricular Pressure (Pa)	Voltage (V)	
1st point	0	0.092
2nd point	26	1.457
3rd point	54	2.914
4th point	88	4.654
5th point	118	6.160

Table 3.1: Measurement points for channel 4

Aortic Pressure (Pa)	Voltage (V)	
1st point	0	0.050
2nd point	20	0.866
3rd point	48	2.054
4th point	84	3.560
5th point	121	5.091

Table 3.2: Measurement points for channel 3

Channel	Calibration constant	R-squared
3	19.439	0.9999
4	23.839	0.9998

Table 3.3: Calibration constants and R-squared values for channels 3 and 4

Each transducer is connected to an amplifier and an analog input module: the aortic pressure transducer to Amplifier 1 and Channel 3, and the ventricular pressure transducer to Amplifier 2 and Channel 4. When data were acquired, it was important to check that the pressure tap calibration was not older than 7 days.

3.1.2 Flow meter calibration

To begin with, the calibration process requires specific equipment: a Transonic Flow Meter, a regulable pump, a TS410 tubing flow module, a bucket and stopwatch and a laptop with LabVIEW software. The Transonic Flow Meter measures flow and provides a voltage signal as output. The regulable pump creates a flow inside the pipes, which can be adjusted to regulate the flow meter accordingly. The TS410 tubing flow module converts analog signals from the flow meter to digital

values for use in programs. A bucket and a stopwatch are used to collect a specific quantity of water and measure the time required to fill it accurately. The LabVIEW software records voltage values corresponding to specific flow measurements. The procedure begins by constructing a basic loop consisting of the pump, pipes, and the Transonic Flow Meter to generate a flow passing through the flow meter. The flow meter is connected to the tubing flow module, which is connected to the laptop with the LabVIEW code, enabling the reading of voltage values associated with the specific flow meter. Data collection involves selecting a predefined power setting for the flow meter and recording the corresponding voltage. The process continues by filling the graduated bucket while simultaneously starting the stopwatch. Once the bucket is adequately filled, the stopwatch is stopped, and the volume (in liters) and the time (in seconds) are recorded. This process is repeated multiple times, each corresponding to different voltage values. Three measurements are taken for each point, and the average is calculated. Flow meter values of around 5 L / min are used to ensure greater accuracy for calibration. At this stage, the LabVIEW code provides the slope and the R-squared value as output. It is crucial to ensure these values are logical, particularly the R-squared value. If the data is valid, the calibration constant, corresponding to the slope, is saved. Data from the Flow Meter Calibration are reported:

Table 3.4: Flow meter calibration Data Points

Point	Voltage (V)	Volume (L)	Time (s)	Flow (L/s)
1st	0.937	2	16.61	0.120
2nd	2.103	3	10.09	0.297
3th	4.701	3.5	5.86	0.597
4th	3.524	3.5	8.33	0.410
5th	3.592	3.5	7.67	0.457

Table 3.5: Calibration Data

Calibration Constant	R-squared
7.147	0.9902

3.2 Initial test

In the initial test, only some data were collected, varying the cardiac output and the nodule size. The purpose of this initial test was to determine which cardiac output and nodule sizes were suitable for generating mild to intermediate PVL. This preliminary assessment was crucial for defining the test matrix used in the subsequent PIV experiments. During this phase, different nodule sizes were analyzed: 3 mm, 4 mm, and 5 mm. However, the largest size (5 mm) resulted in severe PVL, making it unsuitable for our study. Data were collected using LabVIEW, leveraging the connection setup described in the previous chapter for the flow meter and pressure taps. Specifically, data were recorded for nodule sizes of 3 mm, 4 mm, and 5 mm, each under three different cardiac outputs: 3.5 L/min, 5 L/min, and 6.5 L/min. This initial stage allowed us to quantify PVL volumes under various conditions, providing valuable insights that informed the direction of our work. The findings from this preliminary test were instrumental in refining the experimental parameters and establishing a test matrix for the PIV experiments.

The data acquisition involved using a dedicated LabVIEW code to collect data from the pressure taps and flow meter. After processing this data, it was possible to evaluate the PVL, RV, RF, and EROA for each cycle and classify the leakage. The test matrix considered plausible cases, excluding those with an RF greater than 50%.

3.3 PIV

3.3.1 Test Matrix

The test matrix used features three different cardiac outputs with two different nodule sizes plus a refernce condition without using a nodule. When using a cardiac output (CO) lower than 5 L / min, it represented a case of hypotension, while a CO greater than 5 L / min represented a case of hypertension. By tuning the left heart simulator, it was possible to change aortic pressure by modifying compliance and resistance in the loop. In the test matrix, the aortic pressure used during that specific condition is reported.

Cardiac Output (L/Min)	3mm	4mm	No Nodule
3.5 (Hypotension)	60-100	60-100	60-100
5	80-120	80-120	80-120
6.5 (Hypertension)	120-160	120-160	120-160

Table 3.6: Test Matrix

This test matrix was employed for both planar PIV and plenoptic PIV experiments.

3.3.2 Planar PIV Procedure

The experimental setup used was detailed in the previous chapter. First, the nodule was correctly positioned and the heart valve-silicone jacket-nodule assembly was placed in the heart chamber. Before starting the experiments, it was necessary to set up the left heart simulator and tune it to the desired conditions, including the correct cardiac output and aortic pressure. Additionally, the laser needed to be aligned with the center plane, and the camera had to be positioned correctly to ensure the desired field of view.
Finally, planar PIV data was acquired. A sheet of light from the laser illuminated the central plane of the test chamber. The camera view was perpendicular to the laser sheet, and the frame rate was 400 Hz. The basic principle of PIV involves illuminating a seeded flow-field with two laser pulses and capturing the particle images with a CCD camera. Traditionally, both exposures are recorded on a single frame, creating a double exposure processed using auto-correlation. However, this method causes directional ambiguity because it cannot distinguish which particle images correspond to each laser pulse. Image shifting using a rotating or spinning mirror can address this ambiguity but adds experimental complexity. An improved technique, known as Frame-Straddling, records each laser pulse on separate frames, analyzed using cross-correlation. This method preserves the time sequence of the pulses, eliminating directional ambiguity and providing a better dynamic range for velocity measurements compared to the double exposure method. For the planar PIV experiments, the frame-straddling technique was employed.

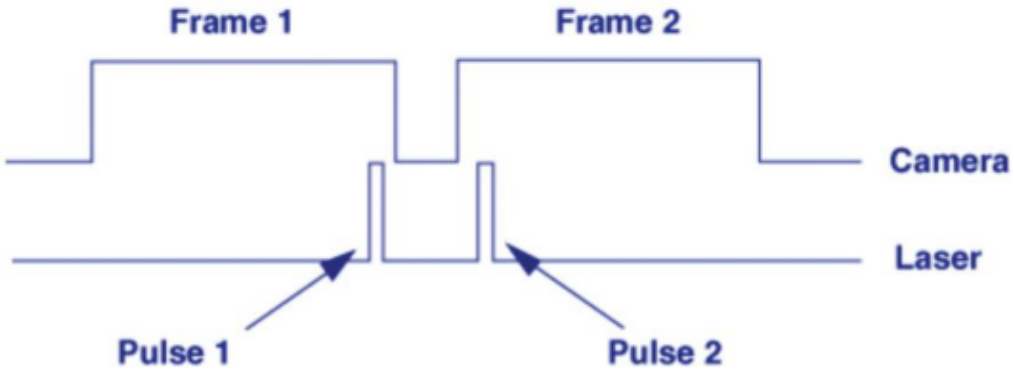

Figure 3.1: Frame strudelling PIV time exposure

Before data acquisition, some tests were performed to ensure that the correct dt was used. After these preparations, data were acquired.
Later, to obtain 3D information, a plenoptic camera was used due to space constraints that prevented the use of multiple cameras for a tomographic PIV setup.

3.4 Plenoptic PIV

Before starting the final experiments using a plenoptic camera, it was necessary to calibrate the volume to analyze. Calibration is essential to define the volume under study. The calibration process for the plenoptic camera involves using a pattern that is repeated at different z positions within the calibration volume, using non linear interpolation is possible to define the rest of the volume. In details, the used calibration method was Direct Light-Field Calibration (DLFC). The Direct Light-Field Calibration (DLFC) method aims to calibrate the recorded light field directly during the reconstruction of the volume, bypassing the need for dewarping as a post-processing step. The goal is to create a mapping from any point in 3D space (X, Y, Z) to a light-field coordinate $L(u, v, s, t)$. This is achieved by relating calibration points in 3D space to locations on the aperture and microlens planes, using perspective views with fixed (u, v) coordinates to determine corresponding (s, t) coordinates. The calibration function P maps points in object space directly to the microlens plane, defined as:

$$(s, t) = P(X, Y, Z, u, v)$$

This involves generating perspective images for each calibration point and recording the dot locations in (s, t) space for each depth position. A matrix A is then created from the object locations and projection angles, and the projection coefficients are determined using least-squares fitting. During volume reconstruction, the synthetic photography equation is modified by replacing linear projection operations with a best-fit polynomial, treating each perspective view as a separate camera. This method assumes ideal (u, v) coordinates and consolidates all calibrations into a single polynomial, accommodating microlens aberrations. A third-order mapping function was used. [22] The pattern must appear consistent at each z position. To create an effective calibration pattern, alternating zones of dark (low intensity) and light (high intensity) areas are used on the calibration plate. This design allows the plenoptic camera to recognize the pattern even when it is out of focus at various z positions. The focus for the calibration process was set on the central plane of the volume. The calibration had to occur under the same conditions as the experiments, so the same water-glycerin mixture was used, maintained at the same temperature and same conditions. The calibrated volume was cylindrical and naturally located in the ventricular side where the experiments occur. Due to the inability to access different positions within the cylinder easily, a complex and frequently revised setup was employed. This section explains the evolution of this calibration setup.

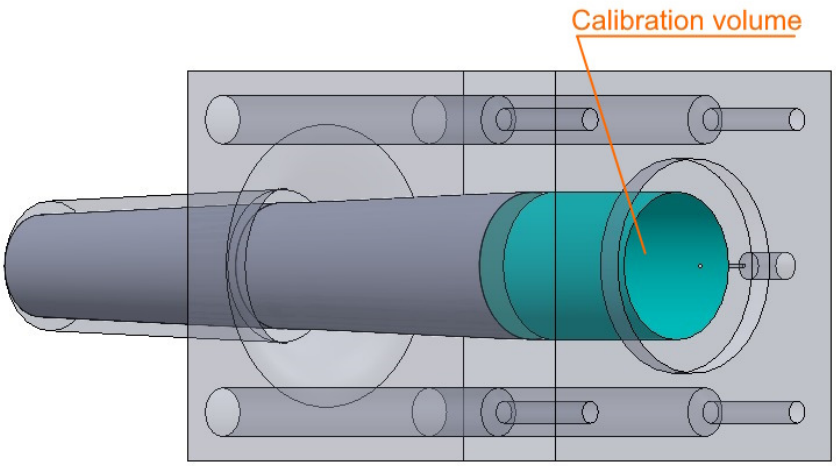

Figure 3.2: Calibration Volume

3.4.1 First setup

To facilitate the calibration process, the aortic side was removed and replaced with a custom-designed bucket. This bucket needed to be rigid, impermeable, and securely sealed at the interface with the ventricular side. Additionally, it had to provide sufficient space to accommodate the calibration plate inside. The calibration bucket was 3D printed using PETG as material.

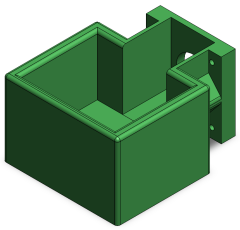

Figure 3.3: Calibration Bucket view 1

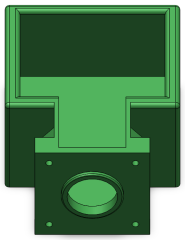

Figure 3.4: Calibration Bucket view 2

The calibration plates were originally designed with a square pattern created using laser engraving. However, the results were not sufficiently accurate due to high distortion of square pattern in our setup and accuracy limitations of the laser engraver. Consequently, a new dot pattern was developed. The initial plan involved creating holes in the calibration plates and filling these holes with white plumber's putty or paint. To calibrate the entire volume, plates of varying widths were needed, as the width required changes with the z position in a cylindrical section. The main challenge was ensuring that all calibration plates were centered in the same position, with the pattern shift limited to a maximum error of 25-50 micrometers (1-2 thousandths of an inch). This precision was crucial for reconstruct our volume with the researched accuracy. Additionally, we had to consider that the camera is calibrating the upper plane of the plate where the pattern is. A special plate design was conceived, providing plates with a step. By flipping the plate and replicating the same pattern on the other face, we were able to calibrate different z positions per plate without changing the width of the plate.

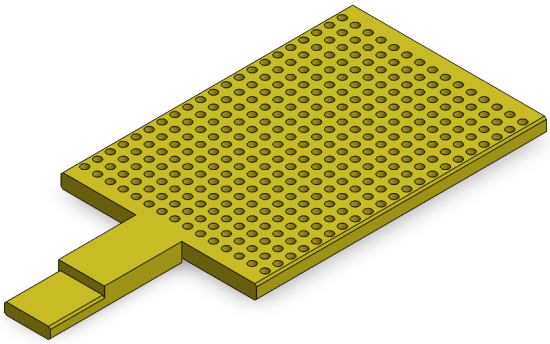

Figure 3.5: Calibration Plate Size L first setup

To achieve precise alignment, a calibration array was designed, ensuring that each plate could be positioned exactly where needed. This array has five slots where plates can fit in, and by flipping the plates, this setup allows us to calibrate 10 planes using three plates of different widths. A calibration support was designed to align the calibration array. This support is glued to the bucket and made of aluminum, allowing the array to be pushed into the corner and aligned using three contact surfaces. Directly using the bucket for alignment was not feasible because it is 3D printed, with tolerances around half a millimeter, which is insufficient for the required alignment accuracy.

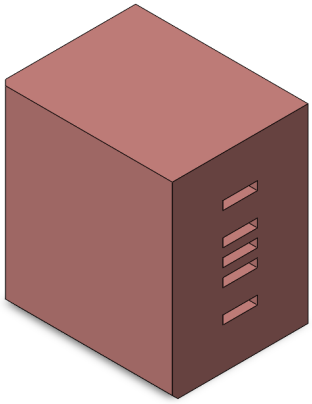

Figure 3.6: Calibraton Array

However, due to the small size of the setup, 29 mm in diameter and 40 mm in length, the calibration array had to be machined from any available material to meet the design specifications. Consequently, design modifications were necessary to accommodate these constraints.

3.4.2 Second setup

In the second design, several changes were made to address the shortcomings of the initial approach. The idea of using a calibration array was deemed unfeasible, necessitating an alternative solution. The new approach involved using a calibration support and calibration blocks to position the calibration plates accurately. Calibration support, calibration blocks, and calibration plates were machined from high-tolerance aluminum to achieve the required precision. The calibration support, glued inside the bucket, provided three contact surfaces for the plates, ensuring proper alignment. The ground blocks were instrumental in adjusting the z position of the plates by stacking them to change the z position of the calibration plane. However, this second design faced challenges with the calibration plates. The small dimensions of the pattern required an intercenter distance of 0.07 inches and a diameter of 0.04 inches for each dot. Additionally, a step in the design, illustrated in the accompanying figure, was complex and expensive to machine. Further revisions are needed to refine these calibration plates and address these issues.

3.4.3 Final setup

In conclusion, the previous setup was retained, but some modifications were made to the calibration plate. Specifically, the discussed step was removed, and an easier design for the plates was developed. The plates were machined from a 1/16 inch aluminum sheet with tight tolerances. The part was squared to ensure it could be worked on just one plane. Due to the removal of the step, a new set of plates classified by size (XS, S, M, and L) was introduced. Some chambers on the plate edges were made to avoid scratching the test chamber while positioning the plate. Here is a representation of how these plates fit inside the pipe for calibration.

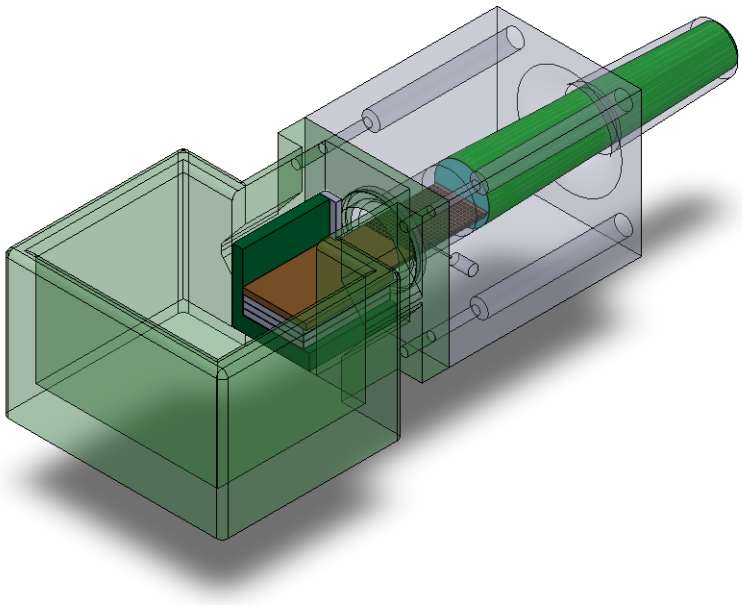

Figure 3.7: Calibraton setup assiem view 1

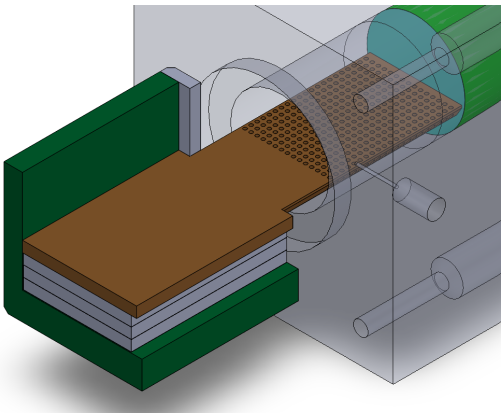

Figure 3.8: Calibraton setup assiem view 2

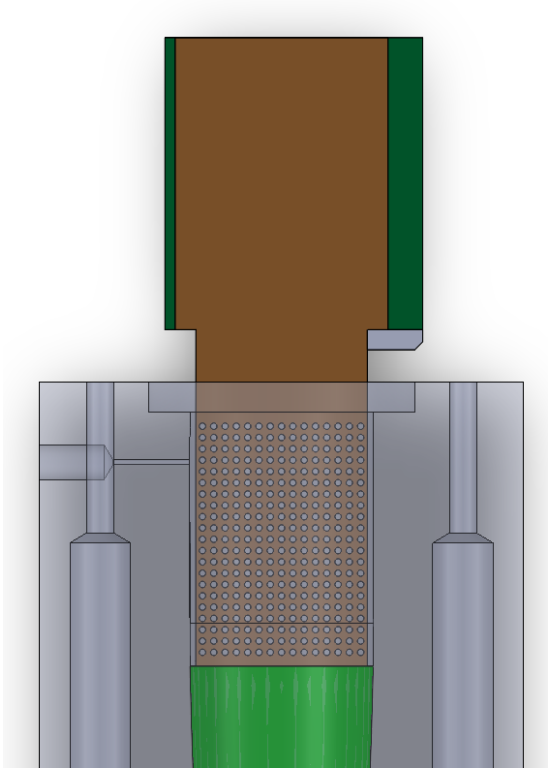

Figure 3.9: Calibraton setup assiem top view

The pattern remained a dot pattern, maintaining the same number of rows for each plate: 36. However, the number of columns varied depending on the plate size. Recently, a special hydrophobic black paint was used to fill the holes, achieving the desired contrast of black (paint) on grey (aluminum). In the following table are reported the details of the designed plates:

Table 3.7: Details plates

	XS	**S**	**M**	**L**
Width (inches)	0.374	0.700	0.920	1.064
Number of column dots	5	9	13	15

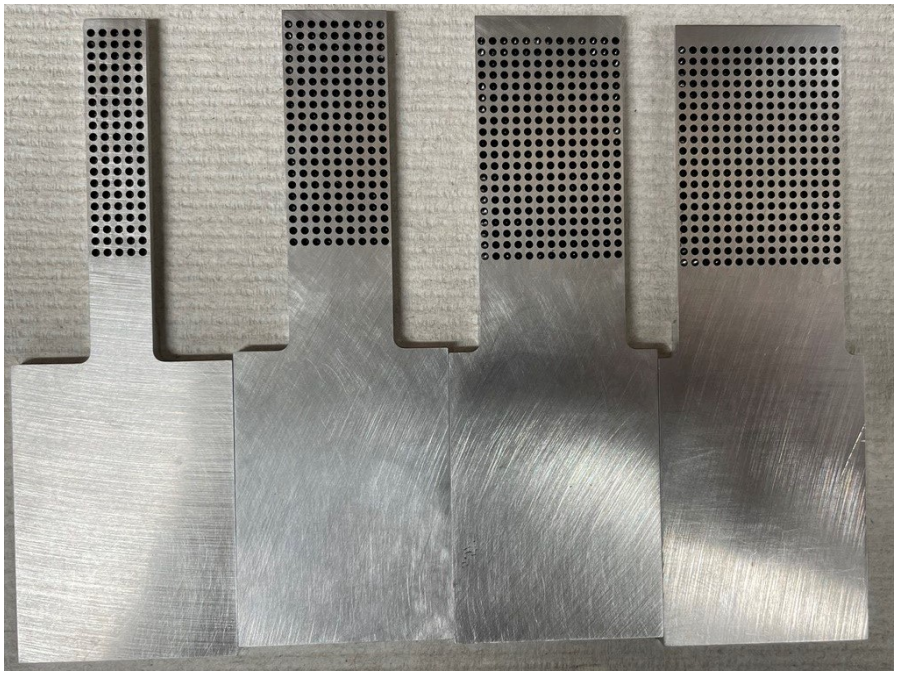

Figure 3.10: Calibraton Plates after painting

In the appendix is possible to find all the drawings about the discussed setup.

3.4.4 Procedure

The calibration procedure began by gluing the machined calibration support inside the bucket using epoxy resin to bond the aluminum with PETG. Once secured, the aortic side of the heart chamber was removed, and the bucket was attached. After ensuring that the bucket was tightly sealed with the ventricular side, the water-glycerin mixture was added.

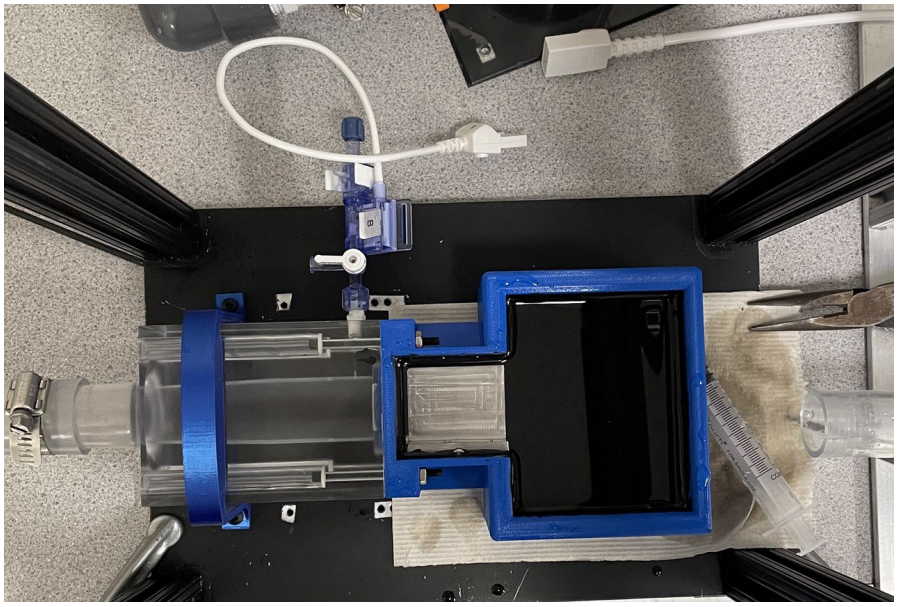

Figure 3.11: Calibraton setup

Next, the illumination source and the plenoptic camera were positioned. Calibration blocks were used to adjust the height to the center plane, where the L-size calibration plate was placed. The plenoptic camera was then focused and calibrated with this setup. Alignment was ensured by manually pushing the stacked calibration blocks and the calibration plate into the corners of the calibration support.

Figure 3.12: Calibraton setup

This procedure was repeated for all the necessary calibration planes. After completing the calibration, without altering the camera or the ventricular side of the chamber (which was clamped to the camera stand), the bucket was removed and the aortic side was reattached. The left heart simulator was started, and the setup was prepared for data collection in the experiments. For the plenoptic PIV, phase-locked PIV was employed. Specifically, 10 different phases were chosen during diastole, and each phase was averaged over 200 cycles to improve accuracy.Using

the laser, the entire calibrated volume was illuminated, ensuring comprehensive data capture across the region of interest. The chosen phases are equispaced during diastole, with the first and last phases capturing key transitional points. This approach ensures a thorough examination of the flow throughout the diastolic period. Data were acquired for all six configurations shown in the test matrix. The phase-averaged PIV technique involves capturing multiple images at each phase point and averaging them to obtain a representative flow field, thereby reducing random fluctuations and enhancing the clarity of the flow dynamics. The data were acquired for all the 6 configuration shown in the test matrix.

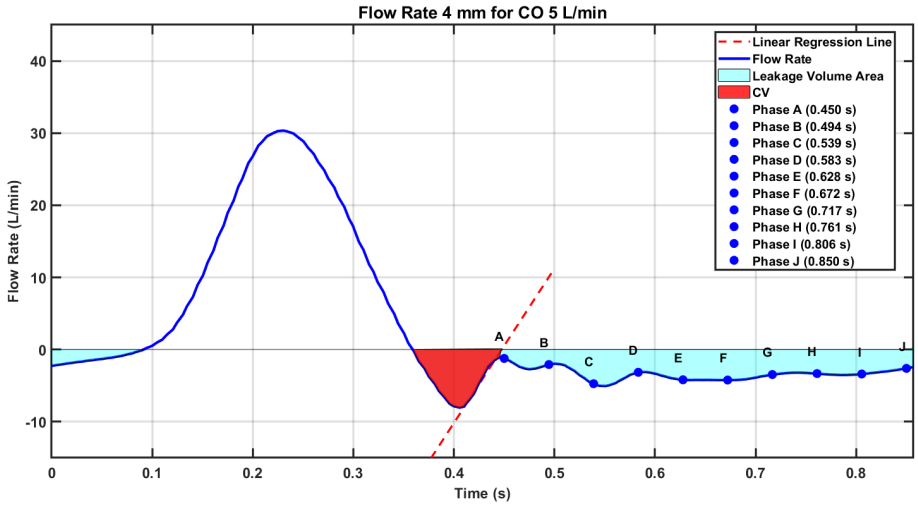

Figure 3.13: Phases used during plenoptic PIV experiments

The data were acquired for all the 6 configuration shown in the test matrix.

Chapter 4

Results

Initially, a preliminary test was conducted to identify the specific entities of PVL involved in the study. Three different nodule sizes were tested, 3mm, 4mm, and 5mm. The hemodynamic parameters were evaluated for each condition, specifically Stroke Volume (SV), Closure Volume (CV), Effective Regurgitation Orifice Area (EROA), Regurgitation Fraction (RF), and Leakage Volume, following the definitions provided in Chapter 1. The focus was on analyzing these data using the parameters commonly employed to classify PVL: RF, leakage per beat, and EROA. The PVL classification follows table 1 reported in chapter 1.

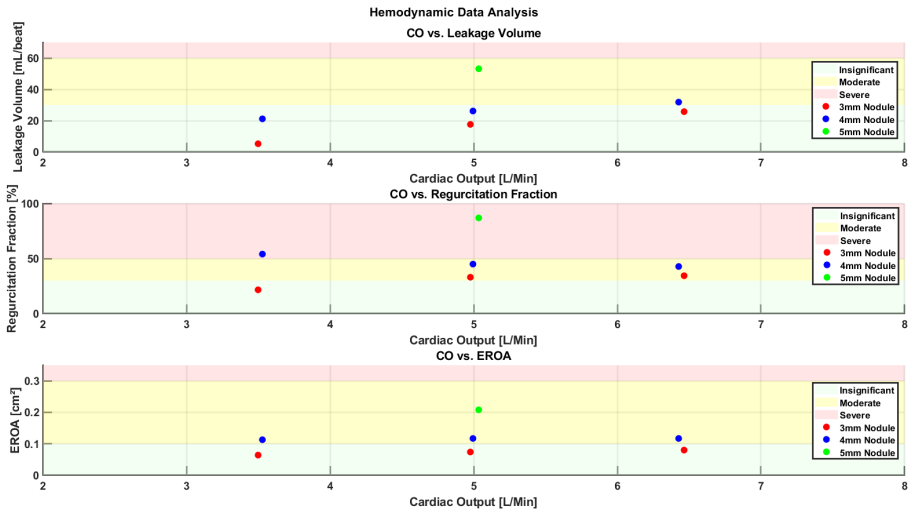

Figure 4.1: Initial test results

As the above plot shows, for the 5mm nodule, the regurgitation volume was approximately 90%. This means that around 90% of the direct flow going through

the aortic valve during systole is returning during diastole. This condition was far from realistic patient conditions or, at the very least, represented an extreme condition not of interest for this analysis. Consequently, the nodule sizes chosen were 3mm and 4mm, which classifies them as mild to moderate leakage. The hemodynamic data are reported below; in this chapter, only the condition at 5 L/min is reported. All other performed tests are detailed in the appendix.

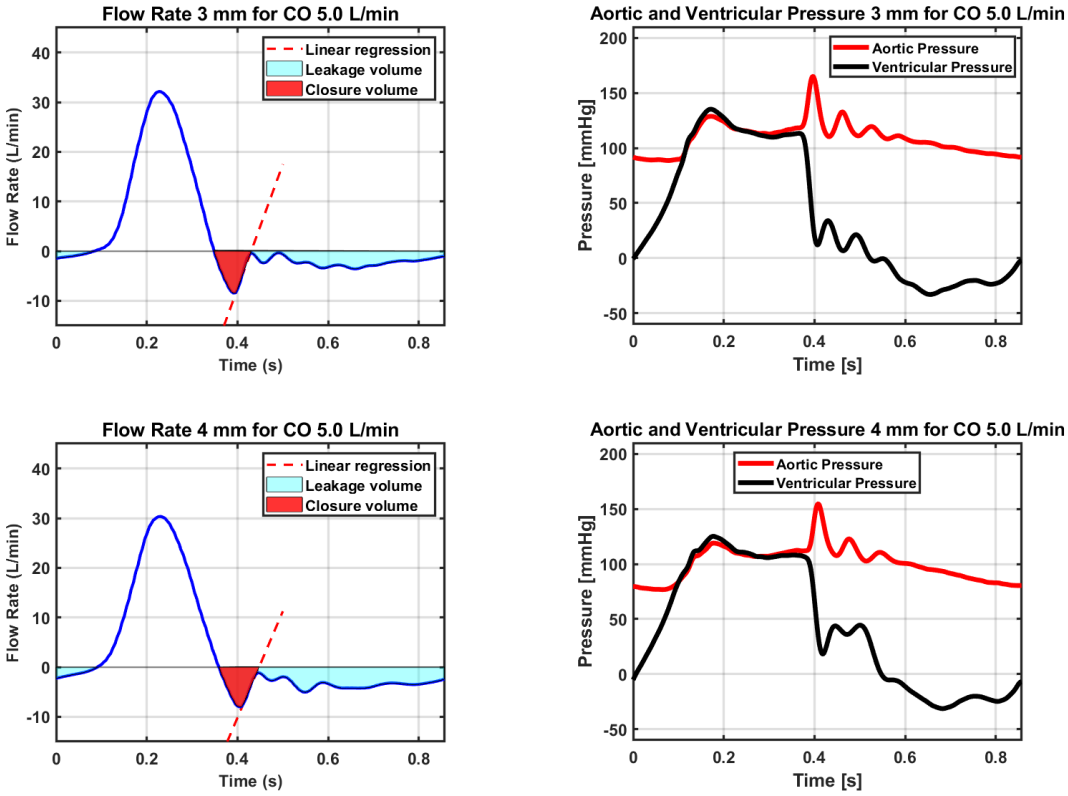

Figure 4.2: Hemodynamic Flow rate 5 L/Min Nodule size 3 mm

To evaluate quantities such as Stroke Volume (SV), Closure Volume (CV) or Leakage Volume (LV), basic integration method were adopted on the Flow rate curve. Also the following fromula was used to evaluate EROA:

$$\text{EROA} = \frac{q_{\text{RMS}}}{51.6 \times \sqrt{\frac{\Delta p}{\rho}}} \tag{4.1}$$

This formula calculates the Effective Regurgitant Orifice Area (EROA) by dividing the root mean square of the regurgitant flow rate (q_{RMS}) by the product of the constant 51.6 and the square root of the pressure gradient across the valve during diastole (Δp) divided by the fluid density (ρ).

CO 5 L/Min	**Nodule 3mm**	**Nodule 4mm**	**Unit**
SV	71.10	71.36	mL
CV	-5.88	-5.90	mL
CO	4.98	5.00	L/min
EROA	0.074	0.117	cm^2
LV	-17.60	-26.16	mL
RF	33.04	44.94	%

Table 4.1: Hemodynamic for CO 5 L/Min

As expected, when the nodule size increases, there is a more pronounced leakage volume. The leakage volume is defined as the sum of transvalvular leakage and paravalvular leakage. However, in the absence of a nodule, meaning no stimulation of paravalvular leakage, there are insignificant leakage during diastole (around 1-2 mL/beat), which is also influenced by the oscillation of the flow rate curve during diastole. This indicates that the heart valve is well sealed and functioning effectively. When reporting data, it is more accurate to refer to LV, as it is the one we are specifically evaluating; however, this is almost entirely paravalvular leakage volume. The Regurgitant Fraction (RF) does not always increase with an increase in Cardiac Output. This is observed in the 3mm data, but not in the 4mm data. It is important to note that when the cardiac output increases, both the stroke volume (SV) and the leakage volume increase. More data would be necessary to study this phenomenon comprehensively. The data appear to be consistent and repeatable, indicating that it is feasible to visualize the produced PVL using Particle Image Velocimetry (PIV).

4.1 PVL visualization

The Particle Image Velocimetry (PIV) data were acquired and processed, revealing that the flow under investigation is characterized by a wall jet. This observation was made evident due to the distinctive velocity profiles and flow patterns captured during the diastolic phase. The contact surface within the test chamber was not flat, given its cylindrical shape, which influenced the flow dynamics and the development of the wall jet. This wall jet phenomenon occurs during diastole because of the pressure differential between the aortic side and the ventricular side. The following section provides a representation of the jet at various instants.

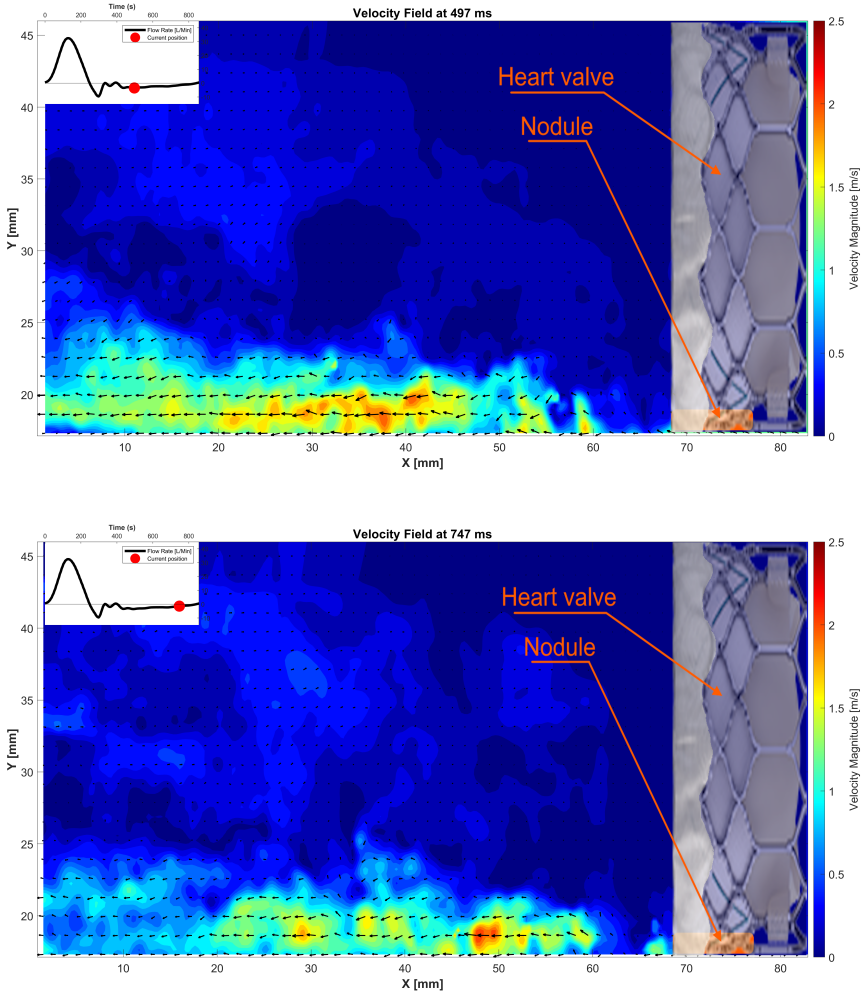

Figure 4.3: Instant velocity field. Cardiac Output 5 L/Min Nodule 3mm

The initial observations from the PIV data indicate that the jet is characterized by a turbulent behavior; however, the mean velocity remains relatively constant throughout diastole. To gain a clearer understanding of these dynamics, the velocity field was averaged over the entire diastolic period. This approach allows for a more comprehensive view of the overall flow patterns and helps identify consistent features within the turbulent jet. By averaging the velocity data over diastole, we can better understand the persistent flow structures and their interactions.

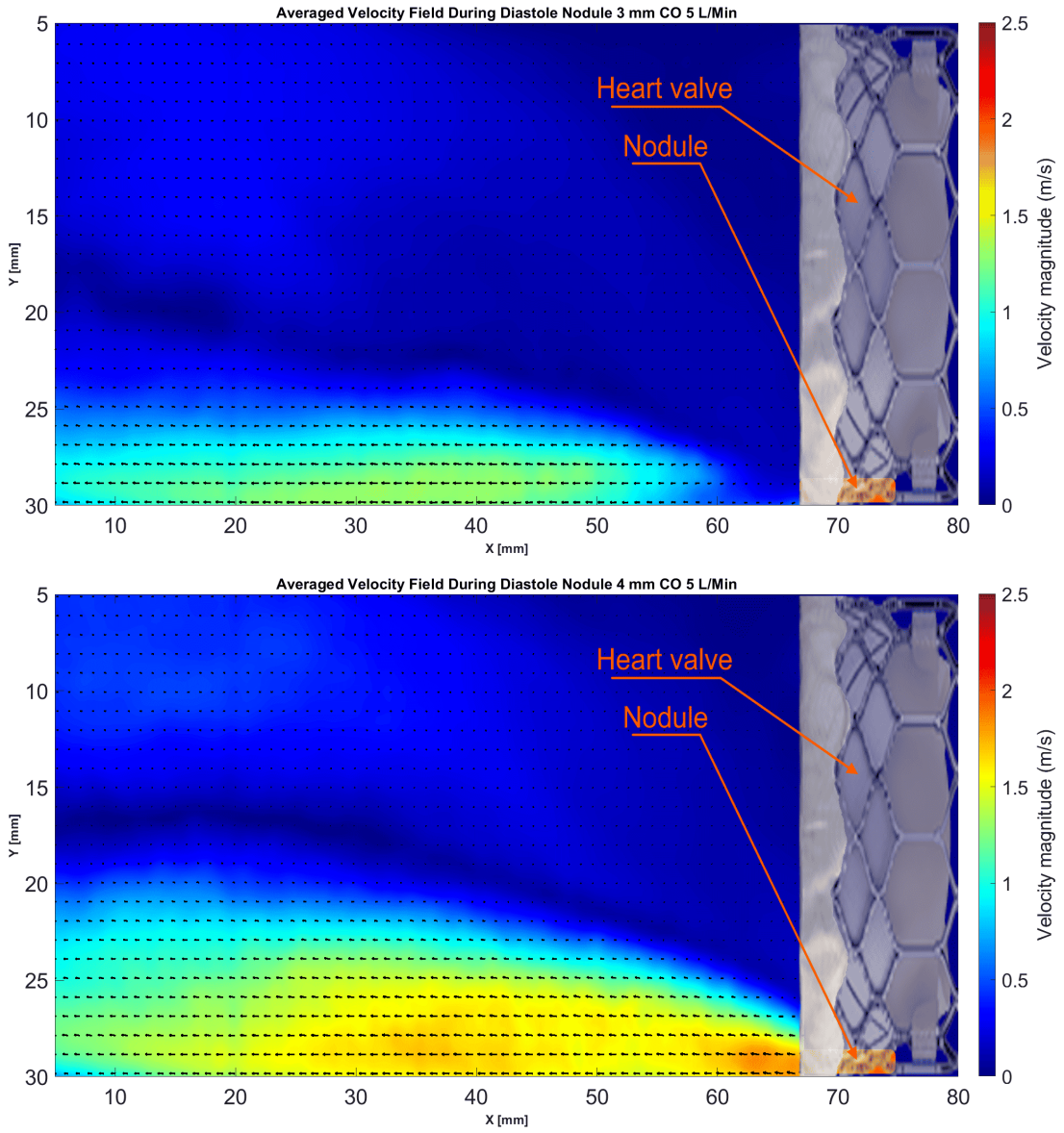

Figure 4.4: Avareged velocity field during diastole Cardiac Output 5 L/Min

The averaged velocity field reveals a much clearer flow pattern, indicating that a significant portion of the jet is turbulent or at least transitioning into turbulence. This highlights the highly dynamic and complex nature of the flow, characterized by large fluctuations in velocity which signify areas of instability. Such turbulence within the jet can influence the efficiency of valve closure, potentially contributing to more aggressive paravalvular leakage (PVL). In the averaged field, the peak velocity is around 2.5 m/s for a 4mm nodule size under a 6.5 L/min cardiac output condition. However, the instantaneous velocity field shows peak velocities reaching up to 3.2 m/s. As the nodule size increases, the thickness of the wall jet also increases, with the width reaching 10 mm for a 3mm nodule size and 15 mm for a 4mm nodule size at x=5 mm. Additionally, the velocity increases with the nodule size. When the cardiac output increases, a more pronounced jet with significantly higher velocity magnitudes can be observed. Average fields are crucial as they provide a clearer representation of the overall flow dynamics and help in identifying persistent flow structures. However, studying turbulence, which can lead to more aggressive PVL, is also essential. Studying these turbulent flows can aid in evaluating potential impacts on the efficiency of valve function and the risk of damage to ventricular tissues and blood particles.

4.2 velocity profiles

It is also interesting to plot the velocity profiles of the wall jet. Unfortunately, due to the limitations of the setup, it is not possible to capture the boundary layer entirely, resulting in a partially visualized wall jet profile. Before analyzing the boundary layer, it is important to visualize the instantaneous velocity profiles at different times and then the averaged profile, as shown in the images 4.5.

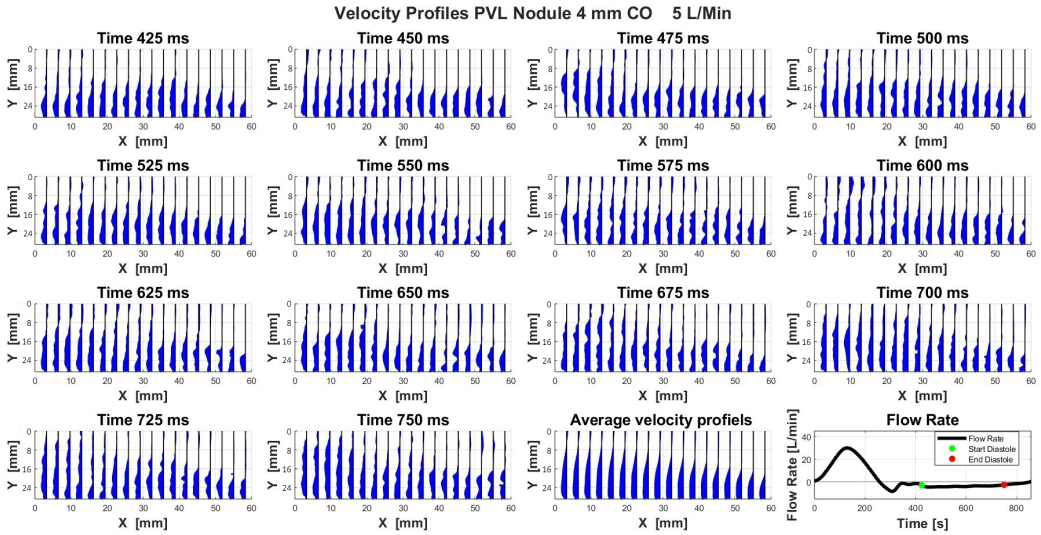

Figure 4.5: Velocity profiles plot

It is clear how turbulence dominates the wall jet, decreasing in intensity as the jet develops. Velocity profiles were plotted for 14 different positions during diastole. The velocity field was averaged between the green point and the red point in Figure 4.5. Some parts of diastole were excluded to avoid transitional effects. Focusing on the averaged profile, we can clearly see the wall jet profile, especially when the jet is fully developed at lower x-coordinates.

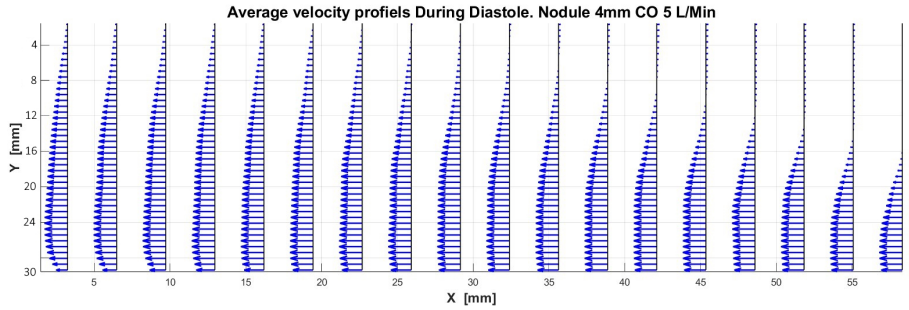

Figure 4.6: Wall Jet velocity profile

The averaged velocity profile plotted during diastole provides clear evidence that we are dealing with a wall jet. The characteristics of a wall jet include a distinct velocity gradient near the wall, indicating the presence of a boundary layer, peak velocity, and an outer zone where the velocity approaches zero. A wall jet typically features a boundary layer, which extends from the wall up to the point where the velocity reaches 99% of the peak velocity. Beyond this boundary layer, the velocity gradually decreases to zero in the outer zone. In Figure 4.6, we can partially observe this boundary layer, especially where the jet is sufficiently developed. The boundary layer's thickness increases with the distance (x) from the jet origin, while the width of the high-velocity region decreases. As the jet develops with increasing x, the peak velocity moves to higher y positions, indicating that the jet is spreading outwards from the wall. This is a characteristic behavior of wall jets, where the high-velocity core initially adheres closely to the wall, but gradually shifts away as the flow progresses downstream. The thickness of the boundary layer increases with x, reflecting the growing influence of viscous diffusion and turbulent mixing as the jet evolves. The plot clearly shows the boundary layer near the wall, where the velocity sharply increases to its peak. This peak velocity then transitions into the outer zone, where the velocity decreases towards zero. The evolution of the jet, with the peak velocity moving to lower y positions and the boundary layer height decreasing with x, demonstrates the dynamic nature of the wall jet as it develops over the diastole period.

4.2.1 Boundary Layer analysis

Boundary layer analysis is necessary to understand how many data in the boundary layer we have and demonstrate that it is a turbulent boundary layer.

Firstly we need to define some quantities. The displacement thickness (δ^*) is defined as the distance by which the external flow is displaced due to the presence of the boundary layer. It represents the loss in mass flow due to the reduced velocity within the boundary layer. The displacement thickness is given by the equation:

$$\delta^* = \int_0^\infty \left(1 - \frac{U}{U_e}\right) dy \tag{4.2}$$

where U is the velocity within the boundary layer and U_e is the peak velocity of the wall jet. The momentum thickness (θ) is a measure of the loss in momentum due to the presence of the boundary layer. It represents the reduction in momentum flux and is given by the equation:

$$\theta = \int_0^\infty \frac{U}{U_e}\left(1 - \frac{U}{U_e}\right) dy \tag{4.3}$$

where U is the velocity within the boundary layer and U_e is the peak velocity of the wall jet. The shape factor (H) is the ratio of the displacement thickness to the momentum thickness:

$$H = \frac{\delta^*}{\theta} \tag{4.4}$$

The shape factor provides insight into the nature of the boundary layer. For a turbulent boundary layer, the shape factor typically ranges from 1.3 to 1.4. This range indicates a well-developed turbulent boundary layer. In our analysis, we do not have complete data for the entire boundary layer. However, as we analyze profiles corresponding to zones where the jet is more developed, we gather more data on the boundary layer. By focusing on these regions, we find that the shape factor values approach the reference range of 1.3 to 1.4, indicating a turbulent boundary layer. This could be because we have more boundary layer data in these regions, making the results more accurate. Additionally, it is possible that the jet becomes completely turbulent further from the orifice.

Nodule 4mm CO 5 L/Min					
X [mm]	60	45	30	15	5
H	1.12	1.15	1.18	1.24	1.42

Table 4.2: The table illustrates the evolution of the shape factor in different x positions for the 4mm Nodule 5 L/min Cardiac Output condition.

4.2.2 Turbulent Boundary Layer

A turbulent boundary layer is divided into two main regions: the outer layer and the inner layer. The inner layer is further subdivided into the viscous sublayer, the buffer layer, and the logarithmic layer. The inner layer extends from the wall up to $y^+ \approx 500 - 1000$ and typically comprises 10-20% of the boundary layer thickness (δ). Within the inner layer, the flow can be further categorized:

- **Viscous Sublayer**

  ($y^+ < 5$): In this region, viscous effects dominate, and the flow is nearly laminar. The velocity profile is linear and can be described by the equation:

  $$u^+ = y^+ \tag{4.5}$$

- **Buffer Layer**

  ($5 < y^+ < 30$): This is a transition zone where both viscous and turbulent effects are significant. The flow in the buffer layer is influenced by the interaction between the near-wall turbulence and the viscous forces.

- **Logarithmic Layer**

  ($30 < y^+ < 500-1000$): In this region, the velocity profile follows a logarithmic distribution:

  $$u^+ = \frac{1}{\kappa} \ln y^+ + C$$

  where κ is the von Kármán constant (approximately 0.41) and C is Coles's constant. The extent of the logarithmic layer depends on the Reynolds number, with higher Reynolds numbers extending the logarithmic region further from the wall.

The thickness of the inner layer varies with the Reynolds number. As the Reynolds number increases, the inner layer becomes thinner relative to the overall boundary layer.

4.2.3 Wall shear stress discussion

When dealing with a turbulent boundary layer, it is crucial to evaluate Wall Shear Stress (WSS) accurately. There are two primary methods for calculating WSS: Newton's Method and the Clauser Method. Below is a detailed explanation of each method, including the working principles, equations, and hypotheses.

- **Newton method**

  Newton's Method for evaluating WSS is based on the fundamental principle of shear stress due to viscosity in a fluid. It calculates WSS directly from the velocity gradient at the wall. The equation for Newton's Method is given by:

$$\tau_w = \mu \left. \frac{dU}{dy} \right|_{y=0} \tag{4.6}$$

  where τ_w is the wall shear stress, μ is the dynamic viscosity of the fluid, U is the velocity of the fluid parallel to the wall, and $\frac{dU}{dy}$ is the velocity gradient perpendicular to the wall, evaluated at the wall ($y = 0$).

  The working principle of Newton's Method involves determining the velocity gradient $\frac{dU}{dy}$ by measuring the velocity profile near the wall. In turbulent flow, this requires high-resolution data close to the wall, as the gradient can be steep. The dynamic viscosity μ is a property of the fluid and is typically known.

  Newton's Method offers several advantages, including direct calculation from measured velocity profiles and applicability to both laminar and turbulent flows, provided the velocity gradient near the wall is accurately known. However, it also has limitations. This method requires accurate velocity measurements very close to the wall.

- **Clauser Method**

  The Clauser Method is a widely used technique to estimate Wall Shear Stress (WSS) in turbulent boundary layers by utilizing the logarithmic velocity profile characteristic of such flows. This method involves plotting the friction coefficient factor (C_f) to determine the appropriate WSS.

  The logarithmic law describes the velocity profile close to the wall in a turbulent boundary layer and is given by the equation:

$$\frac{u}{u_\tau} = \frac{1}{\kappa} \ln \left(\frac{y u_\tau}{\nu} \right) + C \tag{4.7}$$

where $\frac{u}{u_\tau}$ is the dimensionless velocity, u_τ is the friction velocity, κ is the von Kármán constant (typically $\kappa \approx 0.41$), y is the distance from the wall, ν is the kinematic viscosity, and C is Coles's constant (typically $C \approx 5.0$).

To apply the Clauser Method, this logarithmic law is transformed to the form used for the Clauser plot. The friction velocity u_τ is related to the external flow velocity U_e through the friction coefficient C_f:

$$u_\tau = U_e\sqrt{\frac{C_f}{2}} \tag{4.8}$$

Substituting this into the logarithmic law and rearranging, we get:

$$\frac{u}{U_e} = \sqrt{\frac{C_f}{2}}\left[\frac{1}{\kappa}\ln\left(\frac{yU_e}{\nu}\sqrt{\frac{C_f}{2}}\right) + C\right] \tag{4.9}$$

This form allows us to plot the dimensionless velocity $\frac{u}{U_e}$ against the dimensionless distance $\frac{yU_e}{\nu}$ on a logarithmic scale.

The Clauser plot is a graphical tool used to determine the friction coefficient factor (C_f). Different lines corresponding to various values of C_f are plotted, representing theoretical velocity profiles according to the logarithmic law for different C_f values. The experimental data points are overlaid onto the Clauser plot. If the data points align with one of the C_f lines, it indicates the correct C_f value.

When the experimental data points align along a line, it confirms the presence of the logarithmic region in the boundary layer and identifies the corresponding C_f value. Once the C_f value is identified, the friction velocity u_τ and wall shear stress τ_w can be calculated using the following equations:

$$u_\tau = U_e\sqrt{\frac{C_f}{2}} \tag{4.10}$$

$$\tau_w = \rho u_\tau^2 = \rho U_e^2\frac{C_f}{2} \tag{4.11}$$

In our case, we did not have data close enough to the wall to be within the viscous sublayer ($y^+ < 5$), making it impossible to evaluate the wall shear stress using Newton's method. Consequently, we attempted to use the Clauser method. Below is a plot for $x = 5$ mm, with a cardiac output of 5 L/min and a nodule size of 4 mm.

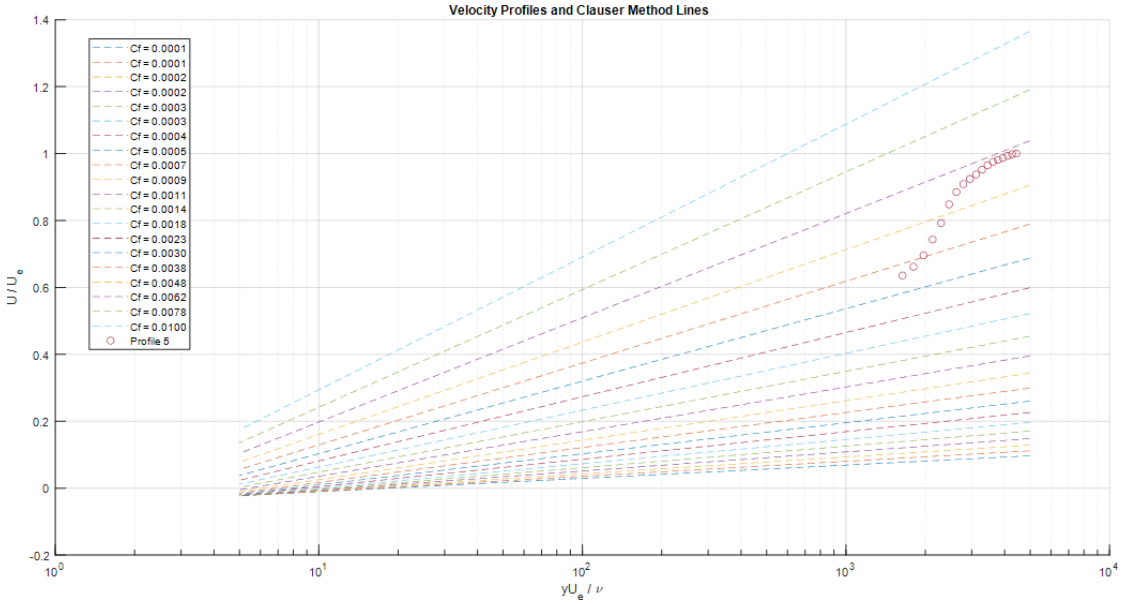

Figure 4.7: Clauser method for Cardiac Output 5 L/Min, nodule 4mm, x=5mm

As can be seen, the data do not align with any parameterization of C_f, indicating that the analyzed data do not exhibit a logarithmic velocity profile. There are several possible reasons for this discrepancy. Firstly, we do not know if the boundary layer is fully developed or in the process of transitioning to turbulence, which makes it difficult to determine when the transition occurs. Additionally, it is possible that the closest data points we have to the wall are already outside the inner layer. However, it is clear that we cannot evaluate the wall shear stress using the Clauser method either.

4.3 Kinetic turbolent energy

Turbulent Kinetic Energy (TKE) is a critical parameter in understanding the dynamics of turbulent flows. It quantifies the energy contained within turbulent eddies, providing insights into the intensity of turbulence and its potential impacts. The equation used to evaluate TKE is:

$$\text{TKE} = \frac{1}{2}\rho\left(\overline{u'^2} + \overline{v'^2}\right) \tag{4.12}$$

where $\overline{u'^2}$ and $\overline{v'^2}$ are the mean square fluctuations of the velocity components in the x and y directions, respectively. In figure 4.7, TKE was evaluated averaging the TKE for every instant during diastole. Analyzing TKE is crucial because it highlights regions with high turbulence, which can correlate with areas of increased shear stress and potential tissue and particles damage. High TKE values indicate vigorous mixing and energy dissipation, which are significant for understanding the analyzed environment. As we can see from the figure 4.7, where the CO 5 L/Min scenario is visualized, the TKE reaches the highest values in the center between x=40 and x=60. We also observe high values just at the exit of the orifice, close to the valve. The peak value for TKE is around 350 joules, which is particularly evident in the case with a 4mm nodule size and a cardiac output of 6.5 L/min. However, the shown results are about average TKE during diastole. As known, it is also important to evaluate TKE instantaneously. In this case, data show how it is possible to reach values over 400 J for brief instants. This means that these high TKE values are not consistent over time.

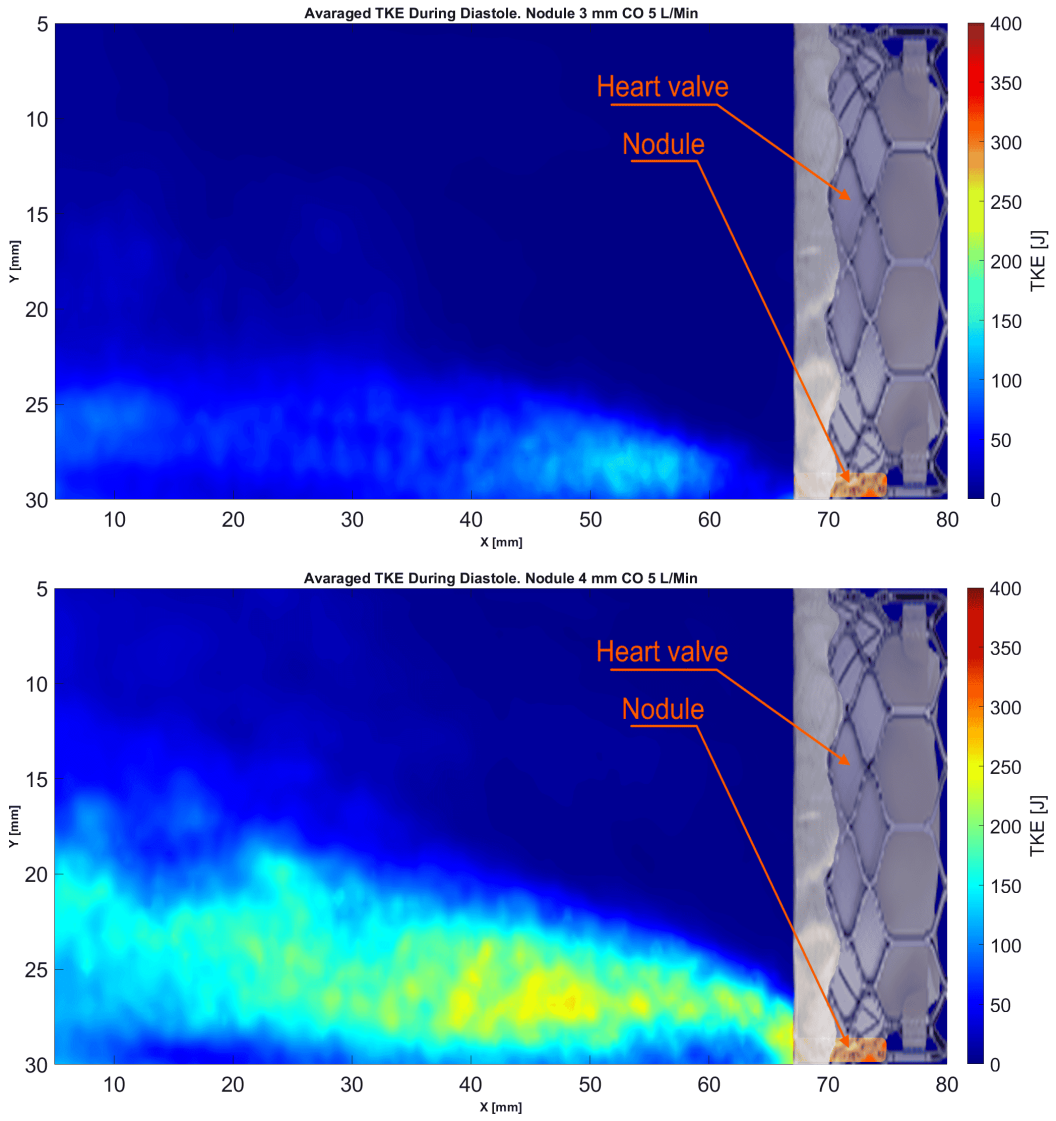

Figure 4.8: Averaged TKE field during diastole Cardiac Output 5 L/Min

4.4 Shear Stress Analysis

Shear stress in fluid dynamics refers to the force per unit area exerted by the fluid parallel to the flow direction. This parameter is critical for understanding the interactions between fluid flow and surfaces, and it plays a significant role in various biological applications. There are two main types of shear stress in fluid dynamics: Viscous Shear Stress (VSS) and Reynolds Shear Stress (RSS). Viscous Shear Stress arises from the fluid's viscosity and the velocity gradient near the wall, and it is essential for characterizing laminar flow behavior. On the other hand, Reynolds Shear Stress is associated with the turbulent components of the flow, representing the fluctuating shear stresses that arise due to turbulence. Both types of shear stress are pivotal in comprehending the complete picture of fluid behavior, particularly in complex flow environments.

4.4.1 Viscous Shear Stress (VSS)

Viscous Shear Stress (VSS) iis evaluated with the equation:

$$\text{VSS} = \tau_{xy} = \mu \left(\frac{dU}{dy} + \frac{dV}{dx} \right) \tag{4.13}$$

where τ_{xy} is the shear stress, μ is the dynamic viscosity of the fluid, and U and V are the velocity components in the x and y directions, respectively. VSS arises due to the viscosity of the fluid and the velocity.

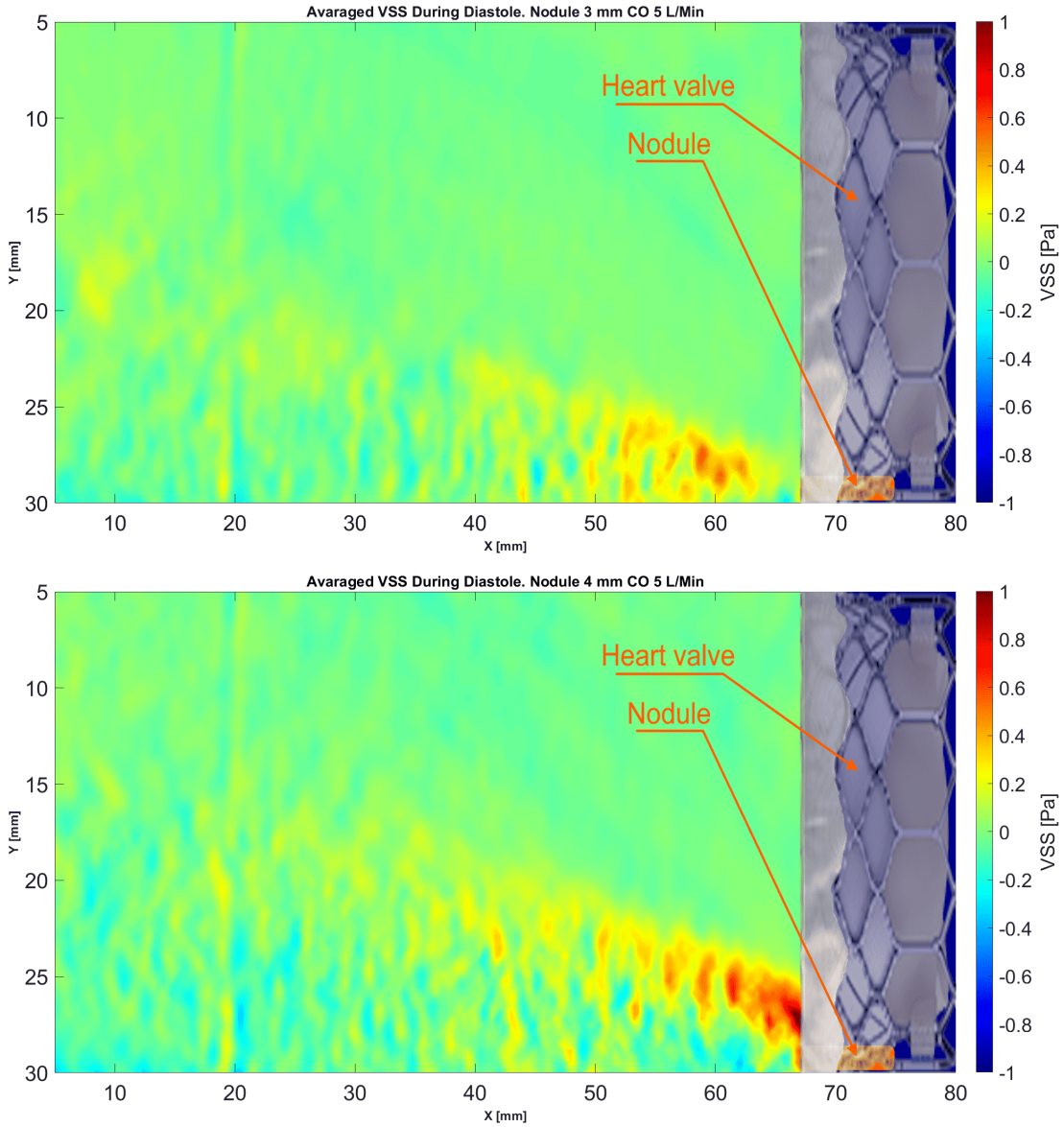

Figure 4.9: Avareged VSS field during diastole

4.4.2 Reynolds Shear Stress (RSS)

Reynolds Shear Stress (RSS) is evaluated with the equation:

$$\mathrm{RSS} = \rho\sqrt{\left(\frac{\overline{u'u'} - \overline{v'v'}}{2}\right) + \overline{u'v'}^2} \tag{4.14}$$

where ρ is the fluid density, and u' and v' are the velocity fluctuations in the x and y directions, respectively. RSS represents the turbulent component of shear stress and is significant in flows with high turbulence.

Shear stress has a profound impact on blood components such as red blood cells, white blood cells, and platelets. High shear stress can lead to the deformation or even destruction of these cells, which can impair their function and contribute to various cardiovascular diseases. For instance, elevated shear stress can cause hemolysis, where red blood cells are damaged and release their contents into the bloodstream. This can also affect the aggregation and activation of platelets, which are crucial for blood clotting. Analyzing wall shear stress is particularly important for understanding the potential damage to ventricular tissue. High wall shear stress can lead to endothelial cell damage, promoting inflammation and contributing to the development of atherosclerosis or other cardiovascular conditions.

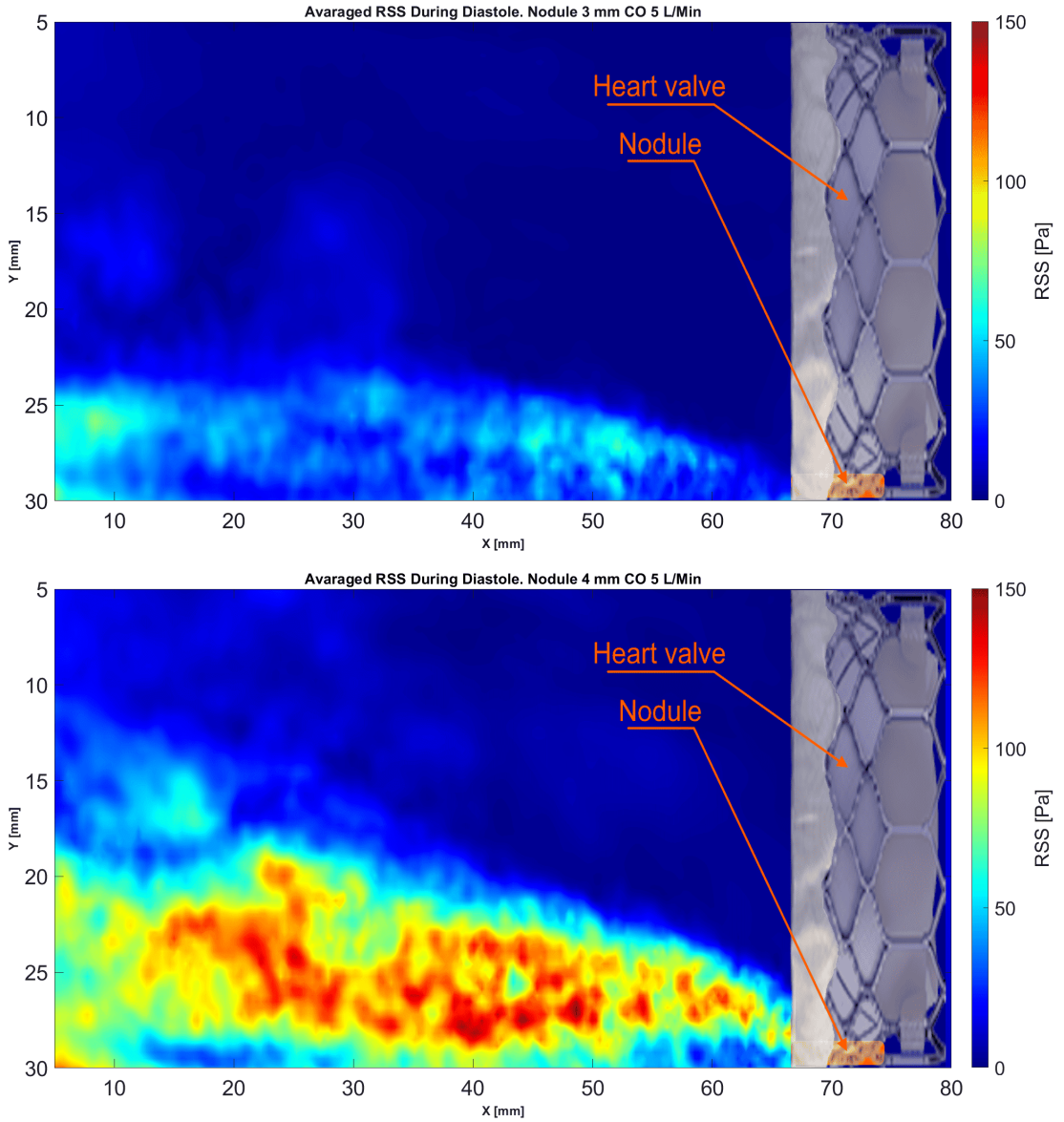

Figure 4.10: Avareged RSS field during diastole

The results for Reynolds Shear Stress (RSS) show a significant peak in the center of the jet, where turbulence is highest. In the condition with a 4mm nodule size and a cardiac output of 6.5 L/min, the RSS reaches values around 160 joules. This peak indicates a region of intense turbulent shear stress, which is typically found where the flow is most chaotic and energy dissipation is highest.
The results for Viscous Shear Stress (VSS) show a significant peak just after the orifice. In the condition with a 4mm nodule size and a cardiac output of 6.5 L/min,

the VSS reaches values up to 1.5 Pa. This peak indicates a region of high shear stress immediately downstream of the valve, where the flow velocity gradient is steep due to the sudden expansion and mixing of the jet. Howevwr VSS is two order of magnitude smaller than RSS.

4.4.3 Particle tracking

Particle tracking is a technique used to monitor the movement of particles within a fluid flow, providing insights into how these particles evolve over time. This method involves tracking the position and trajectory of particles, allowing us to analyze their behavior and interaction with the surrounding flow. By visualizing and quantifying the paths taken by these particles, we can gain a better understanding of the flow patterns, detect areas of re-circulation, and identify regions where particles may accumulate. For our application, particle tracking is particularly important as it helps identify potential stagnation zones within the flow. Stagnation zones are areas where particles experience difficulty moving out, which can lead to problems such as blood coagulation. In cardiovascular systems, blood stagnation can increase the risk of clot formation, posing serious health threats. In our study, particle tracking was implemented by positioning 1000 particles at x=60. This position was chosen to avoid the high instability of the flow near the heart valve but not so far from it where the jet is already developed.

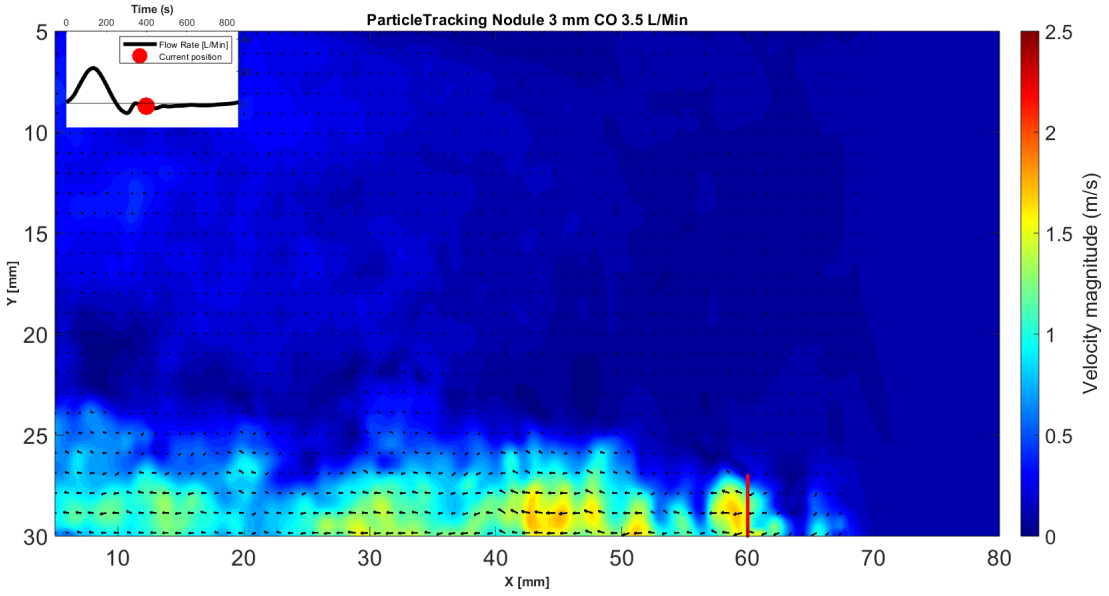

Figure 4.11: Particles positions in particle tracking analysis

The analysis was conducted over a couple of cycles, up to 2000 ms. For each condition, we examined the time required for all particles to exit the field of view, either by touching a wall or the heart valve.
The results clearly indicate that there are no significant stagnation zones present. The most challenging configuration was observed with a 3mm nodule and a cardiac output of 3.5 L/min, where approximately 1100 ms were needed for all particles to leave the field of view. This finding suggests that, while there are areas with slower

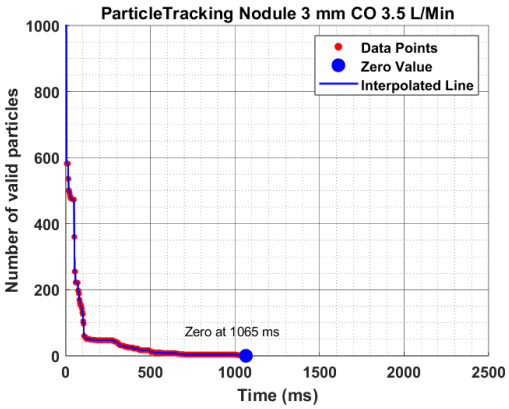

Figure 4.12: Nodule 3mm CO 5 L/Min

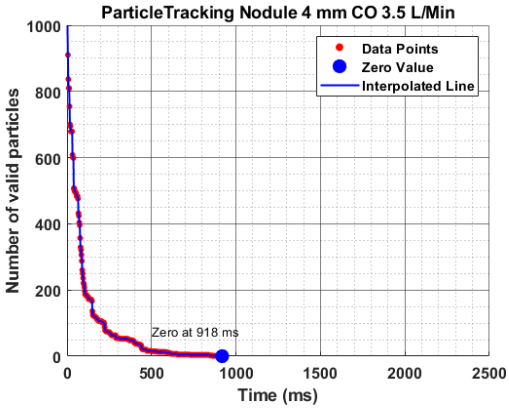

Figure 4.13: Nodule 4mm CO 5 L/Min

particle movement, the particles eventually move out of these regions, reducing the likelihood of prolonged stagnation and potential blood coagulation.

4.5 Plenoptic PIV results

The 3D Particle Image Velocimetry (PIV) results were obtained using a plenoptic camera, offering a detailed view of the fluid dynamics within the studied system. This approach utilized phase-averaged PIV with 10 phases during diastole, allowing for a detailed analysis of the flow patterns at different points in the diastole The 3D PIV results confirmed the findings from the 2D PIV analysis, reinforcing the observed flow behaviors and providing additional insights into the spatial dynamics of the flow. The ability to visualize the flow in three dimensions is particularly valuable in identifying intricate flow structures and interactions that may not be fully captured in 2D analyses alone. The flow during diastole appears relatively constant, so except for the transitional phases (Phase A and J), the velocity field is similar within the phases.

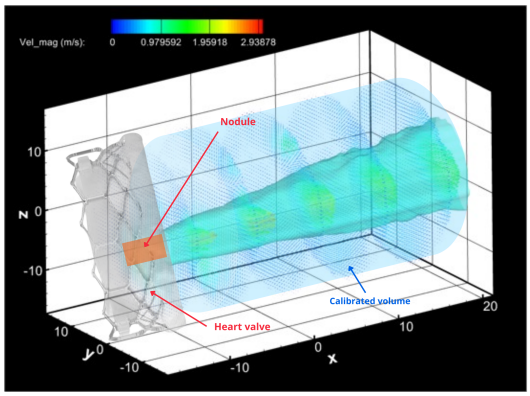

Figure 4.14: Nodule 3mm CO 5 L/Min

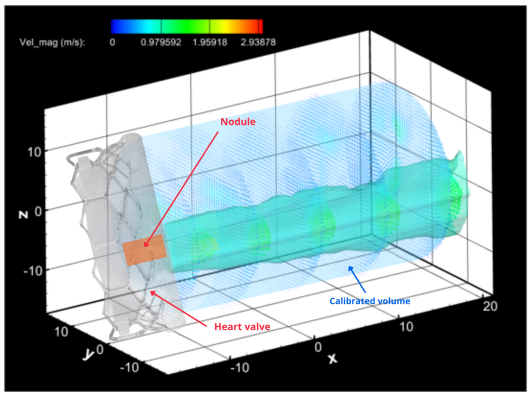

Figure 4.15: Nodule 4mm CO 5 L/Min

Naturally, close to the orifice, the volume occupied by the jet appears larger in the 4mm nodule condition. However, despite the larger percentage of volume occupied by the 4mm condition, the jet in the 3mm condition increases in width more rapidly. It is also interesting to observe the different shapes of the jet between the two different nodule conditions.

4.5.1 Volume Occupied by the Jet

A table will be presented to show the percentage of the volume in which the jet is present over the calibration volume for each different condition. This table provides a clear comparison of how the jet occupies the space within the calibration volume under various conditions.

Nodule (mm)	Cardiac Output (L/min)	Jet Volume (%)
3mm	3.5	32.18
4mm	3.5	45.98
3mm	5.0	35.54
4mm	5.0	47.99
3mm	6.5	36.02
4mm	6.5	51.35

Table 4.3: Percentage of Volume Occupied by the Jet for Different Conditions

We can observe how the jet occupies a significant portion of the studied volume in all conditions. The volume occupied by the jet varies slightly with changes in cardiac output but increases drastically when the nodule size increases. In the 4mm nodule condition with a cardiac output of 6.5 L/min, the jet occupies more than 50% of the volume studied.

4.5.2 Jet Thickness Analysis

We also analyzed the thickness of the jet in both the x-z and x-y planes. This analysis focuses on how the thickness of the jet varies along the y and z directions as the x-coordinate increases. Understanding the variation in jet thickness along these planes is crucial for understanding the spatial distribution and development of the jet within the fluid system.

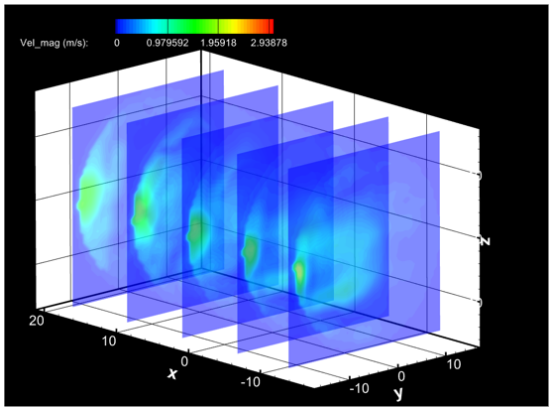

Figure 4.16: Nodule 3mm CO 5 L/Min in diferent y positions

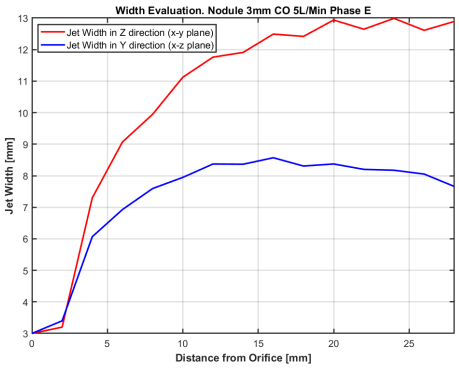

Figure 4.17: Jet Width evaluation

The thickness of the jet increases along the y and z directions as the x-coordinate increases. This indicates the spreading nature of the jet as it moves away from the orifice. The analysis of jet thickness in both planes helps in understanding the dynamics and expansion of the jet in three dimensions. The jet width along the z-axis is larger than the jet width along the y-axis, likely because there is no wall to obstruct the spreading of the jet along the z-axis. We can reach a maximum width of the jet along the y-axis of around 8 mm, while along the z-axis, this can extend up to 13 mm.

Chapter 5

Discussion and Conclusion

The results of the experiments indicate that a wall jet forms during diastole, flowing back from the aortic side into the ventricular side. Despite the peak velocity being around 3 m/s, which is not extremely high, the potential implications of this flow behavior should not be underestimated. The particle tracking analysis highlighted that paravalvular leakage (PVL) do not create stagnation zones. Even in the worst-case scenario, with a 3mm nodule size and a cardiac output of 3.5 L/min, all particles exited the jet in less than two cycles. During systole, it is evident that all particles move towards the aortic side, demonstrating the dynamic nature of the flow and the absence of prolonged stagnation. However, the turbulence within the wall jet can pose significant issues for blood particles. High levels of turbulence lead to substantial Reynolds shear stress values, which can impact red blood cells, white blood cells, and platelets. In our experiments, we observed peak shear stress (SS) levels reaching up to 220 Pa under the worst conditions. However, on average, the peak shear stress in the most adverse scenarios was around 160-170 Pa. Considering these stress levels, it is essential to understand the implications of such mechanical forces on various blood components, such as red blood cells (RBCs), platelets, and white blood cells (WBCs). The exposure time in our experiments was approximately 0.5 seconds, repeated every 0.3 seconds. Red blood cells are particularly susceptible to mechanical damage induced by shear stress. Studies indicate that hemolysis can occur at shear stress levels as low as 150-300 Pa [23]. In the experimental results, the average peak shear stress of 160-170 Pa falls within this critical range. The repetitive nature of the exposure exacerbates this risk, as even intermittent bursts of high shear stress can accumulate to cause significant RBC damage.
The primary effects on RBCs include:

- **Hemolysis**: The destruction of RBCs, leading to the release of hemoglobin into the plasma. This can result in decreased oxygen-carrying capacity and

other complications.

- **Impaired Deformability**: Repetitive shear stress can reduce the deformability of RBCs, making it difficult for them to navigate through microcirculatory pathways. This impairment can contribute to microvascular occlusions and tissue ischemia.

Platelets can be activated by shear stress, and this activation can lead to aggregation and thrombus formation. Studies have shown that shear stress levels around 100-150 Pa can initiate platelet activation, while stress levels above 300-500 Pa significantly enhance this activation [24]. In our experiments, the observed shear stress levels are sufficient to activate platelets, posing a risk of thromboembolic events, especially with repetitive exposure. Specific effects on platelets include:

- **Activation and Aggregation**: Shear stress can activate platelets, prompting them to aggregate. This process is critical in hemostasis but, under pathological conditions, can lead to thrombosis.
- **Release of Procoagulant Microparticles**: Activated platelets release microparticles that enhance coagulation, contributing to a prothrombotic state.

While WBCs are generally more resilient to shear stress compared to RBCs and platelets, they are not immune to damage. Prolonged or repetitive exposure to high shear stress can affect WBC function and viability.
The primary effects on WBCs include:

- **Mechanical Damage**: High shear stress can cause physical damage to WBCs, affecting their ability to function effectively in immune responses.
- **Activation and Inflammation**: Shear stress can activate WBCs, potentially leading to an inflammatory response. This can exacerbate existing conditions and contribute to vascular inflammation.

We should consider that, as the 3D results show, a significant portion of the ventricular volume is impacted by this jet. Data indicate that in the worst condition, with a 4mm nodule and a cardiac output of 6.5 L/min, more than 50% of the volume is affected by the jet. Of course, not all the volume is impacted with the same intensity, as there is a velocity distribution within the jet. This means that different regions of the affected volume experience varying levels of velocity, influencing the degree of shear stress and turbulence encountered by blood components. Further investigation would be interesting, such as evaluating the wall shear stress to determine if the ventricular tissue could be damaged by the PVL jet. Additionally,

analyzing how the jet evolves in a test chamber that better emulates the shape of the heart would be beneficial. This study provides a valuable foundation for further studies and investigations.

Appendix A

Drawings

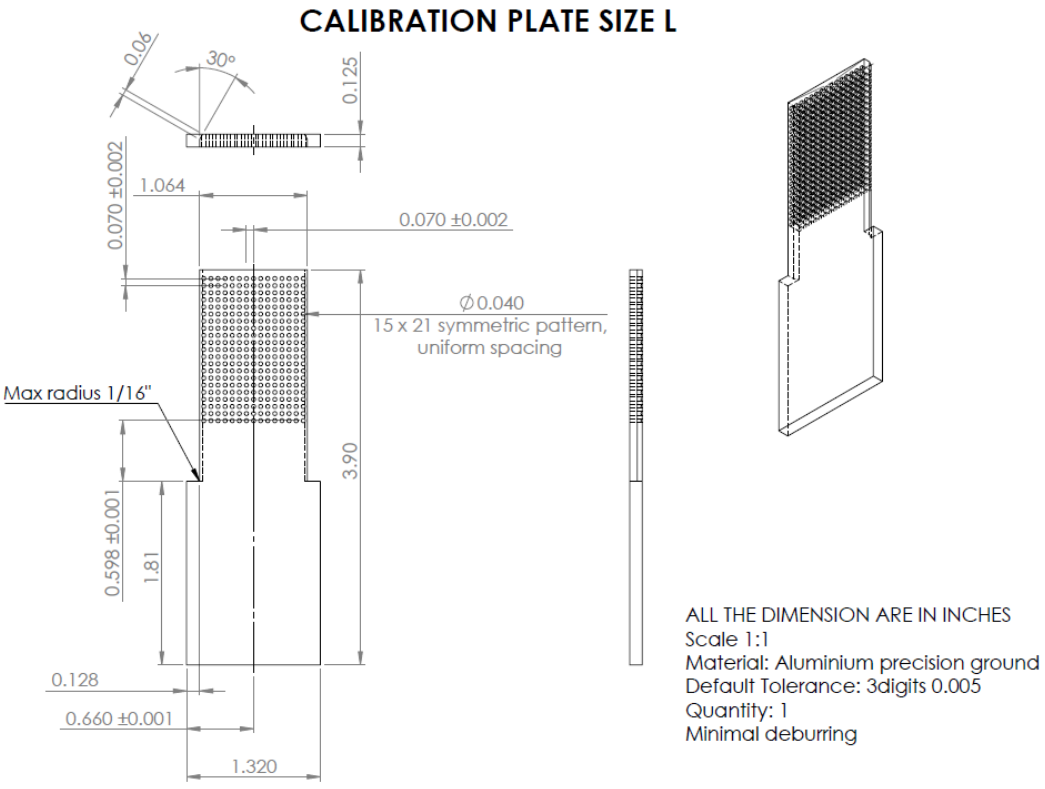

Figure A.1: Calibration Plate Size L

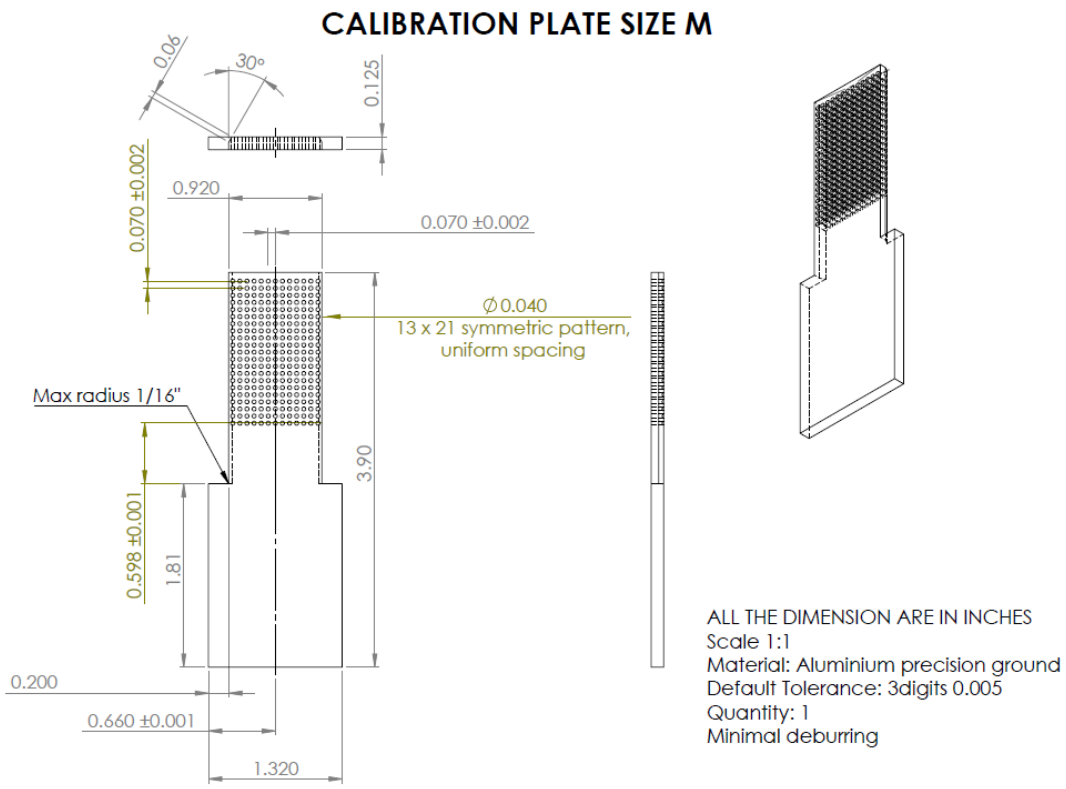

Figure A.2: Calibration Plate Size M

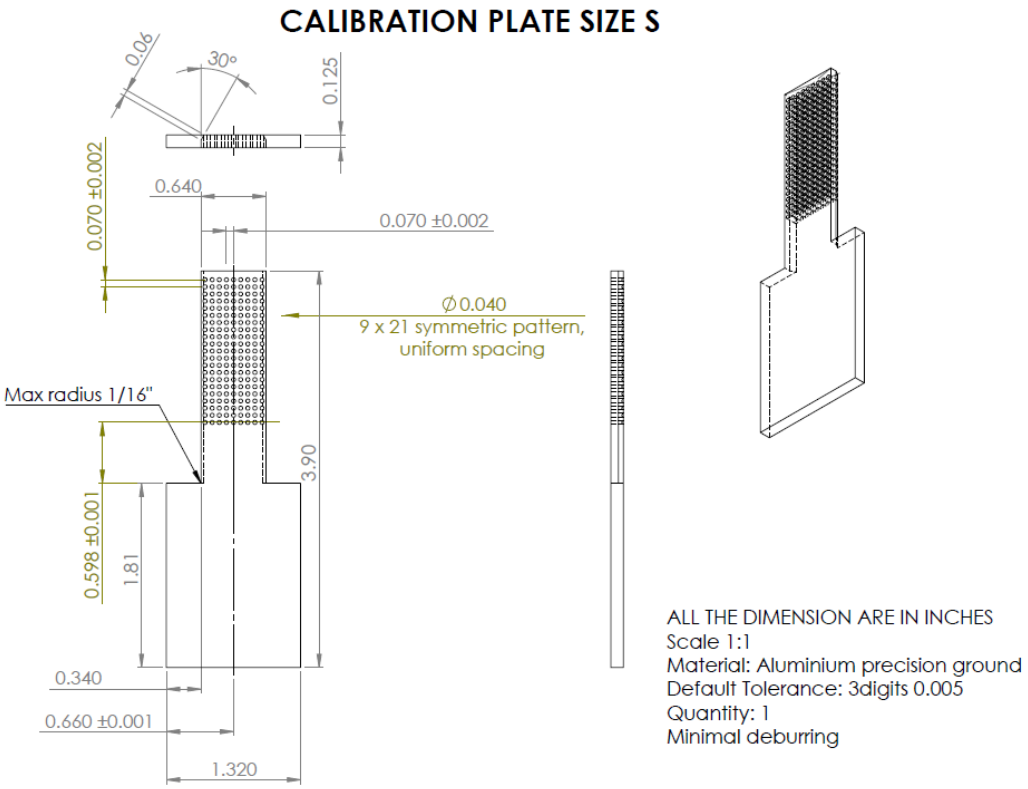

Figure A.3: Calibration Plate Size S

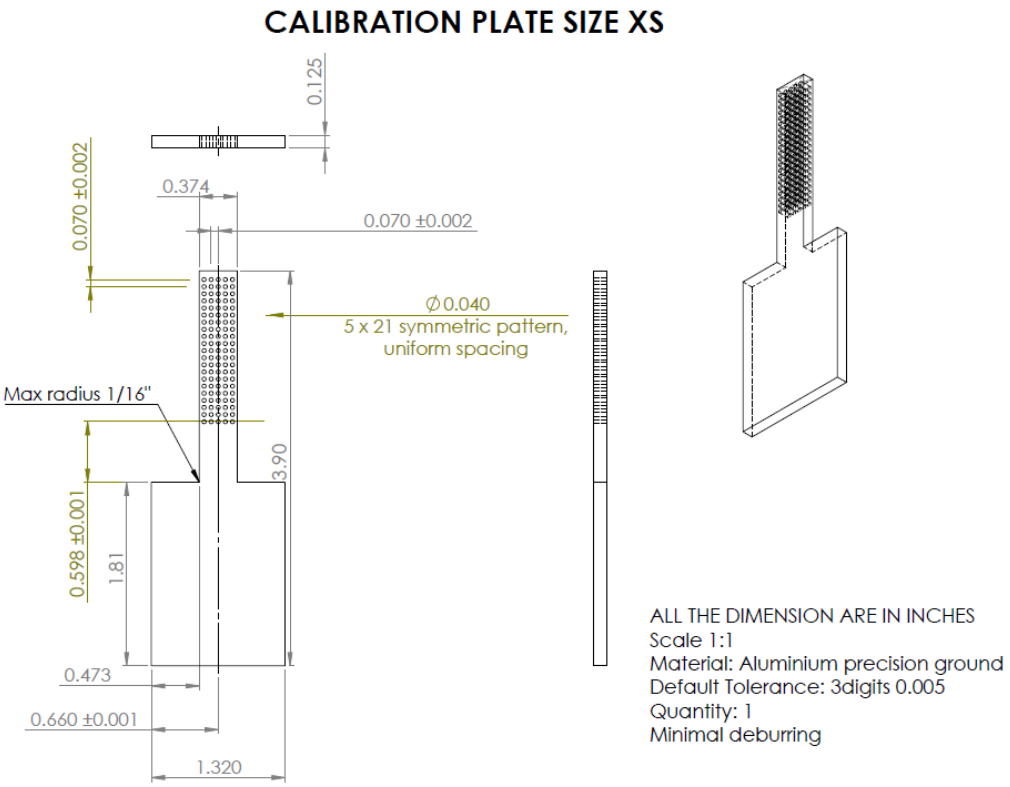

Figure A.4: Calibration Plate Size XS

CALIBRATION SUPPORT PART 1

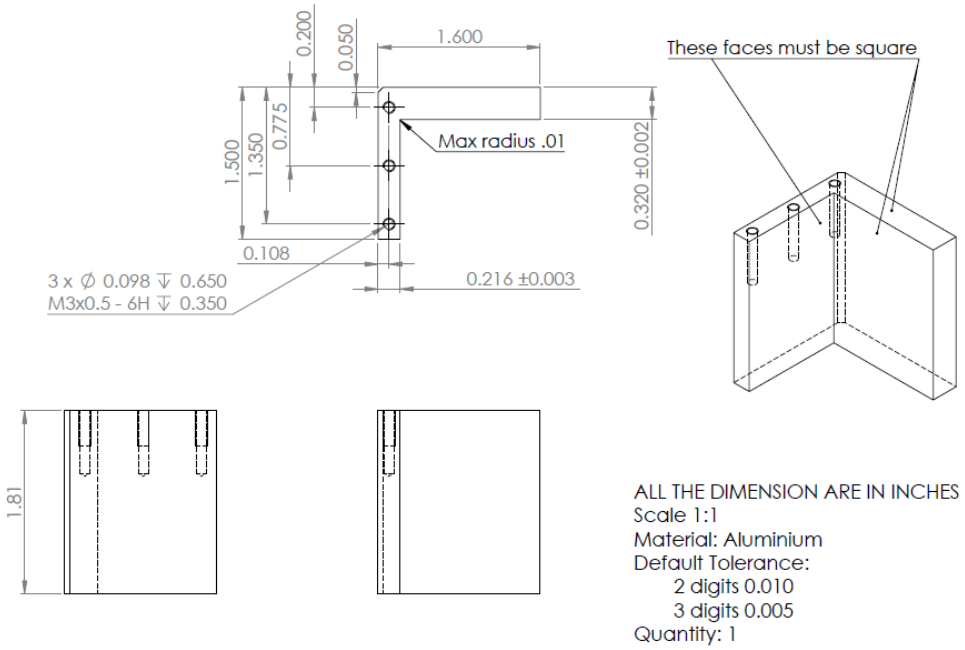

CALIBRATION SUPPORT PART 2

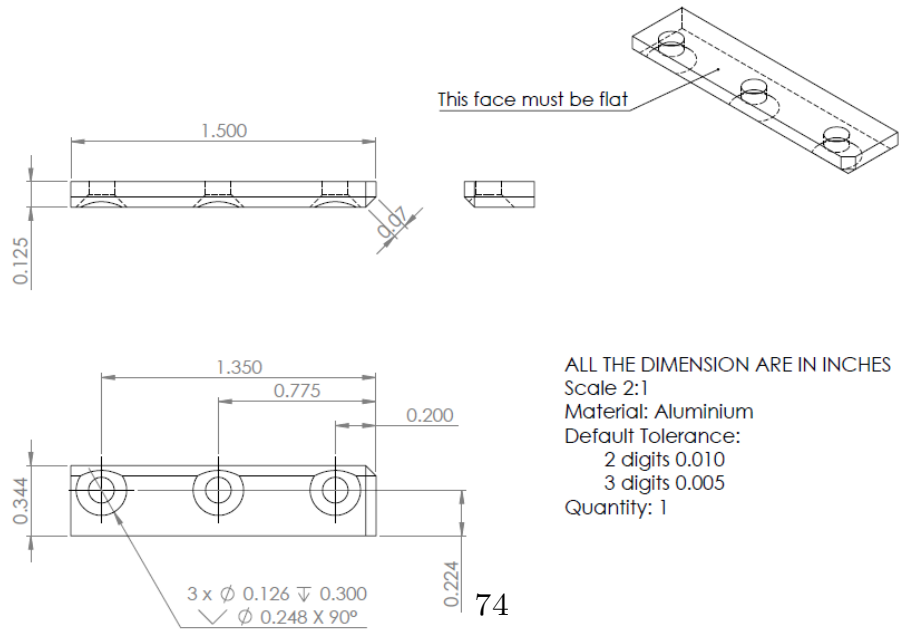

Figure A.5: Calibration support

Appendix B

Results

B.1 Hemodynamic

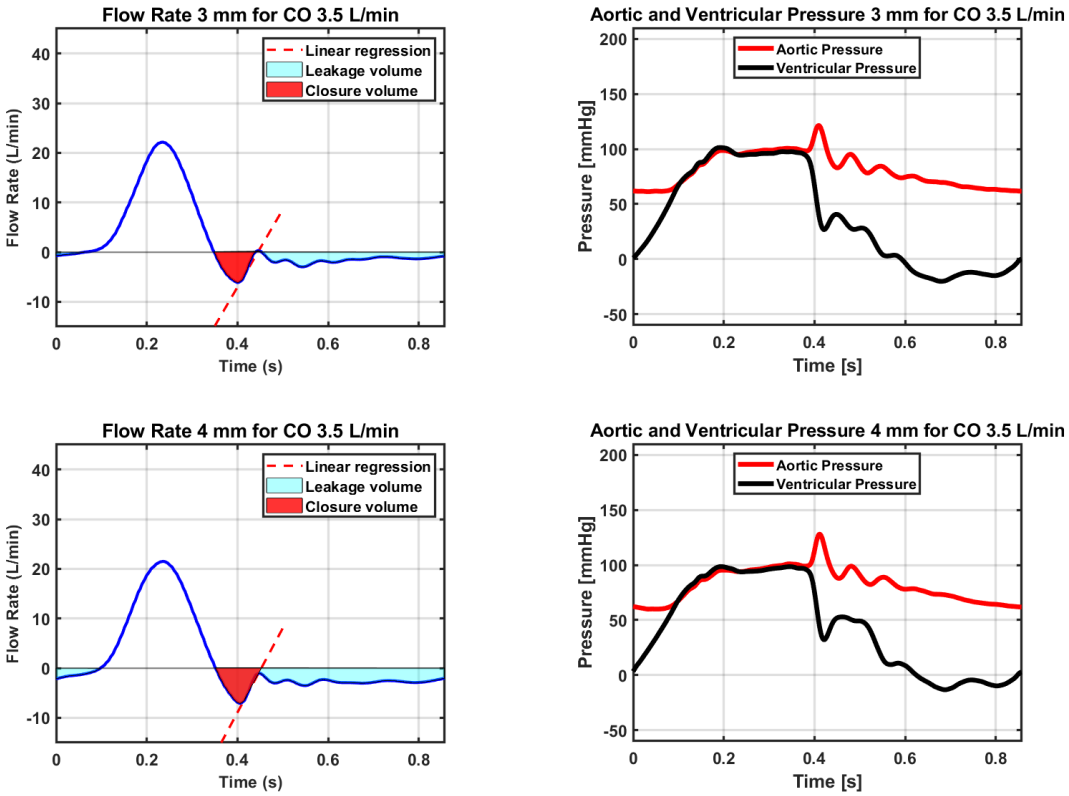

Figure B.1: Hemodynamic Flow rate 3.5 L/Min

CO 3.5 L/Min	Nodule 3mm	Nodule 4mm	Unit
SV	49.99	50.42	mL
CV	-5.56	-6.097	mL
CO	3.49	3.52	L/min
EROA	0.064	0.11	cm^2
LV	-5.23	-21.15	mL
RF	21.59	54.05	%

Table B.1: Cardiac Output 3.5 L/Min

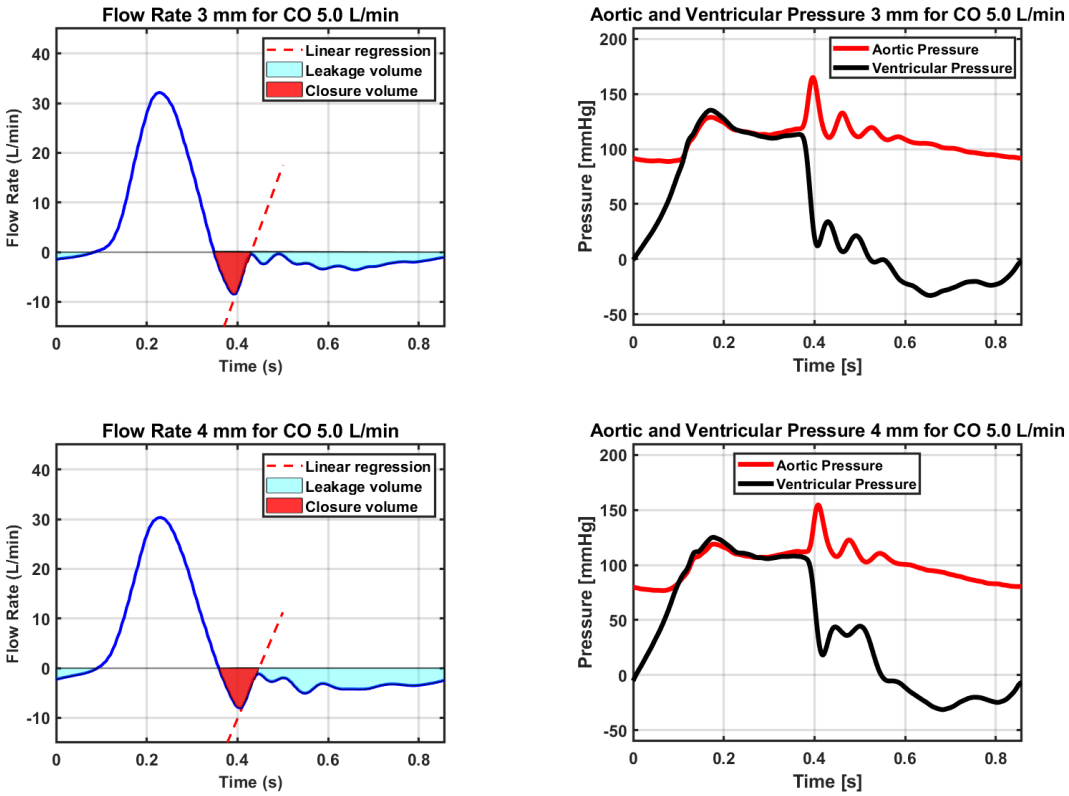

Figure B.2: Hemodynamic Flow rate 5 L/Min

CO 5 L/Min	Nodule 3mm	Nodule 4mm	Unit
SV	71.10	71.36	mL
CV	-5.88	-5.90	mL
CO	4.98	5.00	L/min
EROA	0.074	0.117	cm^2
LV	-17.60	-26.16	mL
RF	33.04	44.94	%

Table B.2: Table for CO 5 L/Min

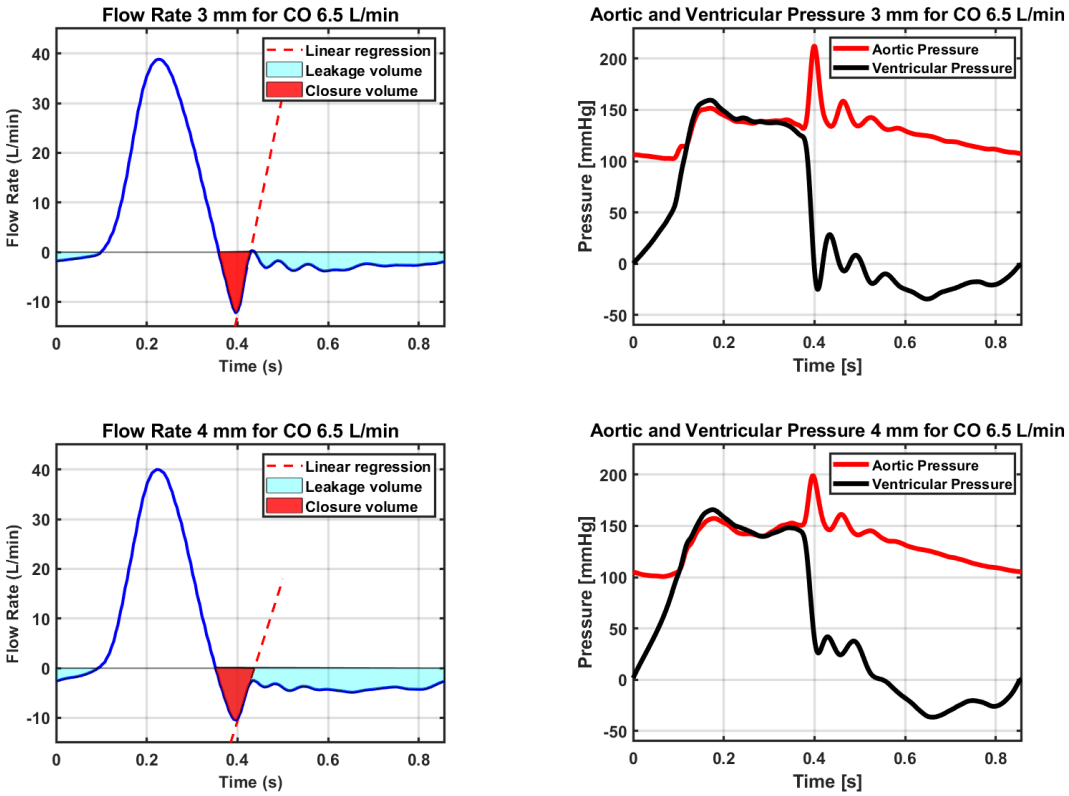

Figure B.3: Hemodynamic Flow rate 6.5 L/Min

CO 6.5 L/Min	Nodule 3mm	Nodule 4mm	Unit
SV	92.36	91.82	mL
CV	-6.993	-7.45	mL
CO	6.47	6.45	L/min
EROA	0.08	0.119	cm^2
LV	-25.771	-31.83	mL
RF	34.39	42.77	%

Table B.3: Table for CO 6.5 L/Min

B.2 Averaged velocity field

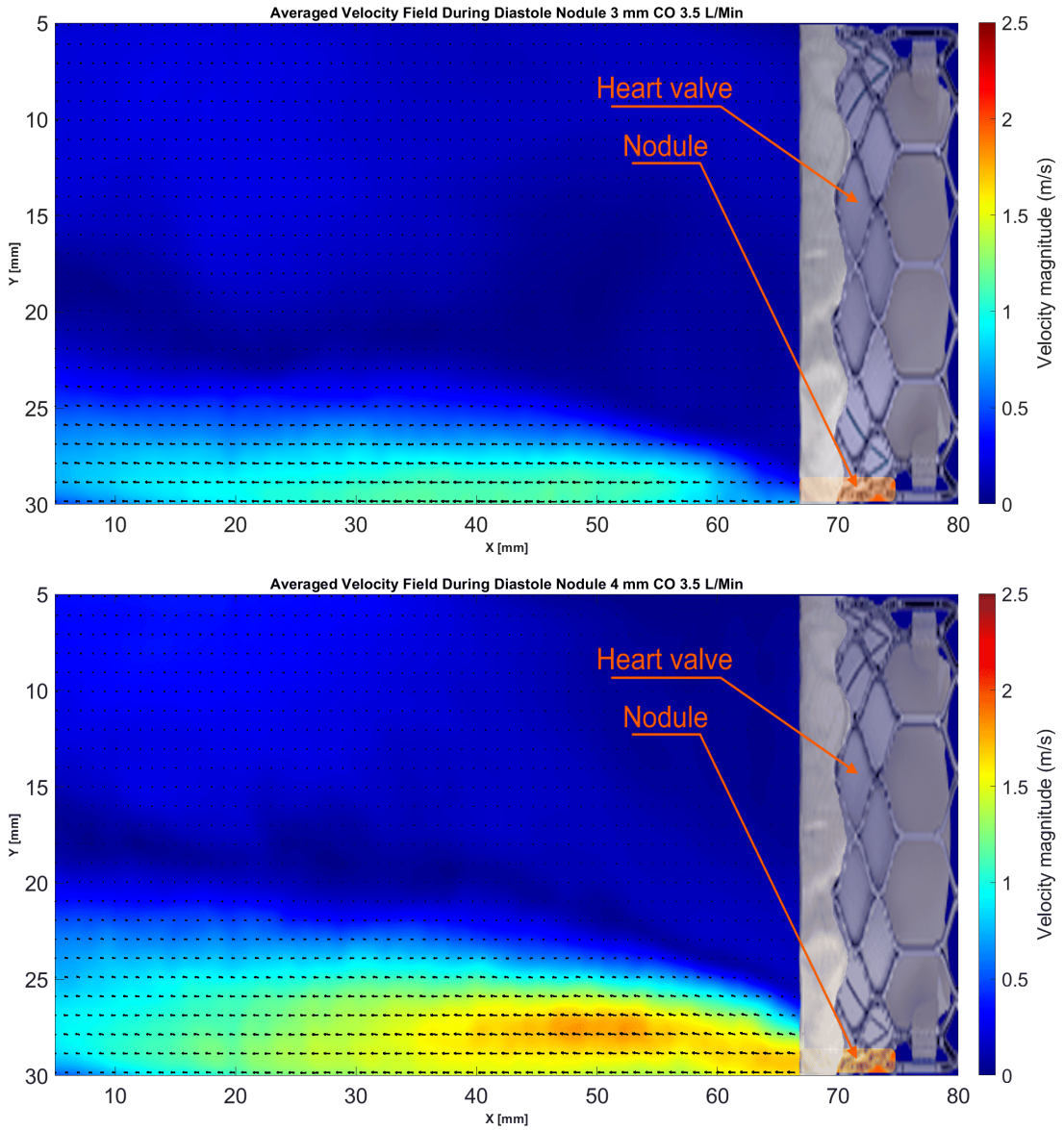

Figure B.4: Avareged velocity field during diastole Cardiac Output 3.5 L/Min

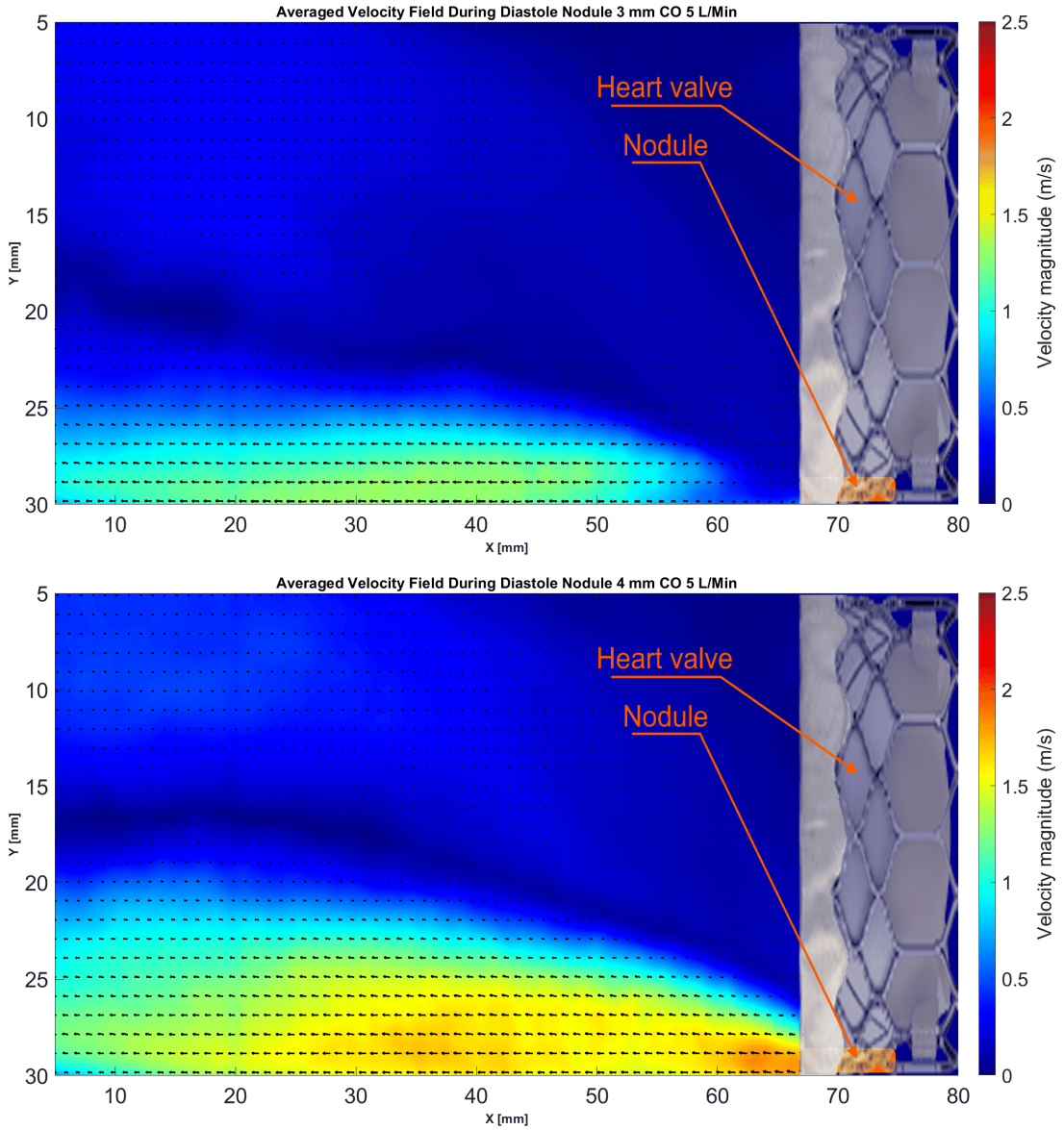

Figure B.5: Avareged velocity field during diastole Cardiac Output 5 L/Min

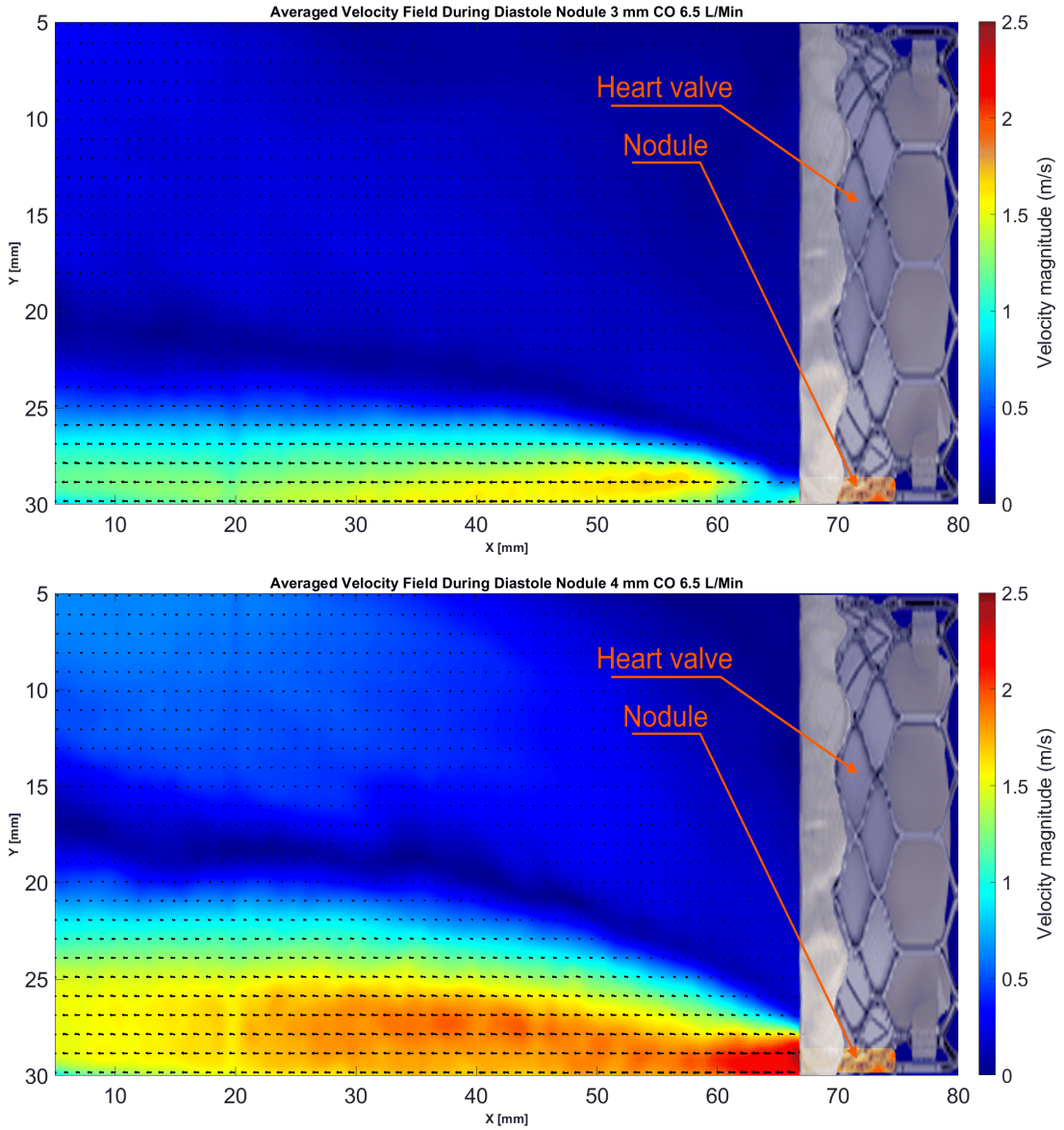

Figure B.6: Avareged velocity field during diastole Cardiac Output 6.5 L/Min

B.3 Kinetic Turbolent Energy

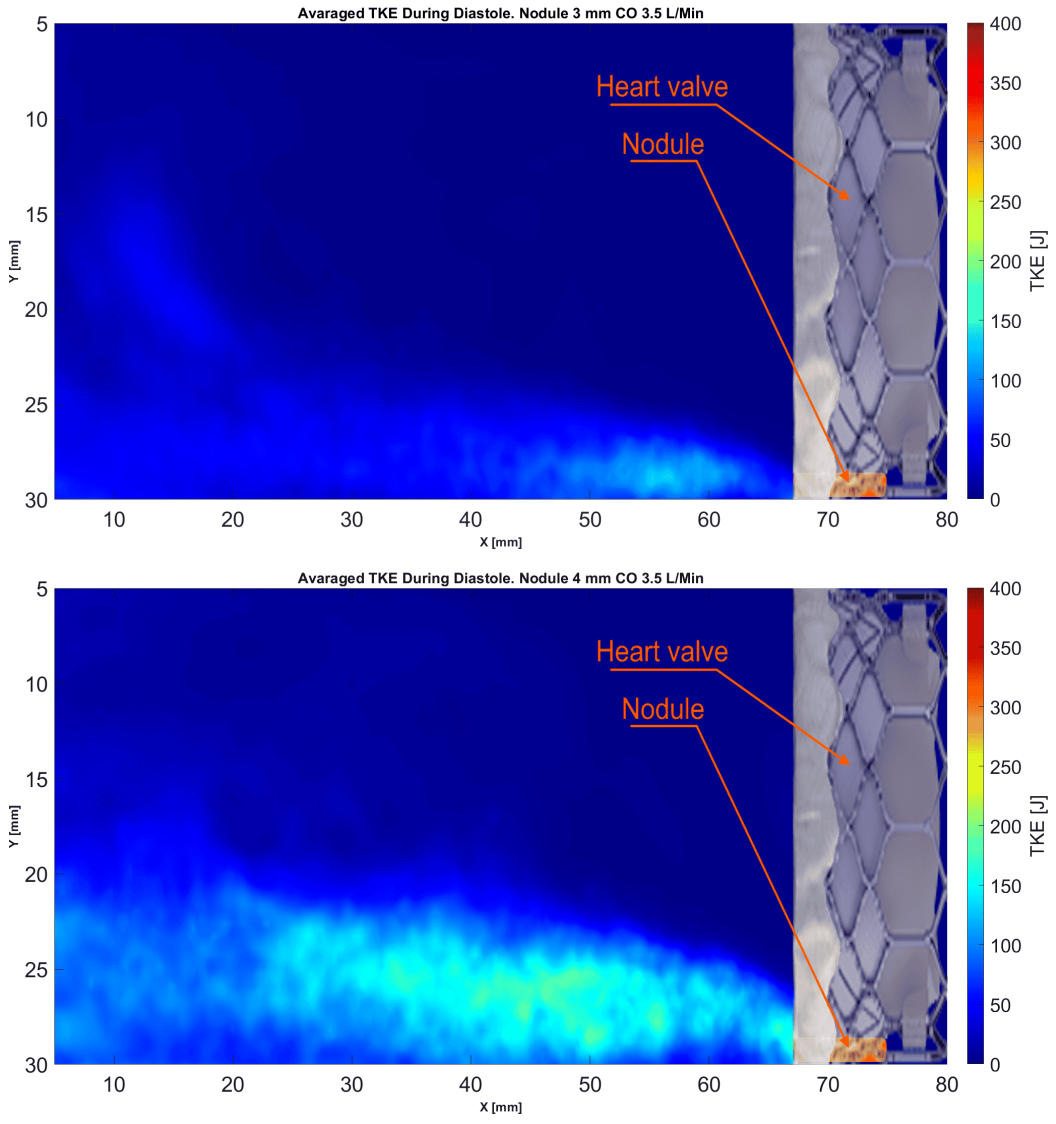

Figure B.7: Averaged KTE during diastole Cardiac Output 3.5 L/min

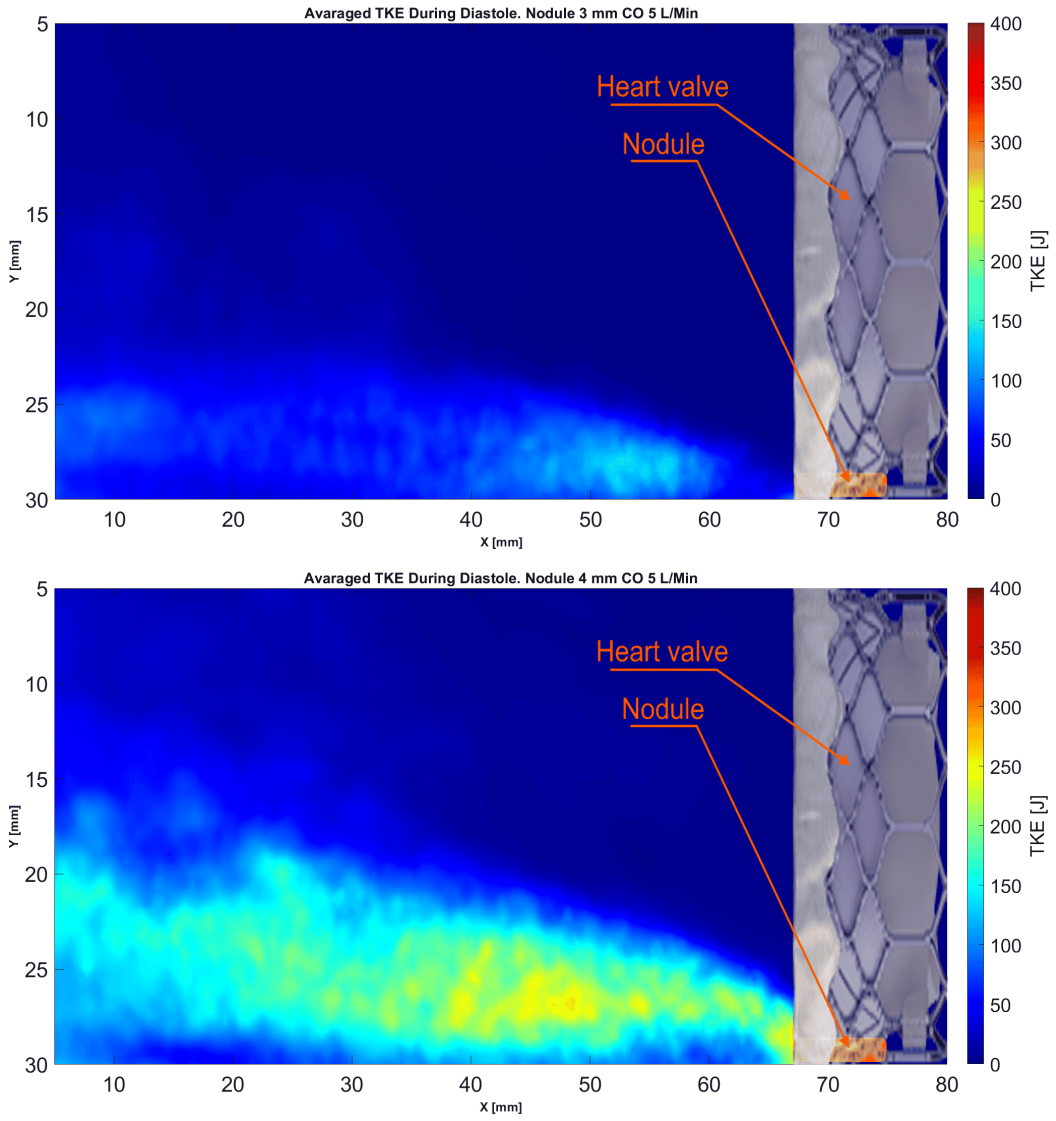

Figure B.8: Averaged KTE during diastole Cardiac Output 5 L/min

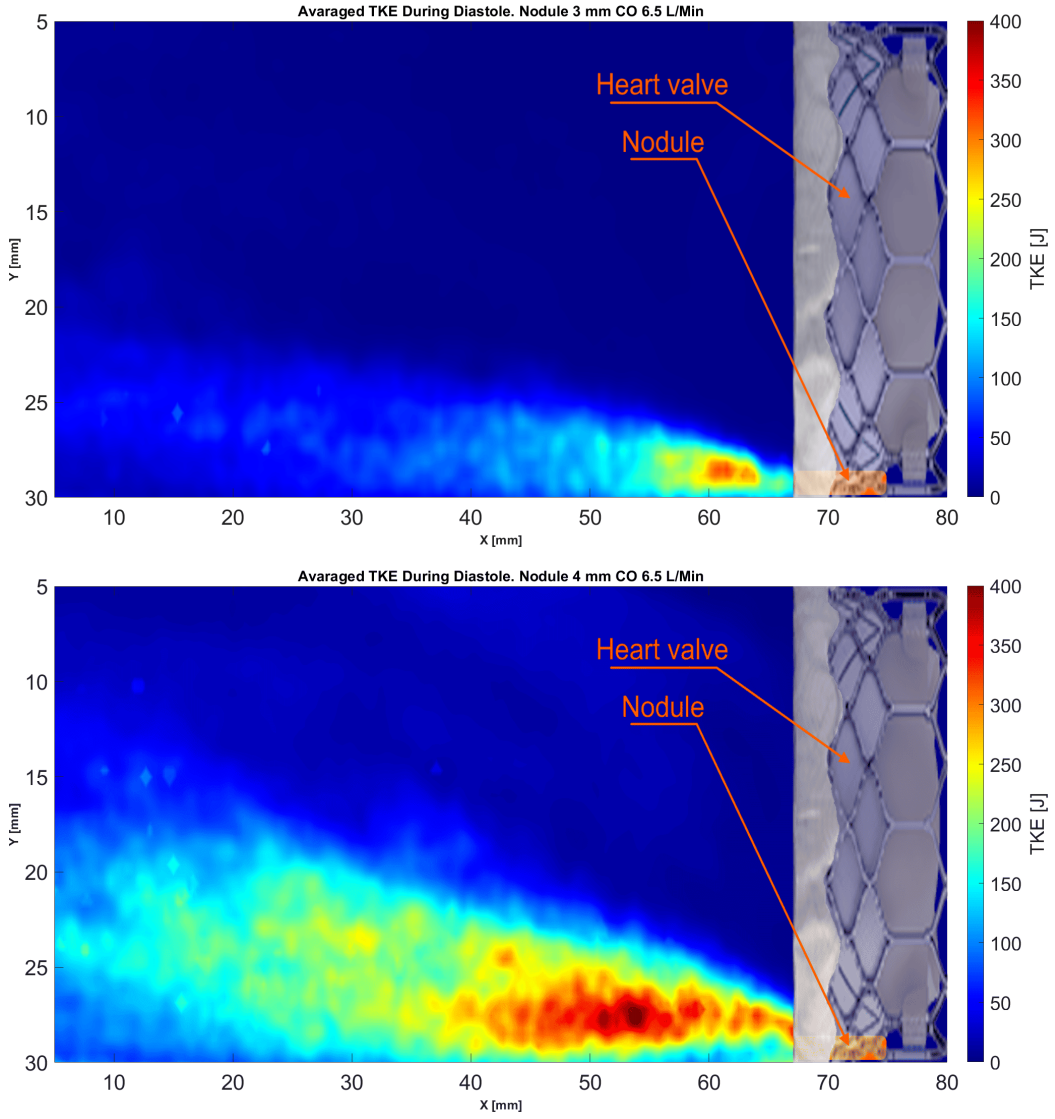

Figure B.9: Averaged KTE during diastole Cardiac Output 6.5 L/min

B.4 Shear Stress

B.4.1 Viscous Shear Stress VSS

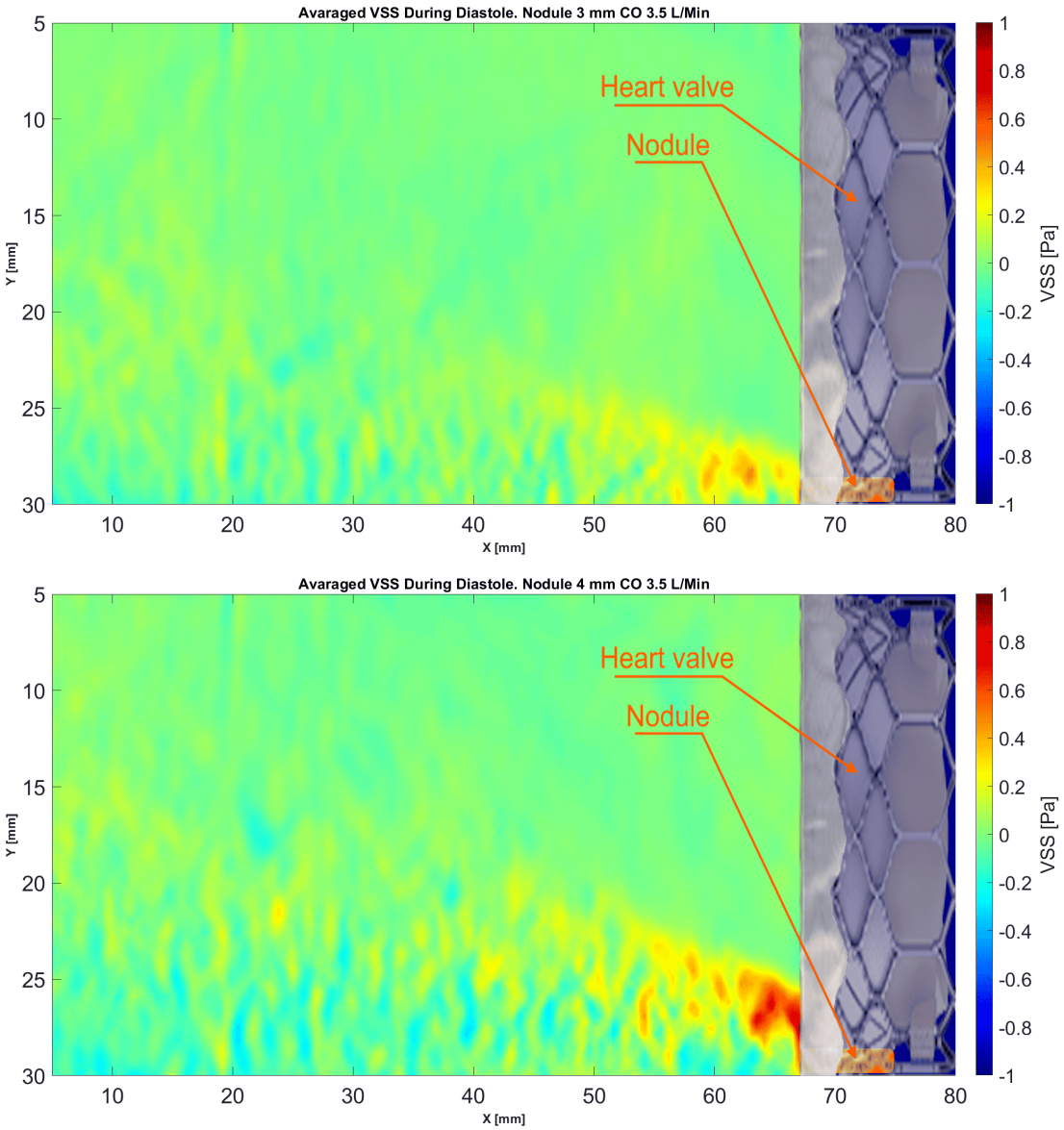

Figure B.10: Averaged VSS during diastole Cardiac Output 3.5 L/min

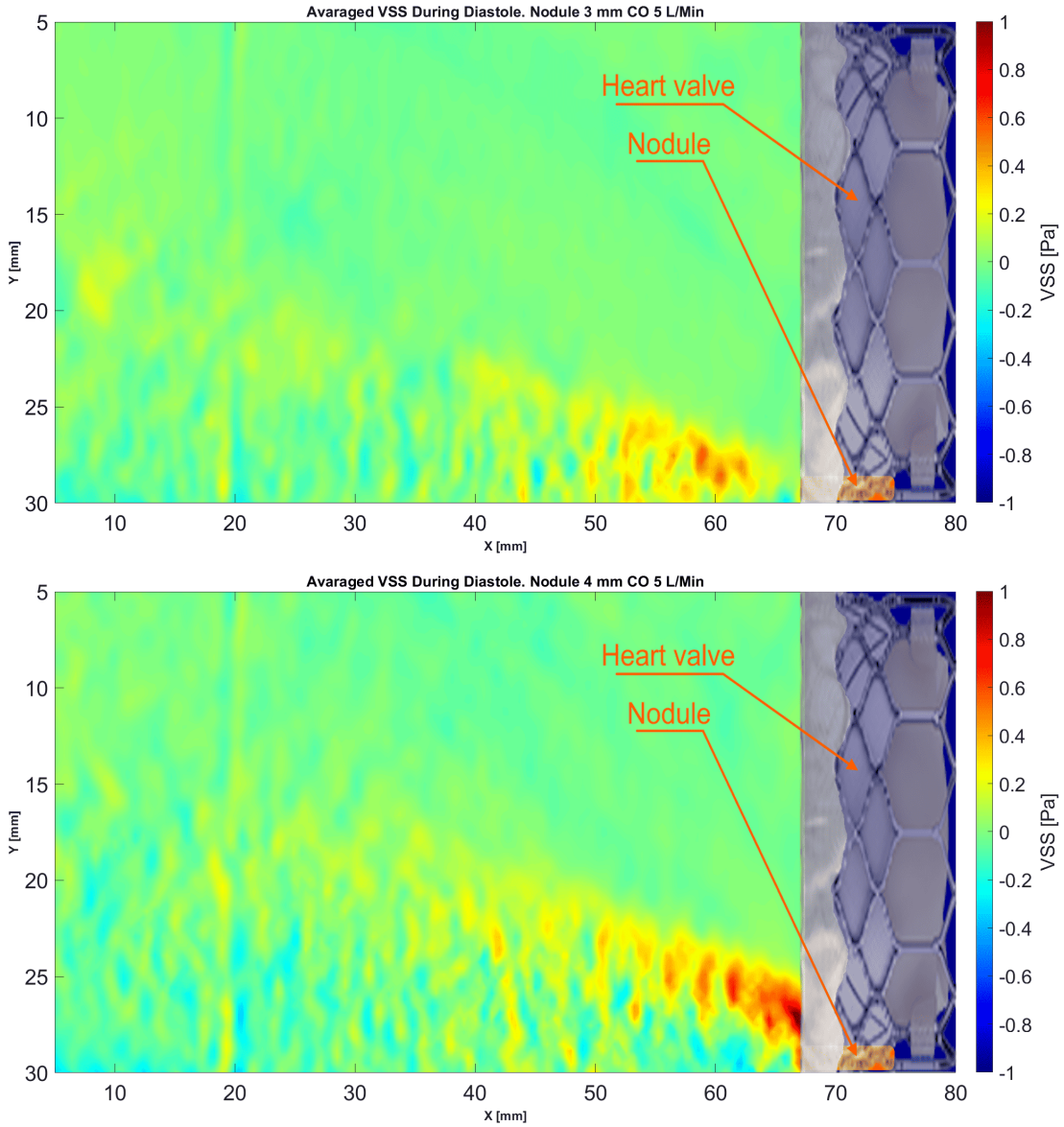

Figure B.11: Averaged VSS during diastole Cardiac Output 5 L/min

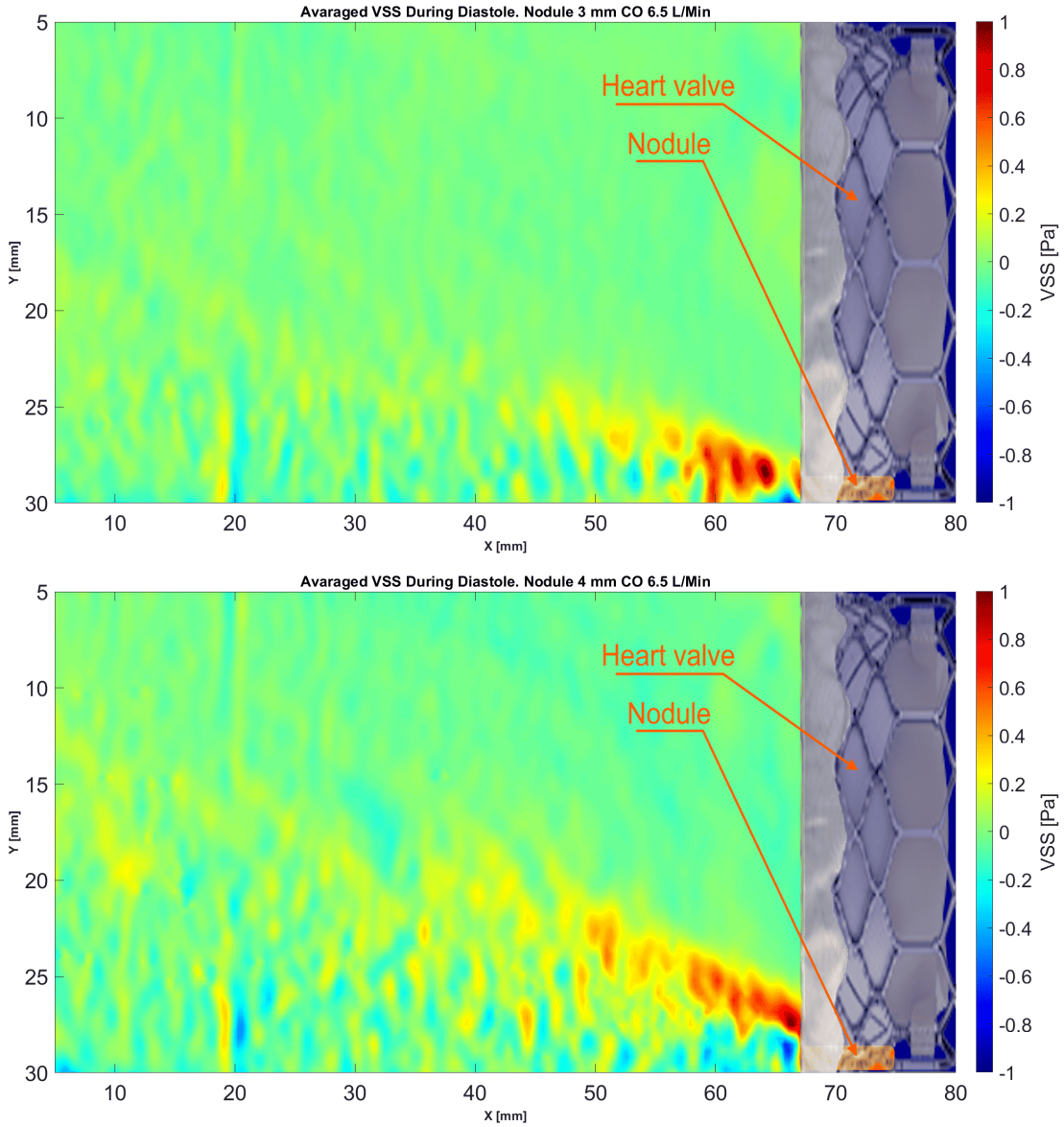

Figure B.12: Averaged VSS during diastole Cardiac Output 6.5 L/min

B.4.2 Reynolds Shear Stress RSS

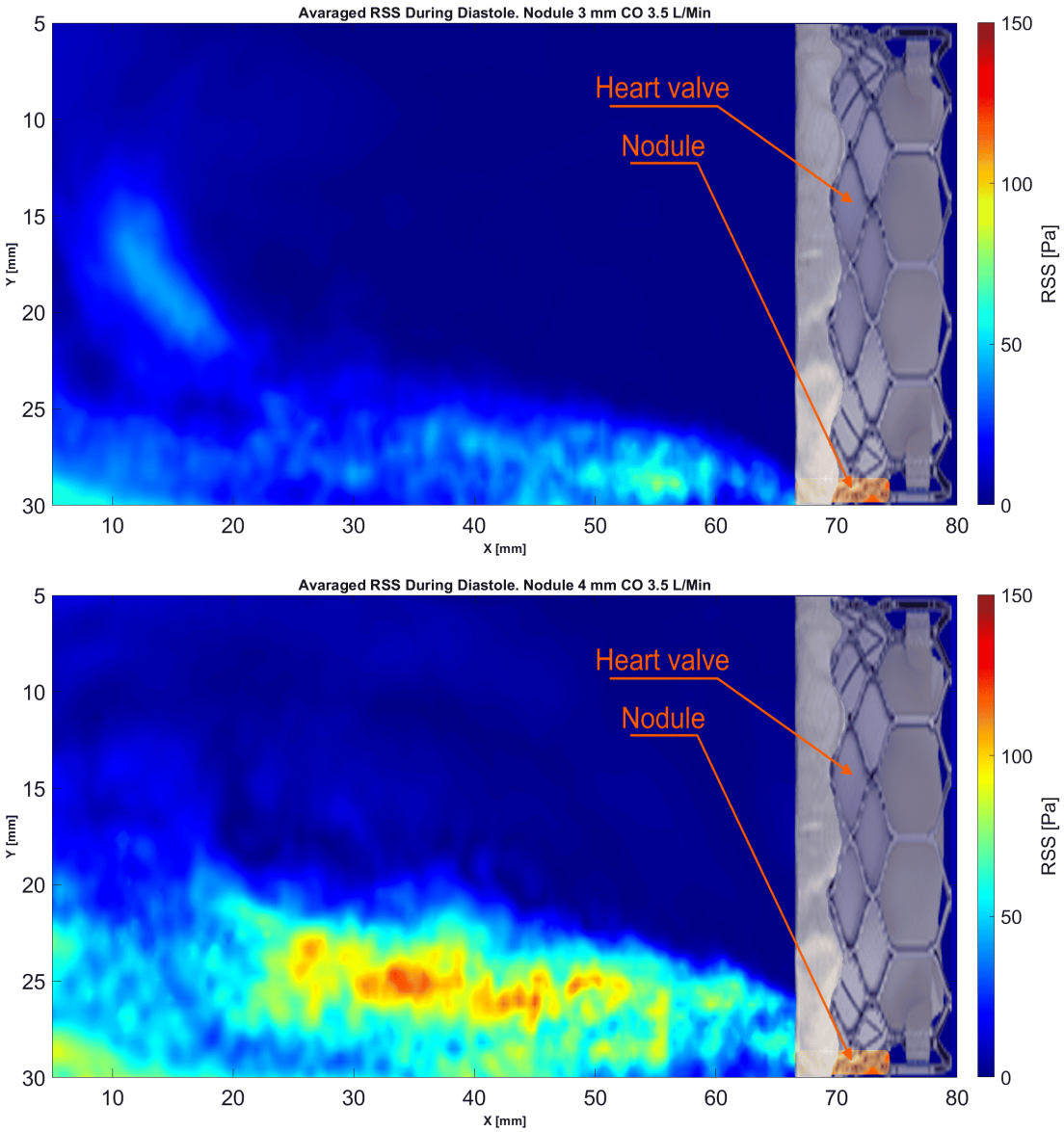

Figure B.13: Averaged RSS during diastole Cardiac Output 3.5 L/min

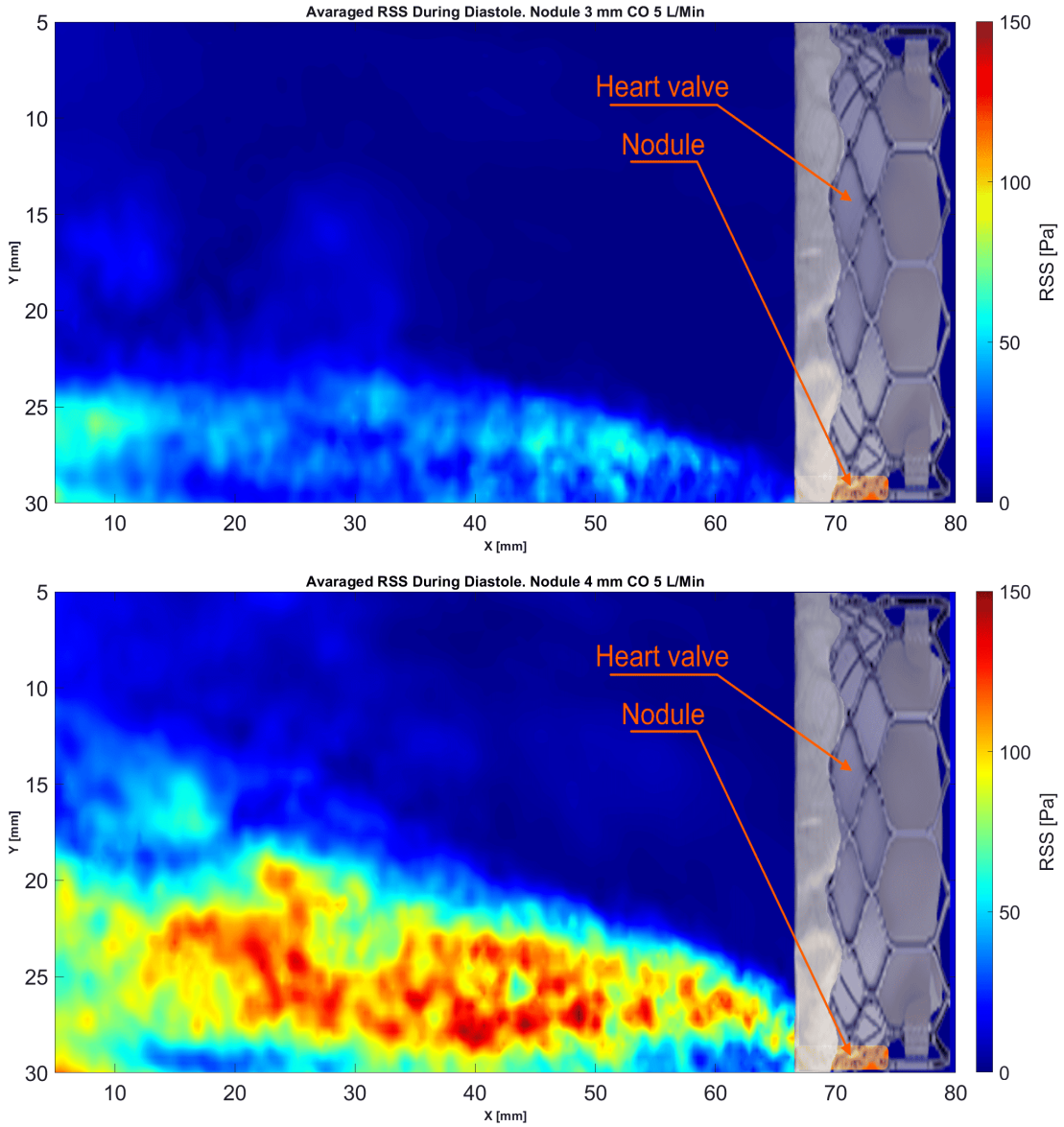

Figure B.14: Averaged RSS during diastole Cardiac Output 5 L/min

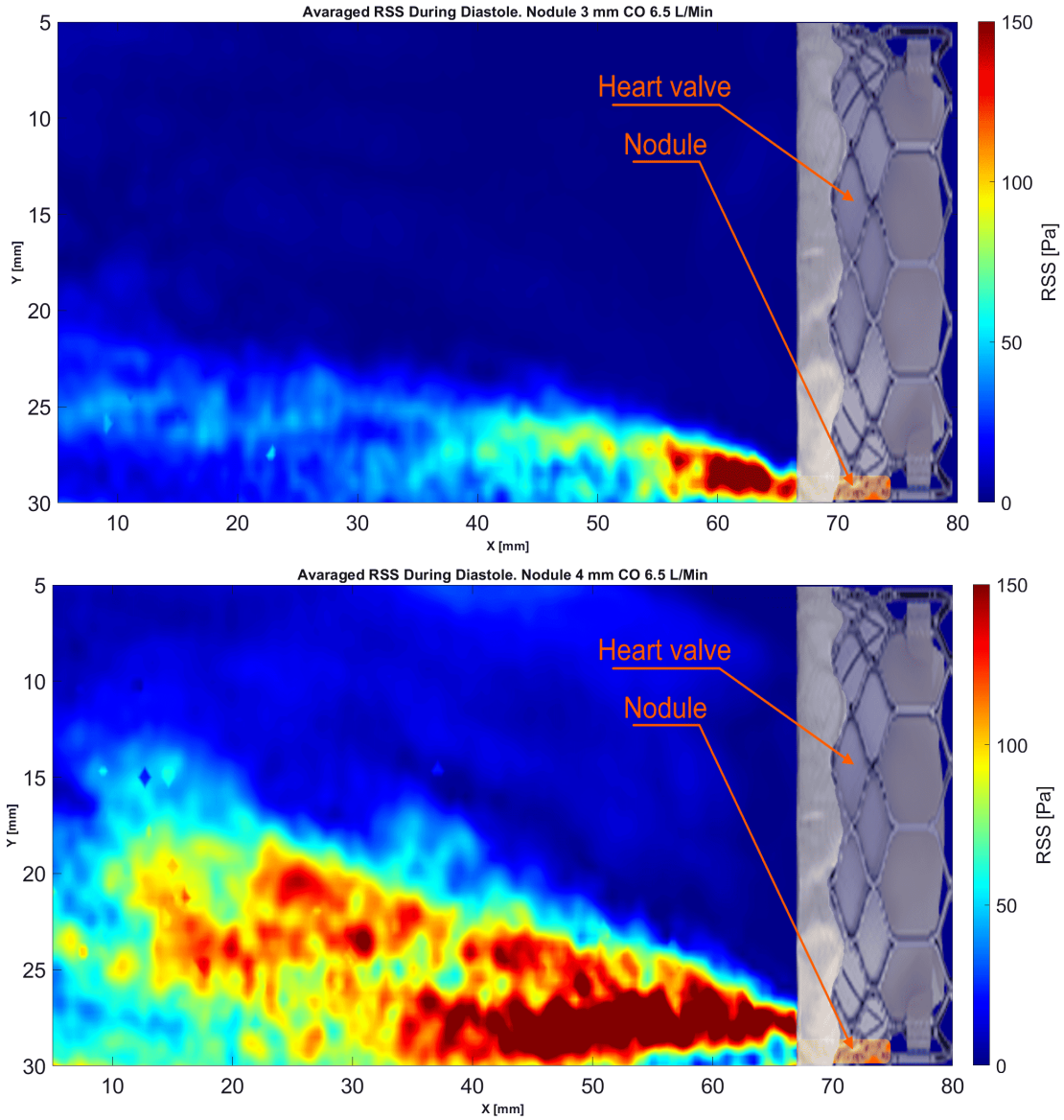

Figure B.15: Averaged RSS during diastole Cardiac Output 6.5 L/min

Bibliography

[1] *Arterial blood pressure Determinants of normal arterial blood pressure*. greek doctor (cit. on pp. 2, 4).

[2] Claudia Trejo-Soto and Aurora Hernández-Machado. «Normalization of Blood Viscosity According to the Hematocrit and the Shear Rate». In: *Journal of Microelectromechanical Systems* (2022). DOI: https://doi.org/10.3390/mi13030357 (cit. on p. 4).

[3] *Valvole cardiache su misura in silicone stampate 3D: via ai primi test*. https://biomedicalcue.it/valvole-cardiache-silicone-stampate-3d/14969/ (cit. on p. 5).

[4] *Introduction to PV loops: Understanding points on the PV loop and measures of cardiac function*. https://www.adinstruments.com/blog/introduction-pv-loops-understanding-points-pv-loop-and-measures-cardiac-function (cit. on p. 6).

[5] *ISO DOCUMENT*. DOI: https://www.iso.org/obp/ui/en/#iso:std:iso:5840:-1:ed-2:v1:en (cit. on p. 7).

[6] *On the quantification of arterial wall mechanical properties using invasive and non-invasive experimental investigations and analytical techniques*. researchgate publication 354923660 (cit. on p. 8).

[7] National Center for Chronic Disease Prevention and Health Promotion (NCCDPHP). *Heart Disease Facts*. Tech. rep. 2023. DOI: https://www.cdc.gov/heartdisease/facts.htm (cit. on p. 8).

[8] Zaid I. Almarzooq Connie W. Tsao Aaron W. Aday. «Heart Disease and Stroke Statistics—2023 Update: A Report From the American Heart Association». In: *American Heart Association* (2023). DOI: https://doi.org/10.1161/CIR.0000000000001123 (cit. on p. 8).

[9] Patrick Mathieu Brian R. Lindman Marie-Annick Clavel. «Calcific aortic stenosis». In: *Nature Reviews Disease Primers* (2016). DOI: https://doi.org/10.1038/nrdp.2016.6 (cit. on p. 9).

[10] *STENOSI AORTICA SEVERA: ARMI MODERNE PER UN MALE ANTICO*. https://salentomedico.com/stenosi-aortica-severa-armi-moderne-per-un-male-antico/ (cit. on p. 9).

[11] Sreekanth Vemulapalli MD John D. Carroll MD Michael J. Mack MD. «STS-ACC TVT Registry of Transcatheter Aortic Valve Replacement». In: *The Annals of Thoracic Surgery* (2021). DOI: https://doi.org/10.1016/j.athoracsur.2020.09.002 (cit. on p. 11).

[12] *TAVR*. https://drmssmukharjee.com/services/tavi-tavr-pavr/ (cit. on p. 11).

[13] G. Michael Deeb Jeffrey J. Popma M.D. «Transcatheter Aortic-Valve Replacement with a Self-Expanding Valve in Low-Risk Patients». In: *The new england journal of medicine* (2019). DOI: https://:10.1056/NEJMoa1816885 (cit. on p. 12).

[14] *Lifetime Management After TAVR: Younger, Low Risk Patients: Later ViV*. https://cvinterventions.com/wp-content/uploads/Pinto-Lifetime-management-after-TAVR.pdf (cit. on pp. 12, 13).

[15] Steven J. Yakubov Jeffrey J. Popma G. Michael Dee. «Transcatheter Aortic-Valve Replacement with a Self-Expanding Valve in Low-Risk Patients». In: *Th e new england journal of medicine* (2022). DOI: 10.1056/NEJMoa1816885 (cit. on p. 13).

[16] Finja Borowski Michelle Spanjaards. «A fast in silico model for preoperative risk assessment of paravalvular leakage». In: *Biomechanics and Modeling in Mechanobiology* (2024). DOI: 10.1007/s10237-024-01816-8 (cit. on p. 14).

[17] Oren M. Rotman Brandon J. Kovarovic. «Mild Paravalvular Leak May Pose an Increased Thrombogenic Risk in Transcatheter Aortic Valve Replacement (TAVR) Patients-Insights from Patient Specific In Vitro and In Silico Studies». In: *Bioengineering* (2023). DOI: https://doi.org/10.3390/bioengineering10020188 (cit. on p. 15).

[18] Shigeru Saito Yutaka Tanaka. «Quantitative assessment of paravalvular leakage after transcatheter aortic valve replacement using a patient-specific pulsatile flow mode». In: *International Journal of Cardiology* (2017). DOI: https://doi.org/10.1016/j.ijcard.2017.11.106 (cit. on p. 15).

[19] Shotaro Hirota Shunsuke Saito Toshimi Sairenchi. «Prosthetic Valve Function after Aortic Valve Replacement for Severe Aortic Stenosis by Transcatheter Procedure versus Surgery». In: *Journal of Cardiovascular Development and Disease* (2022). DOI: 10.3390/jcdd9100355 (cit. on p. 16).

[20] Timothy Fahringer Brian S. Thurow. «Comparison of Plenoptic PIV and Stereo PIV Measurements in a Wing Tip Vortex». In: *17th International Symposium on Applications of Laser Techniques to Fluid Mechanics* (2014). DOI: doi:10.1088/0957-0233/26/11/11520 (cit. on p. 23).

[21] Kyle P Lynch Timothy W Fahringer and Brian S Thurow. «Volumetric particle image velocimetry with a single plenoptic camera». In: *Measurement Science and Technology* (2015). DOI: doi:10.1088/0957-0233/26/11/11520 (cit. on p. 24).

[22] Elise Munz Hall Timothy W Fahringer and Brian S Thurow. «Volumetric calibration of a plenoptic camera». In: *Applied optics* (2018). DOI: doi.org/10.1364/AO.57.000914 (cit. on p. 31).

[23] Michael J. Simmonds Jarod T. Horobin Surendran Sabapathy. «Red blood cell tolerance to shear stress above and below the subhemolytic threshold». In: *Biomechanics and Modeling in Mechanobiology* (2019). DOI: doi.org/10.1007/s10237-019-01252-z (cit. on p. 67).

[24] Bartley P. Griffith Dong Han Jiafeng Zhang. «Models of Shear-Induced Platelet Activation and Numerical Implementation With Computational Fluid Dynamics Approaches». In: *journal of biomechanical engineering* (2022). DOI: DOI:10.1115/1.4052460 (cit. on p. 68).